STRUCTURAL PERFORMANCE OF GFRP REINFORCED BALCONY SLAB WITH THERMAL BREAK

By

Arezo Rasouli

A Thesis submitted to the Faculty of Graduate Studies of
the University of Manitoba
in partial fulfillment of the requirements for the degree of

Master of Science

Department of Civil Engineering
University of Manitoba
Winnipeg, MB, Canada

Abstract

Thermal bridging in building envelopes can lead to heat exchange with the outside. Significant thermal bridging occurs through cantilevered balconies, because they pierce through the building envelope. A potential solution is to add a thermal barrier and use materials with low thermal conductivity, such as GFRP, to reinforce balconies.

The central objective of this research was to compare the thermal and structural performance of three types of thermal breaks in GFRP reinforced cantilevered balcony slabs. This study is Phase II of a two-phase research project at the University of Manitoba. In Phase I the thermal and structural performance of specimens with Armatherm^{TM} 500 break reinforced with carbon steel, stainless steel and GFRP reinforcement were investigated (Boila, 2018).

For this study, nine segments of full-scale balcony slabs were constructed and tested. All specimens were reinforced with #15M GFRP rebars and included a thermal break midway along their length, creating an inside and outside slab separated by this thermal break. Specimen dimensions were 1600 mm by 500 mm by 190 mm.

The three types of thermal breaks used in the nine specimens were Armatherm^{TM} 500, DOW and UHMW, and each had a thickness of 13 mm. These breaks were chosen based on their thermal properties, strength and market availability. Six of the specimens (three pairs, each pair with the same type of thermal break) were tested in dual thermal chambers in which the cantilever end, representing the outside slab, was at about -30 °C. The floor end, representing the inside slab was kept at about +21 °C. The purpose was to measure the amount of heat exchange through the slab and its thermal break between the two thermal environments.

Thermal breaks were included in the location of maximum moment. Concrete, which carries most of the flexural and shear load, is completely replaced by the thermal break at that location. To evaluate the strength of this connection, structural tests for all nine specimens were carried out to failure by applying a monotonic load at the tip of the cantilever. Strain gauges and PI gauges were installed on rebar and on concrete to measure strain, dilation between thermal break and concrete, as well as crack widths on concrete. An LVDT device measured deflection due to load applied at the cantilevered end.

Thermal testing showed that Armatherm$^{\text{TM}}$ 500 is the most effective thermal break in decreasing thermal bridging through balcony slabs: In Armatherm$^{\text{TM}}$ 500 specimens the temperature difference across the thermal break was 27% and 72% greater than the temperature difference across the thermal breaks in DOW and UHMW specimens, respectively.

Structural tests showed that at service load the largest deflection in Armatherm$^{\text{TM}}$ 500 slabs was 27% and 42% smaller than the largest deflections in UHMW and DOW slabs, respectively. The dilation between the Armatherm$^{\text{TM}}$ 500 and concrete was the smallest among the three thermal break types as well. In slabs with Armatherm$^{\text{TM}}$ 500 the dilation was 33% and 18% smaller than that in slabs with DOW and UHMW thermal breaks, respectively.

In summary, at service load, the thermal and structural performance of slabs with Armatherm$^{\text{TM}}$ 500 thermal break was better than that of specimens with DOW and UHMW thermal breaks.

To

my parents

Acknowledgments

I am profoundly grateful to my advisors Dr. Dagmar Svecova and Dr. David Kuhn. Their kind support and guidance throughout this research work has been instrumental. They showed me the way all along, and were always there to provide direction and help. I am very thankful to them for giving me this opportunity to learn from their knowledge. This has been such a great experience for me. Without their ideas and advice this work would not have happened.

Dr. Svecova's support during this time went beyond just technical support. She is a role model for me.

I express my gratitude to my committee member Dr. John Wells. My research would not have been possible without his support. This project has been a collaboration between the University of Manitoba, Red River College, and Crosier Kilgour and Partners, each of which made important contributions. I express my gratitude to my committee member Dr. Dimos Polyzois for providing detailed comments on the final draft of this thesis, which helped clarify many details and enrich this thesis.

All specimens for this work were instrumented, cast and structurally tested at W.R. McQuade Structures Laboratory. Dr. Chad Klowak's continuous support was crucial for the success of my thesis. Samuel Abraha and Syed Mohit provided essential assistance throughout my lab work. I would like to express many thanks to all of them.

Many thanks to Red River College's Rob Spewak, Cory Carson, Brandon Campbell, Christin Burgess, and Joel Turner for their significant contribution to this work. Their support was essential for performing the thermal tests.

For this work GFRP rebars were donated by Pultrall, and thermal breaks were donated by Armadillo (Armatherm^{TM} 500), Jasper Plastics (DOW) and Johnson Plastics (UHMW).

I am indebted forever to my parents for their unconditional love, support and sacrifices for a better future for me. Last but not least, a special thanks to my beloved husband Bashir Ahmad for his continuous support during completion of my master's degree.

Table of Contents

List of Tables

List of Figures

Chapter 1 Introduction

1.1 Background

Many buildings lose large amounts of heat through their balconies (RDH, 2013). This amount of energy loss is significant on the global scale. Climate change has justifiably been a growing worldwide concern over the past few decades. In response, there has been a push in the construction industry to make buildings "greener". If buildings are better insulated, less energy will be consumed to keep them warm in winter and cool in summer. This is particularly true in countries where summers are hot and winters are very cold, like Canada. Less energy needed to keep buildings warm/cool will mean less fossil fuels will have to be burnt. That means a decrease in energy costs for owners. It also means less greenhouse gasses are released into the atmosphere, thus helping to slow global warming.

Balcony slabs in Canada are subject to large temperature gradients in winter. Their outside part is subject to extreme cold as low as -40 °C while their inside/floor part is subject to mild room temperatures of about +20 °C. The temperature gradient between the cold and warm parts can be as much as 60 °C. As a result, a balcony design that prevents heat exchange between the indoors and the outside is highly sought after. One way to better insulate balconies is to embed insulating materials, commonly called thermal breaks, in the slabs at the outside wall locations. A more fundamental approach is to use entirely new materials to reinforce concrete balconies. Previous work has shown that when both methods are combined, even further heat loss prevention is achieved (Boila, 2018).

Building codes in North America have been evolving such that the issues arising from balcony thermal bridging are being specifically addressed in them. At the same time, construction companies have also started taking balcony thermal bridging into account (Concrete Construction, 2019). For example, balcony thermal breaks were recently used at a luxury building in New York which is one of the first multi-family building to meet the Passive House energy efficiency requirements (Dacko, 2020).

Steel has been widely used to reinforce concrete for the past two centuries. While it has many excellent properties, it suffers from a few serious setbacks as well. Notably, steel suffers from corrosion so the maintenance cost of steel-reinforced buildings increases with age. Steel also conducts heat very well, which, in some cases, allows buildings to lose heat easily. Efforts have been under way to find new materials which have high strength, while at the same time are more resistant to corrosion. One such class of materials, which has attracted attention over the past couple of decades, are Fiber Reinforced Polymers (FRP). The use of FRP in concrete structures was first pioneered in 1954 by Rubinsky and Meier (Jeetendra, Suresh, & Hussain, 2015). FRP was initially used to retrofit and strengthen existing steel reinforced structures that needed repair. However, over the last three decades the possibility of replacing steel with FRP for reinforcement has been investigated, including at the University of Manitoba. FRPs may be especially fit for reinforcing structures that are subject to harsh environments and electromagnetic fields (Eugenijus, Edgaras, Gribniak, & Gintaris Kaklauskas, Aleksandr K. Arnautov, 2013). Balconies are an example of such structures, particularly in extremely cold environments such as Canada.

A sub-class of FRP materials are Glass FRPs (GFRP). Currently, most residential buildings are commonly reinforced with steel. Compared to steel, GFRP is lighter, electrically insulating, and conducts heat much less (B&B FRP Manufacturing Inc., 2018). In addition, GFRP is corrosion resistant, hence structures reinforced with it have lower maintenance cost. GFRP reinforced balcony slabs with thermal break may be ideal for significantly decreasing heat flow through balconies. In this work all specimens were reinforced with GFRP.

This study is Phase II of a research project at the University of Manitoba. Phase I was carried out by (Boila, 2018). The objective in Phase I was to experimentally and numerically investigate the thermal and structural performance of balcony thermal break systems reinforced with carbon steel, stainless steel and GFRP. Therefore, eighteen balcony slabs were thermally and structurally tested. Half the slabs of each reinforcement type included a 25 mm Armatherm^{TM} 500 thermal break. The carbon steel and stainless steel reinforced slabs which did not include a thermal break formed the control specimens for Phase I, as well as for this research.

The work in Phase I showed that the combination of Armatherm^{TM} 500 thermal break and GFRP reinforcement provided the best thermal insulation: on average, the temperature near the warm side of the thermal break was 13.7 °C higher for this combination, compared to regular carbon steel reinforcement without a thermal break (Boila, 2018). Thus, Phase I has paved the way for designing a practical thermal break balcony system.

The work in Phase II, described in this thesis, differs from Phase I in three main ways. Firstly, three types of thermal breaks were tested in this work. There are many other candidate thermal breaks on the market. The three types of thermal breaks were chosen in collaboration with a team at Red River College in Winnipeg, who specialize in thermal testing; and with advice from Crosier Kilgour.

Secondly, since the thermal beak is in the location of maximum moment, it negatively impacts the capacity of slabs. Therefore, the research team made the decision that in this Phase of the project thermal breaks with a reduced thickness of 13 mm will be used to improve their structural performance.

Thirdly, the two top #25 GFRP rebars used in Phase I specimens were replaced with five #15 GFRP rebars in Phase II specimens. This provides the same reinforcement area, and it was done to reduce crack width and dilation at the thermal break concrete interface.

This work was funded by NSERC CUI2I program which provides funding to university teams that work on industrially funded projects, Crosier Kilgour and Partners and SIMTReC (Structural Innovation and Monitoring Technologies Resource Centre). For all specimens in this work, GFRP rebars were donated by Pultrall, and thermal breaks were donated for this work by the following companies: Armadillo (Armatherm^{TM} 500), Jasper Plastics (DOW) and Johnson Plastics (UHMW).

1.2 Research Objectives

The main objective of this research was to compare the thermal and structural performance of three types of thermal breaks in GFRP reinforced cantilevered balcony slabs.

1.3 Scope of Work

The following three types of thermal breaks were used:

- 0.5″Armatherm^{TM} 500
- 0.5″ DOW
- 0.5″ UHMW

Nine specimens were built for the study. Three types of thermal breaks were used in these nine specimens, and thermal break thickness was 13 mm. All specimens were structurally tested to failure by applying a static monotonic load at the tip of the cantilever.

Of the nine specimens, three specimens had 13 mm Armatherm^{TM} 500, three others had 13 mm DOW, and the last three had 13 mm UHMW as their thermal breaks. Two specimens per thermal break group were selected for thermal testing prior to structural testing. Thus, thermal tests were carried out on a total of six specimens. Thermistors were installed on specimens, and thermal tests were carried out in a thermal chamber at Red River College in Winnipeg. Typical Canadian winter conditions were simulated in thermal tests, with the cold and warm sides of specimens at about -30 °C and +21 °C respectively.

1.4 Thesis Structure

This thesis includes seven chapters. Chapter one provides a broad introduction to this research by discussing the background and context of the project, main research objectives, and the scope of the work.

Chapter two is a detailed literature review of the related work. It reviews FRPs, thermal bridging in balconies, the most common thermal break solutions that have been put in practice in Canada and elsewhere, and finally previous work at the University of Manitoba on which this research is based.

Chapter three is a detailed explanation of the structural testing program for the nine main specimens of this study. It includes study design, materials, specimen preparation, and details of instrumentation i.e., the layout and installation for thermistors, strain gauges, PI gauges, and LVDT.

Chapter four discusses the structural test data and their analysis. Structural test results, data plots, comparative analysis, failure modes, and comparison with previous work is offered.

Chapter five details the thermal experimental program. It includes study design, materials, specimen preparation, instrumentation, a description of thermal chambers, and external insulation of specimens in thermal chambers.

Chapter six discusses the thermal tests and their analysis. It includes thermal test results and data plots. The thesis ends with chapter seven which summarizes the structural and thermal conclusions, and provides recommendations for future work in this area.

The next chapter provides a literature review on FRP and thermal breaks and their use in concrete structures. It also includes a discussion of the background to this research, as well as previous relevant research.

Chapter 2 Literature Review

The main focus of this chapter is on literature review regarding the recent use of thermal breaks in concrete balcony slabs. Thermal bridging in balconies and ways of dealing with it are discussed. Newly proposed energy efficient materials such as FRP, and in particular GFRP rebars, are reviewed. The use of thermal break materials in concrete balcony slabs and the latest manufactured thermal breaks are summarised. Finally, a brief summary including results and recommendations of the recent relevant work which was done by Boila, 2018 at the University of Manitoba is given. The work outlined in this thesis is in continuation of that work.

2.1 Thermal Bridges

Thermal bridges are interruptions of the insulation layer in parts of the building envelope. Such interruptions allow for greater exchange of heat between the inside and outside of a building. In colder months, this leads to reduced internal surface temperature and a higher risk of condensation and mold growth, which negatively affect the building. Thermal bridges mean higher energy consumption and reduced indoor comfort because heat is lost in winter, and in summer heat can enter buildings. Thermal bridges generally take place in zones with lower thermal resistance. Bridging can happen through elements such as plates or studs, frames, cladding supports, columns, shear walls, exposed floor slabs and balconies (RDH, 2013).

Dealing with thermal bridges is considered very important for energy efficiency. European energy policies consider them in their requirements for energy-efficient buildings. Examples include Switzerland’s energy policy, and also MINERGIE and Passive House which are two of the most common European energy standards (Goulouti, 2016). However, the significance of thermal bridges is not fully addressed in the Canadian building code. In this code major envelope piercings, such as balconies, whose cross section area is under 2% of the pierced wall’s area do not have to be considered when calculating the effective thermal conductivity of the wall in question (Ge, Ruth McClung, & Zhang, 2013).

2.1.1 Balcony Thermal Bridges

Balconies are responsible for up to 30% of most buildings’ heat losses in cold weather (Goulouti, Castro, & Keller, 2015). These slabs pierce through the building envelope in order to create an external cantilevered balcony. Steel and concrete have high thermal conductivity values and their use in balconies can lead to thermal bridging in building envelopes. Balconies are considered one of the biggest sources of thermal bridging, after windows and doors. Regardless of how well insulated a building is, if balconies allow for thermal bridging, the building will not meet energy code requirements and the intended comfort level. The R-values required by the energy code are in the range R-10 to R-20 and for the so-called green buildings they are even higher. Currently most buildings have walls in the R-2 to R-5 range. Balconies have effective R-values of about R-1 (RDH, 2013). Therefore, efforts have been underway to find efficient and low-cost thermal breaks for balconies.

Thermal break is a material with very low thermal conductivity. Usually, a thermal break element is placed between the floor slab and the balcony to decrease heat exchange with the outside. There exist a number of other solutions to limit the effect of balcony thermal bridging, such as external insulation of edges of the slab, concentrating rebar attachment of balconies, and wrapping rigid insulating foam around balconies. Each solution differs in its performance, cost and practicality (RDH, 2013).

A more fundamental approach is to look for new materials which can replace steel as reinforcement. One such promising candidate is FRP. In contrast to steel, FRPs are resistant to corrosion, and do not conduct heat and electricity. An ideal solution would be to reinforce balconies with FRP and include thermal breaks in them. In fact, this approach has been pursued at the University of Manitoba over the past several years, and is at the core of this thesis as well.

2.2 Fiber Reinforced Polymers

FRPs are composite materials generally made up of two main components: fibres and matrix. The role of fibre is to carry load. Fibres are elastic and have high strength, while matrices connect the fibres together. FRP are manufactured in many different forms, such as bars, grids and fabric. For structural applications, the fibre to matrix volume ratio should be greater than 55% in FRP bars (ISIS Canada, 2007). FRPs have low thermal conductivity and high R-values. Their thermal conductivity is up to 170 times lower than that of stainless steel (Goulouti, Castro, & Keller, 2016).

There are several kinds of fibres and matrices which can be used for manufacturing FRP. The three more common types of FRP are the following (Goulouti, 2016):

- Glass FRP: thermal conductivity of GFRP is much lower than stainless steel and efforts have been underway, including in the research outlined in this thesis, to replace stainless steel bars by GFRP bars. GFRP does not have high stiffness. Also, some GFRP shows sensitivity to the alkaline concrete environment.
- Aramid FRP: AFRP has much lower thermal conductivity and is stiffer than GFRP. However, AFRP has low compressive strength, so it cannot be widely used for components which are under high levels of compressive stress.
- Carbon FRP: CFRP is much lighter and stronger than GFRP, yet it is much more expensive. The literature search on their use in balconies does not turn up many results, probably because their cost hinders their use in balconies. Table 1 shows the thermal properties of FRP composites as well as a few non-FRP materials. It must be noted that thermal conductivity of FRP materials varies depending on how they have been manufactured.

Table 1 Comparison of thermal conductivities (Goulouti et al., 2015)

Material	Thermal Conductivity [W/mK]
Stainless steel bars	15.0
Reinforced concrete	2.5
Glass fibers	1.0
Aramid laminate	0.10

The mechanical and physical properties of different fibres vary widely. Moreover, every type of fibres has its own sub-types with somewhat different properties. Properties of the most common fibres are summarized in Table 2.

Table 2 Fibre properties (Günaslan, Karaşin, & Öncü, 2014)

Material	Tensile Strength [MPa]	Modulus of Elasticity [GPa]
Glass fibre	2410	70
Carbon fibre	3100	220
Aramid fibre	3600	124

FRPs do not show yielding, and their stress-strain relationship in tension is linear elastic until failure. The FRP used in this work was GFRP, which includes glass fiber. How does glass fiber compare with the other common fibers? According to literature, in terms of compressive strength glass fibres are slightly less strong and stiff in compression than in tension (Nanni, Luca, & Zadeh, 2014). They are similar to carbon fibres in this regard. Glass fibers' fatigue behaviour varies depending on the type of glass fibre. Glass fibres are usually less resistant to fatigue compared to aramid but generally more resistant to fatigue than carbon fibres. In terms of stiffness, glass fibres are brittle and their modulus of elasticity is much less than that of carbon fibres (Nanni et al., 2014).

Glass fibers are cheaper to manufacture and so they are the most commonly used fibres in FRP materials. They are mostly made up of silica sand. Glass fibres are usually produced through extrusion. First silica and other necessary minerals are melted and then extruded. Fibres are then coated with a chemical solution and bundled together. There are different types of glass fibres. The most common are E-glass and S-glass. E-glass or electrical glass has minimum vulnerability to moisture and is a very good insulator. It also has very good mechanical characteristics such as good tensile strength. S-glass or high strength glass has the highest tensile strength and modulus of elasticity. However, S-glass is more expensive to produce, thus E-glass is commonly used. Alkali-resistant glass (AR-glass) is very resistant to alkali environments such as cement-based matrices but currently sizes which are suitable with thermoset matrices are not available, therefore their use is limited.

GFRP is used in GFRP pipes, tanks, light-weight fuel efficient aircrafts and vehicles, wind turbines and other corrosion resistant equipment. Overall, the advantages of glass fibre include their good chemical resistance, great insulation characteristics, high tensile strength and low cost. Their disadvantages include comparatively low fatigue resistance and low tensile modulus (GangaRao, Taly, & Vijay, 2007). Table 3 summarizes the properties of the three most common sub-types of glass fibres in engineering.

Table 3 Properties of glass fiber (ISIS Canada, 2007)

GFRP sub-type	Tensile Strength [MPa]	Modulus of Elasticity [GPa]	Elongation [%]	Coefficient of Thermal Expansion [x 10^{-6}]	Passion's Ratio
E-Glass	3500-3600	74-75	4.8	5	0.2
S-Glass	4900	87	5.6	2.9	0.22
Alkali Resistant Glass	1800-3500	70-76	2 - 3	N/A	N/A

2.2.1 FRP in Codes

There are currently two design codes in Canada which permit the use of FRP as internal reinforcement for concrete structures. One is applicable to FRP reinforcement in building components (CSA S806, 2017). The other code is applicable to bridge structures (CSA-S6, 2019). This research refers to (CSA S806, 2017), and uses the load factors specified by the National Building Code of Canada (National Research Council Canada, 2015).

2.2.2 GFRP Rebar Properties

V-Rod GFRP rebars were used for reinforcing balcony slabs in this work. Mechanical properties of V-Rod are as shown in Table 4 (Pultrall, 2018).

Table 4 Typical mechanical properties of GFRP reinforcing bars

GFRP V-ROD	Tensile Strength [MPa]	Modulus of Elasticity [GPa]	Ultimate Tensile Strain
	710	46.4	0.015

The bond of these bars with concrete is equal to, or better than, the bond of steel bars (ISIS Canada, 2007). According to Design and Construction of Structural Concrete Reinforced with FRP Bars (ACI Committee 440, 2015), the most important advantages of using GFRP rebars in concrete structures are:

- A greater tensile strength than steel bars.
- Lighter in weight: one-fourth to one-fifth of steel bars.
- They do not experience corrosion, and have a much better service life than steel.
- They have much lower thermal conductivity than steel.
- They have much lower electrical conductivity than steel.

Thermal properties of FRPs depend on a number of factors such as the type of fibre and matrix used in the FRP, and the fiber-volume ratio (ISIS Canada, 2007). It must be noted that thermal properties of FRPs are substantially different in the longitudinal and transverse directions, as seen in Table 5. For the purposes of this work, longitudinal thermal properties of GFPR rebars matter the most, as the main focus of this research is to decrease longitudinal heat flow along balcony slabs.

Table 5 Typical coefficients of thermal expansion for GFRP rebars

Coefficient of Thermal Expansion [x 10^{-6}/°C]	
Longitudinal	6 to 10
Transverse	21 to 23

2.3 Use of Thermal Breaks in Concrete Balcony Slabs

Cantilevered balcony slabs are extensions of the floor. As mentioned earlier, this leads to thermal bridging. Thermal breaks are materials whose thermal conductivity is lower than steel and concrete. A thin layer of thermal break material may be inserted across the width of a cantilevered balcony slab to significantly decrease heat flow between outdoor and indoor environments through the balcony. The construction industry is starting to use thermal breaks in concrete balcony slabs. The primary challenge preventing the widespread use of thermal breaks, however, is their cost and that fitting a thermal break inside balcony slabs may make them structurally vulnerable. In addition to being highly insulating, a desirable thermal break material needs to have high compressive and shear strength. One challenge is that materials with low thermal conductivity usually also have low compressive strength, which makes them undesirable for load bearing thermal breaks needed in balconies (Boila, 2018). Research is ongoing to find reinforcement designs which incorporate thermal breaks, which at the same time meet the required serviceability requirements.

The use of thermal breaks in balconies was first championed in Europe. European countries and in particular Germany had an important role in producing and using of the thermal break technology (Chafik, 2015). Research and studies in Canada and the US on the use of thermal breaks in cantilevered concrete balcony slabs have built on European technology. According to (Chafik, 2015) the American Society of Heating, Refrigerating and Air-Conditioning Engineers (ASHRAE) research project was the first in North America to investigate thermal bridging and the use of thermal breaks to eliminate it, and mostly focuses on the use of thermal breaks in concrete balcony slabs. In the following six different types of thermal breaks which are currently available are described.

2.3.1 Schöck Thermal Break System

Balcony thermal breaks have been used in Canada before. One example is Schöck Isokorb® thermal breaks. These have been used in concrete balcony slabs of a 30 story high-rise residential building named Ventus at Metrogate in Scarborough, Ontario, and in a 6 story multi unit residential building named Beaver Barracks in Ottawa, Ontario (Chafik, 2015).

According to Schöck, when its thermal breaks are used in balconies and parapets of a building, they decrease a building's heat loss by as much as 14%. Schöck's thermal break is light and easy to carry and install, and its installation takes about 5 minutes per each balcony. Furthermore, inserting a thermal break during casting, as opposed to wrapping a balcony slab with insulation, decreases construction costs by up to 10% (Saunders, 2020). Figure 1 shows the use of Schöck Isokorb® thermal breaks in a concrete balcony slab in Canada. According to Schöck Isokorb® the efficiency in preventing heat loss of this thermal break is about 50% (Chafik, 2015).

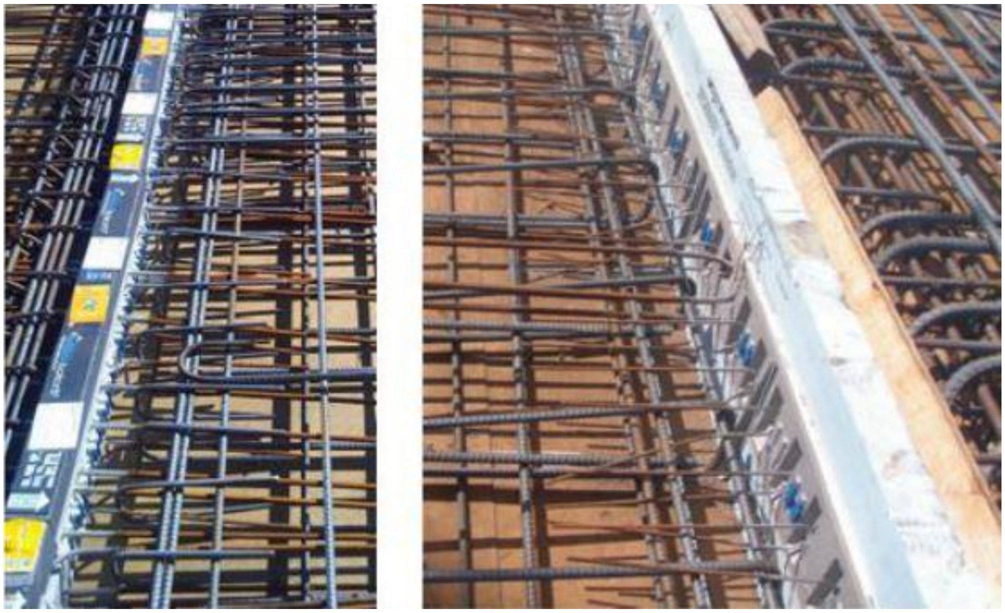

Figure 1 Schöck Isokorb® thermal break in concrete balcony (Chafik, 2015)

2.3.2 A/GFRP Thermal Break Concept

In 2014, (Goulouti et al., 2016) investigated the potential impacts of using high performance FRP thermal breaks in balcony connections. They concluded that a thermal break made up of FRP can achieve the following:

- The thermal breaks have a linear thermal transmittance <0.10 W/m^2.
- Thermal losses can be reduced by 18%.
- Heating requirements of a building with an optimum envelope can be reduced by 41%.

The thermal break proposed in (Goulouti et al., 2016) is a multifunctional component. Moment and shear forces from the balcony concrete slab are transferred through the thermal break to the inner concrete slab of the building. The proposed thermal break has a thermal conductivity which is much smaller compared to the currently used stainless steel bars in balcony connectors. Because AFRP has greater stiffness, the author proposed the use of AFRP loops to transfer the moment-tensile force of the balcony cantilever. They proposed to use a short pultruded GFRP component for bearing the compression force. A hexagonal component made of AFRP or GFRP which has a polyurethane core is attached to the pultruded GFRP component and its function is to transfer the shear force through an inclined compression diagonal. Figures 2 and 3 show the thermal break and its AFRP loop.

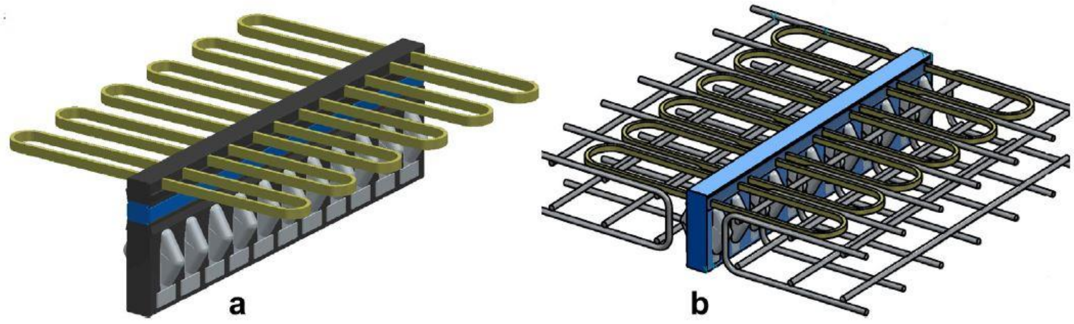

Figure 2 Thermal break: a) prefabricated A/GFRP b) the break placed from top into pre-installed concrete slab reinforcement (Goulouti et al., 2016)

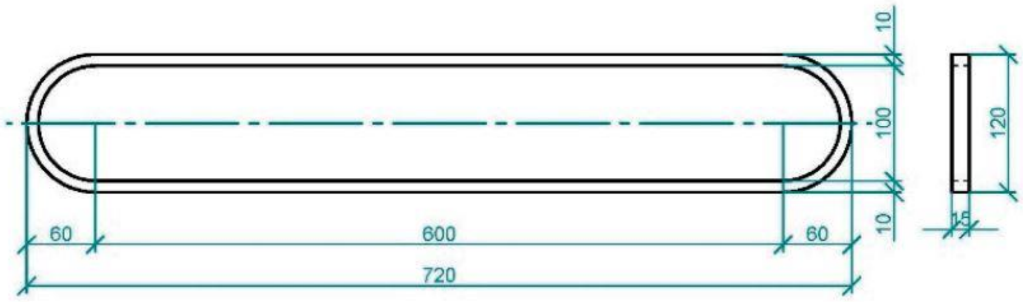

Figure 3 AFRP loop; dimensions in mm (Goulouti et al., 2016)

2.3.3 Armadillo Thermal Break

The main product offered by Armadillo is a thermal break called Armatherm^{TM} 500. It is made of polyurethane and thermoset materials which do not catch on fire or melt. This is an important specification for a structural material used in buildings. This thermal break also has high compressive strength, which is important for balconies. The load supporting capacity of the thermal break depends on its density as shown in Table 6. Armatherm™ 500 thermal breaks are made such that they do not absorb water and moisture (Armadillo, 2019).

Table 6 Specifications of Armatherm™ 500 thermal break (Armadillo, 2019)

Armatherm™ 500			
Specifications	500 – 150	500 – 200	500 – 280
Compressive stress [MPs]	3.86	7.58	14.82
Compressive modulus [MPs]	125.00	199.94	339.91
Thermal conductivity [W/mK]	0.0461	0.0562	0.0764
R Value	3.1	2.6	1.9
Operating temperature °C	-184.4/+79.4		

Armatherm™ 500 is provided at several densities and thicknesses. Currently it is available in sheets of 203.2 x 101.6 x 50.8 mm and 152.4 x 203.2 x 254 mm for the desired U-values. This thermal break has been used in a variety of structures:

- Concrete balcony slab
- Slab/Floor edge
- Parapets
- Column base
- Roof penetrations
- Roof edge
- Slab to foundation
- Foundation to wall

Armatherm™ 500 was previously used by Boila, 2018 at the University of Manitoba, and was one of the three thermal breaks used in the study outlined in this thesis.

2.3.4 Johnson Industrial Products Thermal Break

The product offered by Johnson Industrial Plastics is called Ultra High Molecular Weight (UHMW) Polyethylene. The UHMW thermal break is a semi-crystallin material which does not absorb water and is strong against chemical and mechanical damage i.e., it has good wear resistance. Moreover, its impact strength is very high and it is a good insulator. UHMW has a low coefficient of friction and so may not create sufficient bond with the concrete (Johnston Industrial Plastics, 2018).

The UHMW thermal breaks available in the market are in the form of sheets of size 1219.2 x 3048 mm which range in thickness from 25 mm to 127 mm. A UHMW sheet of 13 mm thickness was used in this study. Table 7 shows mechanical and thermal properties of the UHMW thermal break.

Table 7 UHMW material specifications (Technical Products Inc., 2018)

Specifications	UHMW
Compressive strength [MPs]	20.68
Compressive modulus [MPs]	551.58
Thermal conductivity [W/mK]	0.4093
Operating temperature °C	+82

2.3.5 Jasper Plastics Thermal Break

DOW thermal break is made of polyurethane foam which has high density and high compressive strength. They are mostly used as a thermal barrier between concrete foundation and steel columns. The material that makes DOW thermal break is non corrosive, resistant to moisture and does not rot or dissolve. The DOW thermal break used in this study is JP-1800 Psi. The advantages of JP-1800 are:

- Energy savings: it reduces heat flow.
- Strength and stability: the thermal break's high compressive strength allows higher load capacity.
- High moisture resistance: closed cell polyurethan foam doesn't absorb water.

However, DOW break is combustible and should be used away from high heat areas. Table 8 shows mechanical and thermal properties of the DOW thermal break.

Table 8 DOW material specifications (Jasper Plastics, 2020)

Specifications	DOW
Compressive strength [MPs]	12.41
Compressive modulus [MPs]	455.05
Thermal conductivity [W/mK]	0.2306

2.3.6 Fabreeka-TIM® Thermal Break

Fabreeka produces a thermal break/insulating material using a fiberglass-reinforced laminate composite. According to the company website, the thermal break is an efficient, energy-saving product which inhibits thermal bridging in structural connections. The thermal break is used between flanged steel connections and can bear loads. According to the company, their thermal break is not only resistant to conduction of heat, but also has high compressive strength: "Fabreeka International's thermal insulation material has a per-inch R-value of 0.56 and a thermal conductivity of 3.113 W/mK and is far superior to steel (R-0.003) or concrete (R-0.08), providing a structural thermal break between flanged steel framing members."(Fabreeka International Inc., 2016). Figure 4 shows the Fabreeka-TIM® thermal break.

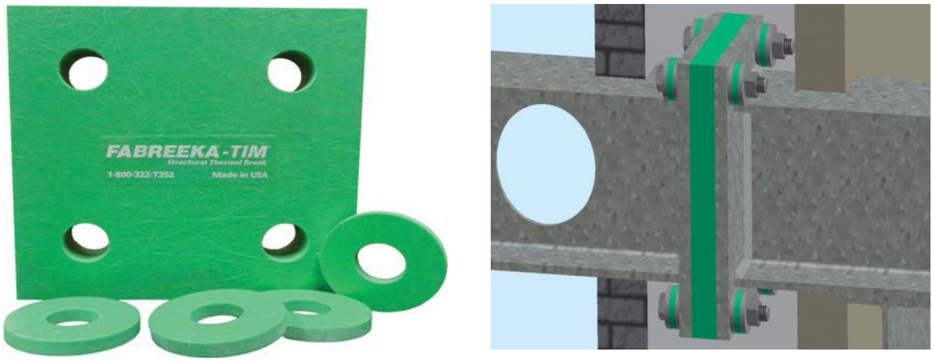

Figure 4 Fabreeka-TIM® thermal break

2.4 Previous Work at the University of Manitoba

Research has been going on at the University of Manitoba's Department of Civil Engineering on thermal breaks in concrete balcony slabs since 2015 (Boila, 2018). The end goal is an optimal reinforcement design which provides the best balance between thermal and structural performance. In earlier research balcony specimens reinforced with carbon steel, stainless steel and GFRP were tested. Six slabs were reinforced with GFRP, six with carbon steel and six with stainless steel.

Three slabs of each reinforcement type included a 25 mm thick Armatherm^{TM} 500 thermal break. Specimens with and without thermal break were tested both structurally and thermally.

In the thermal tests previously conducted at the University of Manitoba, specimens were exposed to 21°C on the warm side (i.e., indoors) and -31°C on the cold side (i.e., the outdoor cantilevered end). The same temperature range was used in the research outlined in this thesis. These values were chosen to represent typical winter conditions in many Canadian cities including the city of Winnipeg. The work conducted by Boila (2018) showed that the combination of Armatherm^{TM} 500 thermal break and GFRP reinforcement provided the best thermal insulation: on average, the temperature near the warm side of the thermal break was 13.7 °C higher for this combination, compared to the regular carbon steel reinforcement without a thermal break (Boila, 2018). As part of that work, a numerical simulation of thermal tests was carried out using Heat3. The simulations showed that Armatherm^{TM} 500 thermal breaks in conjunction with GFRP reinforcement reduced longitudinal heat flow by as much as 62.5%, while the same thermal break in conjunction with stainless steel reinforcement reduced heat flow by 50%.

The key question, however, was whether such a combination would provide the necessary structural strength needed for balconies. To find the answer, Boila (2018) tested these specimens for ultimate load capacity and serviceability. She found that GFRP reinforced slabs with thermal break did not undergo failure at the thermal break. The specimens had the same strength as that of GFRP reinforced slabs without thermal break, which meant the addition of a thermal break did not weaken the slabs. In contrast, yielding took place in the steel reinforcement at the location of the thermal break, leading to large deformations. All specimens with thermal breaks experienced dilation between concrete and the thermal break. Also, rotation at the balcony connection for specimens with a thermal break was two times as much as that experienced by specimens without a thermal break.

GFRP reinforced specimens with thermal breaks experienced less deflection compared to GFRP specimens without thermal break. Their deflection at ultimate was less than that of steel reinforced specimens, because steel yielded before failure of slabs. Moreover, dilation between thermal break and concrete was a major issue that needed to be addressed by future work.

In the work presented in this thesis specimens were tested for structural and thermal performance using an improved GFRP reinforcement design. Boila (2018) used only one type of thermal break, namely Armatherm^{TM} 500. In the current work, three different types of thermal breaks were used in specimens, and the thermal and structural performance of those specimens were experimentally evaluated.

Prior to the work on the current experimental program, two initial concrete balcony specimens were built and tested structurally for their serviceability behaviour. The only difference between these two initial specimens and those in the previous work by Boila (2018) was the size and number of the reinforcing bars. The top tension rebars were 2 #25M in previous work, with a total area of 1145 mm^2. In the two initial specimens they were replaced with 5 #15M rebars with a total area of 1165 mm^2. The main purpose was to compare dilation at the thermal break with the earlier study by Boila (2018).Since satisfactory structural results were achieved from the two initial specimens, the same reinforcement arrangement was used for the nine main specimens of this study. For extended details regarding the initial two specimens in this study, see Appendix A.

The next chapter includes the details of the structural experimental program, how specimens were made and instrumented, and what the test setup was for this work.

Chapter 3 Structural Experimental Program

Of the nine specimens in this study, six were tested thermally at Red River College, and all nine were structurally tested at the University of Manitoba.

All specimens were designed following the load requirements of the 2015 National Building Code of Canada for a typical 6 foot (1.83 meter) cantilever balcony. A typical balcony slab has a cantilever length 1830 mm, a width of 1000 mm and a depth of 190 mm. However, the capacity at Red River College to lift the specimens when placing them in the thermal chamber was limited. As a result, the length and width of all specimens had to be reduced: All specimens in this study were 1600 mm long and 500 mm wide. Specimen thickness was 190 mm which is the same as that of a typical 6 foot cantilever balcony. As such, all specimens were essentially cut-outs of typical balcony slabs with the same dimensions as those in the previous study (Boila, 2018). This chapter discusses specimen preparation.

3.1 General – Description of Specimens

Three types of thermal breaks, listed below, were used in the nine specimens of this study:

- Armatherm^{TM} 500 (Armadillo, 2019)
- DOW (Jasper Plastics, 2020)
- UHMW (Johnston Industrial Plastics, 2018)

For all nine specimens the thermal breaks were 13 mm thick, and all rebars were the same size: #15M GFRP rebars. See Table 9 for reinforcement details of the nine main specimens.

Table 9 Specimen reinforcement

Specimen Reinforcement	Thermal Break	# Specimens
Top: 5 #15M GFRP Bottom: 2 #15M GFRP Transverse: 8 #15M GFRP	13 mm Armatherm^{TM} 500	3
	13 mm DOW	3
	13 mm UHMW	3

The same naming plan for strain gauges as used in Phase I of the program was used, namely the support side is referred to as the north side, and the cantilevered side is called the south side. In all specimens these two slab portions were separated with a thermal break. Moreover, west and east were used to denote the two sides of the slab on which PI gauges were installed.

As seen in Table 10 below, the specimens were divided into three groups of three. From each group, two specimens were tested thermally and structurally, while one specimen from each group was only tested structurally.

Table 10 Naming of specimens

Specimen Name	Type of Thermal Break [13 mm thick]	# of Slabs
AR1, AR2, AR3	Armatherm^{TM} 500	3
UHMW1, UHMW2, UHMW3	Ultra High Molecular Weight Polyethylene	3
DOW1, DOW2, DOW3	DOW	3

3.2 Materials

3.2.1 Concrete

A ready mix normal strength concrete with a compressive strength of 40 MPa was used for casting the slabs. In addition to the slabs, compression [102 mm x 203 mm] cylinders were tested. Compression tests of cylinders were done according to ASTM C39 - 18 Standard Test Method for Compressive Strength of Cylindrical Concrete Specimens (ASTM International, 2019). Compression cylinders were prepared prior to casting the slabs. Based on ASTM International (2019), a total of 24 compression cylinders were cast on the day of casting of the slabs: Groups of three cylinders were tested 7, 14, and 28 days after casting . Moreover, groups of three cylinders were to be tested on each of the four days of testing of the slabs. The aim was to check concrete strength on those days. Tables 11 and 12 outline the results.

The first three specimens AR3, DOW3, and UHMW3 were tested on the 28th day of casting of concrete. The test results of compressive cylinders on the 28th day was used as concrete compressive strength. The concrete compressive strength of the remaining six slabs is included in Table 12.

Table 11 Results for compression cylinders

Cylinder No.	Test Age [day]	Measured Dimensions		Max Load [lb]	Max Load [kN]	Compressive Strength [MPa]	Average Compressive Strength [MPa]
		Diameter [mm]	Area [mm^2]				
1	7	102	8219	68904	307	37	37
2	7	101	8064	64295	286	35	
3	7	102	8220	69758	310	38	
4	14	101	8012	82620	368	46	48
5	14	101	8036	86507	385	48	
6	14	101	8059	90360	402	50	
7	28	101	8059	81111	361	45	50
8	28	102	8110	94442	420	52	
9	28	101	8010	93161	414	52	

Table 12 Results for compression cylinders on the day of testing

Specimens	Cylinder No.	Measured Dimensions		Max Load [lb]	Max Load [kN]	Compressive Strength [MPa]	Average Compressive Strength [MPa]
		Diameter [mm]	Area [mm^2]				
AR$_2$	1	103	8332	68450	304	36	40
	2	103	8332	81840	364	44	
	3	102	8171	74630	332	41	
AR$_1$, DOW$_1$, DOW$_2$ & UHMW$_2$	1	102	8171	88040	392	48	48
	2	101	8012	79280	353	44	
	3	101	8012	92860	413	52	
UHMW$_1$	1	101	8012	92430	411	51	43
	2	101	8012	58070	258	32	
	3	102	8171	85610	381	47	

3.2.2 Thermal Break

Three different types of thermal breaks with thickness of 13 mm were used in the slabs: Armatherm^{TM} 500, DOW and UHMW. The key difference between these thermal breaks is their thermal conductivity, which is 0.0562 W/mK for Armatherm^{TM} 500 (Armadillo, 2019), 0.2306 W/mK for DOW (Jasper Plastics, 2020), and 0.4093 W/mK for UHMW (Technical Products Inc., 2018). Thermal breaks were placed midway along the length of the specimens. Holes were pre-drilled in the thermal break so that longitudinal rebars could pass through it. The objective was to compare the thermal and structural performance of these thermal breaks and find the most suitable material for use with GFRP reinforced balcony slabs. Figure 5 shows the dimensions of thermal breaks for the nine specimens.

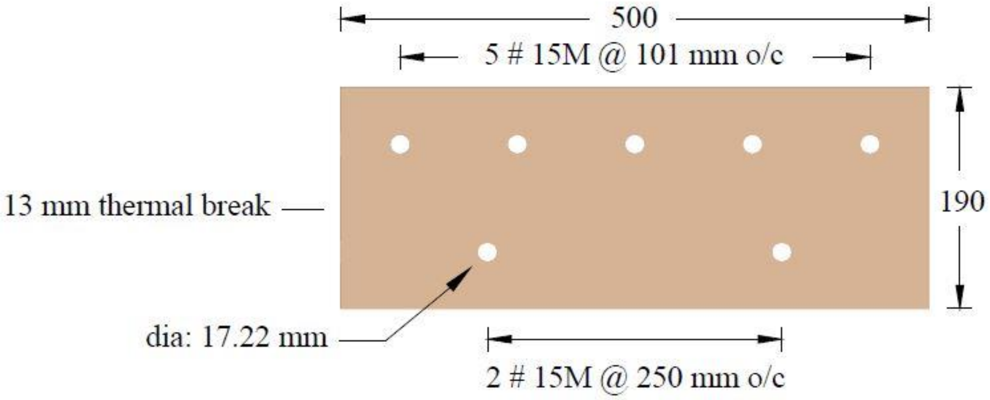

Figure 5 Thermal break dimensions

3.2.3 Reinforcement

All GFRP rebars for this study were donated by Pultrall (2018) which also provided their properties summarized in Table 13.

Table 13 Rebar properties (Pultrall, 2018)

GFRP Rebar	Effective Diameter [mm]	Effective Area [mm^2]	Ultimate Tensile Strength [MPa]	Tensile Modulus [GPa]
#15M	17.22	232.9	1100	60

Three #15M GFRP rebars with the length of 2160 mm were separately tested in tension under a static monotonic load. Test results are shown in Table 14. Based on Annex B of CSA S806 (2017), the anchor and total length of GFRP required for testing in tension is calculated as:

$\mathrm{d} = 17.22\ \mathrm{mm}$ nominal diameter of specimen

$\mathrm{A} = 232.9\ \mathrm{mm}^2$ cross sectional area of specimen

$\mathrm{f_u} = 1100\ \mathrm{MPa}$ ultimate tensile strength

$\mathrm{L_g}$ should not be less than 250 mm. Length of grip is:

$$\mathrm{L_g} = \frac{\mathrm{f_u} \times \mathrm{A}}{350} = \frac{1100 \times 232.9}{350} = 732\ \mathrm{mm} > 250\ \mathrm{mm}$$

Total length of GFRP specimen:

$40\ \mathrm{d} + 2\ \mathrm{L_g}$ or greater $= 40\ (17.22\ \mathrm{mm}) + 2(732\ \mathrm{mm}) = 2152.7\ \mathrm{mm} \sim 2160\ \mathrm{mm}$

Note: To enhance gripping, according to the clause B.3.4.1 of CSA S806 (2017), a 2 mm projection of the cross bars should be left while cutting the specimens.

Table 14 GFRP rebars tensile test results

GFRP Rebar No.	$\mathrm{f_u}$ [MPa]	$\mathrm{f_u}$ Average [MPa]	ε_u	ε_u Average	E Average [GPa]
1	854	970	0.02010	0.02250	43.1
2	984		0.02386		
3	1071		0.02354		

The materials are linear elastic until failure; hence they do not yield. This behaviour can be seen in Figure 6 from the results of testing three #15M GFRP rebars in tension.

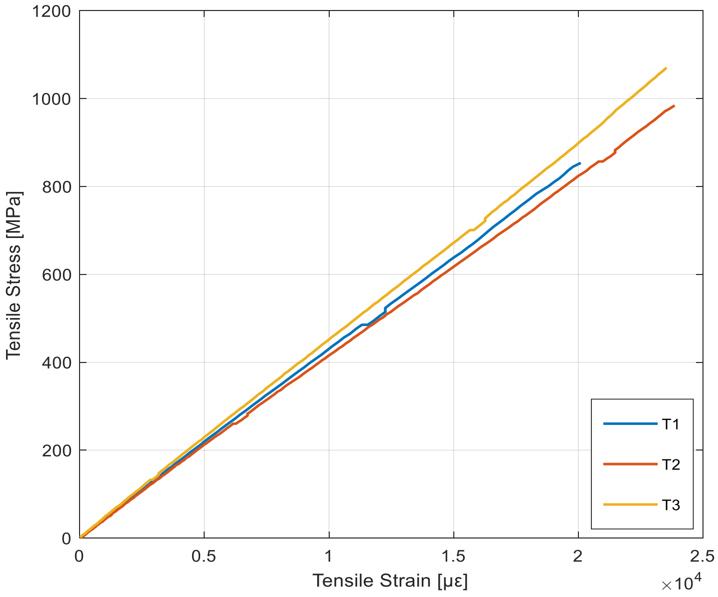

Figure 6 Three GFRP rebars tested in tension

3.3 Instrumentation

A total of six strain gauges (350 ohm) were used in each specimen. Three were installed on the middle top tension rebar: One at the position where the rebar crossed the thermal break, halfway through the thermal break thickness, and two others 30 mm away on each side of the thermal break. The other three strain gauges were installed on one of the bottom rebars. These were installed at the same positions and distances from thermal break as the top ones. The location of the strain gauges is shown in Figure 7.

Naming convention for strain gauges was as follows; the support side of the slab was labeled north (N), the middle of the slab was denoted as M, the cantilever side was labeled south (S). T stands for top, B for bottom. There were two longitudinal sections in each slab called AA and BB. Section AA is along the bottom rebar, and section BB is along the middle top rebar as shown in Figure 7. As an example, ST-BB means south top gauge in the BB section. The data from strain gauges were plotted as strain [µε] versus load [kN]. Reinforcement sketches are shown in Figure 8.

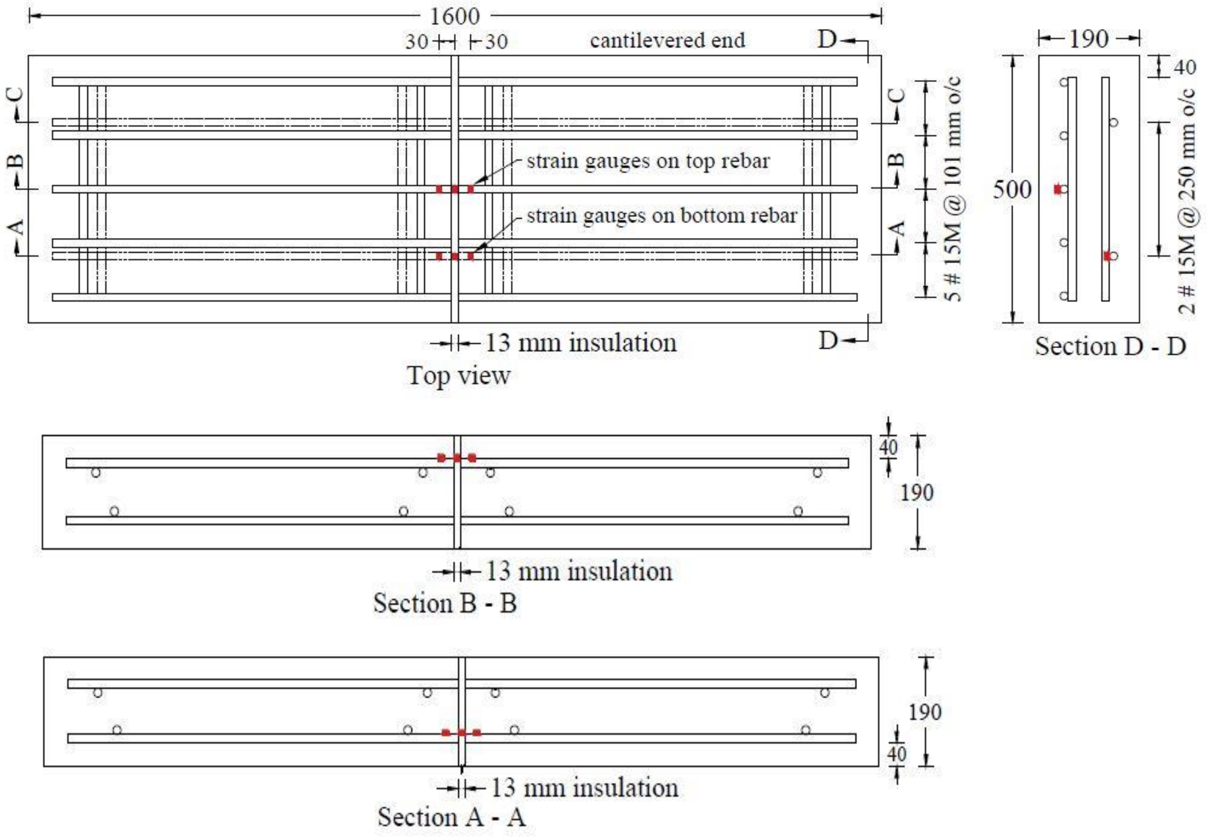

Figure 7 Location of strain gauges on specimens shown in red dots

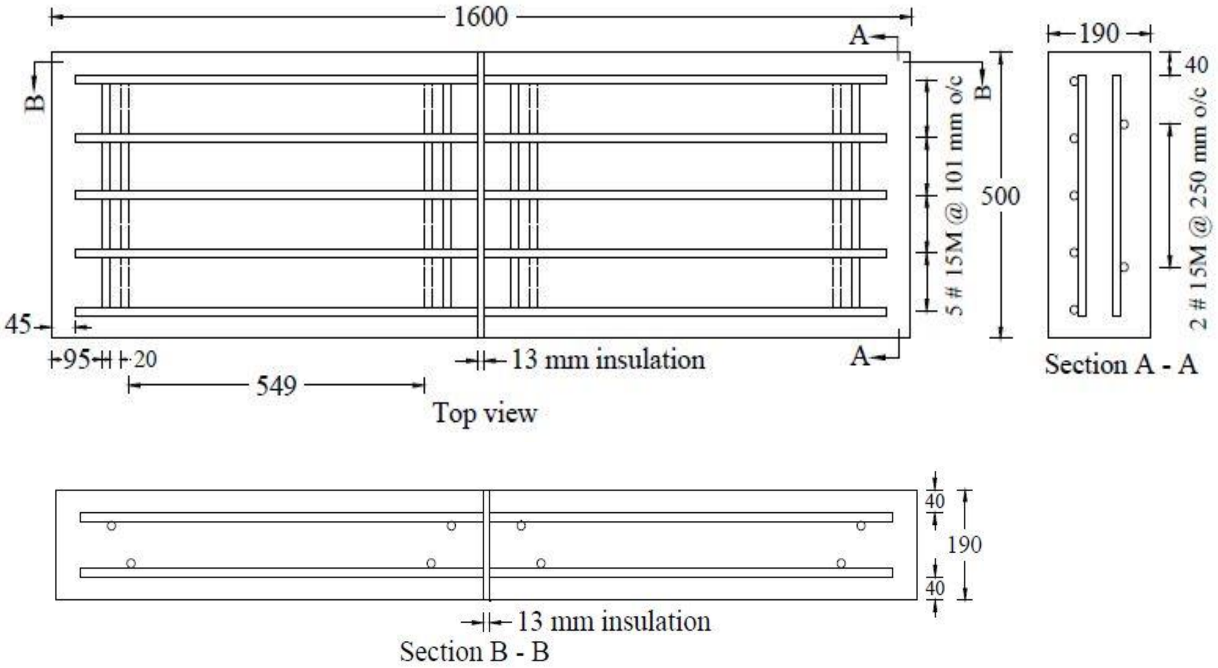

Figure 8 GFRP reinforced slab

The reason for choosing the above-mentioned locations for strain gauges was to measure strains at the locations of maximum moment.

Before installing strain gauges, the surface of the GFRP rebar was ground. The surface was then cleaned with alcohol. Strain gauges were glued on the rebar and then covered with Nitrile Rubber Coating and left for about 20 minutes to dry. They were then covered with a transparent tape and covered with epoxy coating. Sand coating was spread on top of epoxy immediately to increase roughness and improve bond with concrete.

The purpose of using PI gauges is to measure the strain and crack widths on concrete as well as to measure the dilation between the concrete and thermal break. A total of four 200 mm PI gauges were used for each slab. One PI gauge was installed in the tension area on top of the west side, and another PI gauge was installed in compression at the bottom of the west side. The same PI gauge arrangement was used on the east side.

On the west side the top and bottom PI gauges, named PI gauges 4 and 3 respectively, were installed just behind the thermal break, to the support side of the slab (north). For the east side the top and bottom PI gauges, named PI gauges 1 and 2 respectively, were installed such that they crossed the thermal break towards the support part of the slab. See Figure 9 for a drawing of PI gauge arrangement on all nine specimens.

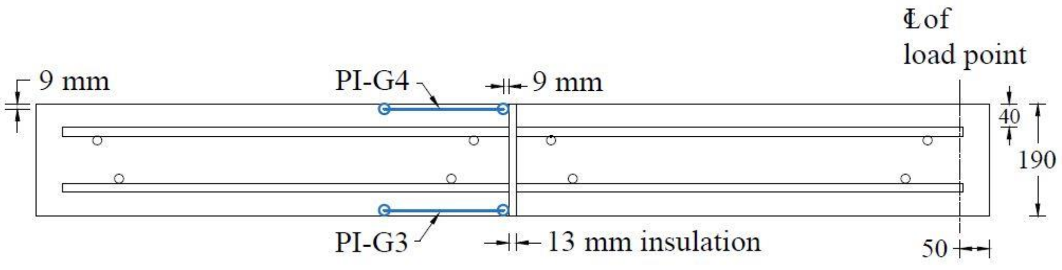

West edge - PI gauges behind thermal break

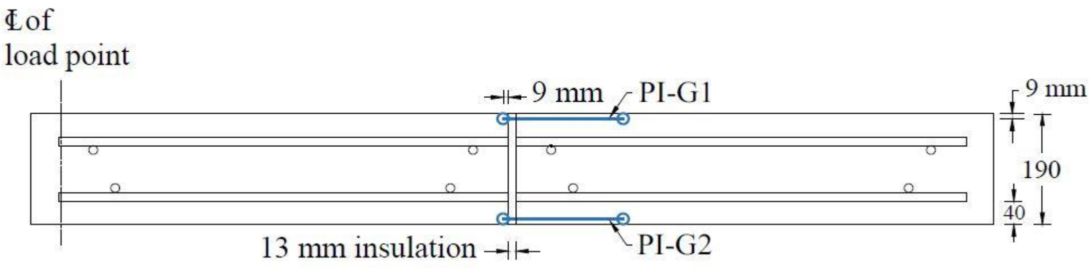

East edge - PI gauges crossing thermal break

Figure 9 Drawing of PI gauge arrangement

To install a PI gauge on concrete at the sides of the slab, two bolts (18 mm in diameter) were glued to the concrete first. Epoxy was applied under the bolts and on concrete to fix them in place. Then the 200 mm PI gauge was placed between washers and nuts such that they are able to move and capture the changes in length between the two bolts.

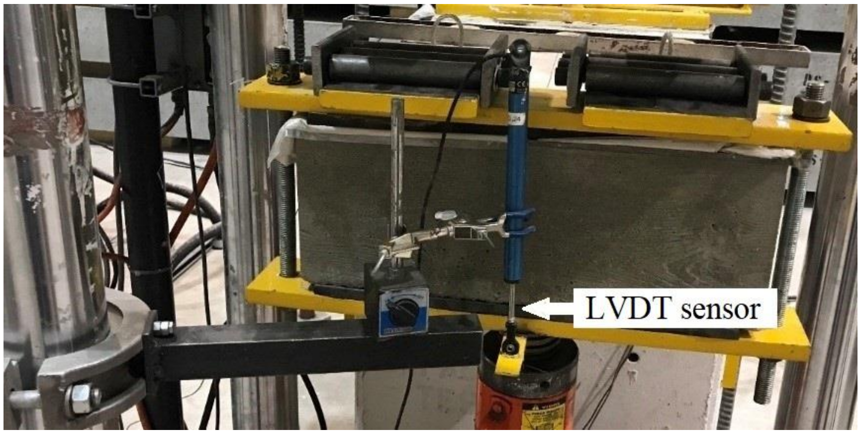

Figure 10 Location of LVDT

Linear Variable Deflection Transducer (LVDT) sensors measured the vertical displacement of the slab due to the applied load. For all specimens, an LVDT was installed at the cantilever end, 90 mm away from the load point, to measure the deflection/displacement of the cantilever tip. The test was carried out under deflection control and was set at 2 mm/minutes. Figure 10 shows the position of the LVDT. Figure 11 shows the slab side naming as well as the locations of the two supports.

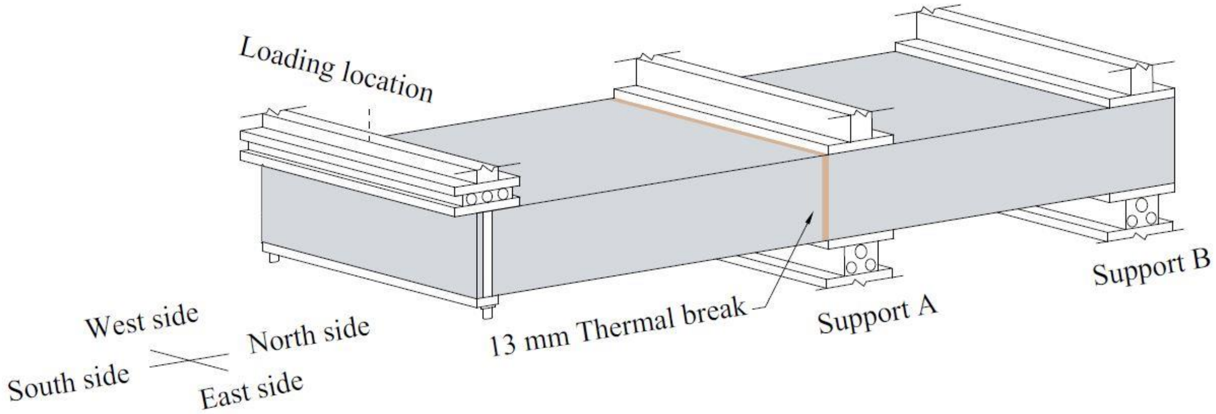

Figure 11 Naming of slab sides, supports and location of load at the tip of the cantilever slab

3.4 Preparation of Specimens Before Casting

Formworks were built for specimens prior to casting. Next, strain gauges were installed on top and bottom rebars prior to making reinforcement cages. Openings for threading the GFRP bars through were drilled through the thermal break, five in the top layer and two at the bottom layer. Rebars were passed through the openings. Cages for the nine specimens were built from #15M GFRP rebars: Five rebars on top and two on bottom, and eight transverse rebars. To connect the rebars into a reinforcement cage, plastic zip ties were used. Plastic rebar chairs were used to provide the rebars with the required concrete cover: Eight 133 mm and eight 40 mm chairs were used for that purpose in each slab. The inside thermistors were installed in two layers. One layer was placed on top of the GFRP rebars (three thermistors on each side of the thermal break), and the second layer was suspended between the top and bottom rebars (9 thermistors on each side of the thermal break). Strain gauges and thermistors were labeled. The inside of the formworks was coated using a release agent. Finally, reinforcement cages were placed into the formworks.

In order to have zero bending moment at the thermal break while lifting the slab, two lifting cables were placed symmetrically at a distance of 40 cm from thermal break. Thus, four lifting cables were used per slab. Each cable had a length of 70 cm and a diameter of 6 mm. Each lifting cable was tied using zip ties to the top longitudinal rebar. To make sure lifting cable is well anchored in the concrete, the wires at the ends of the cable were unravelled and spread out. See Figure 12 for clarification.

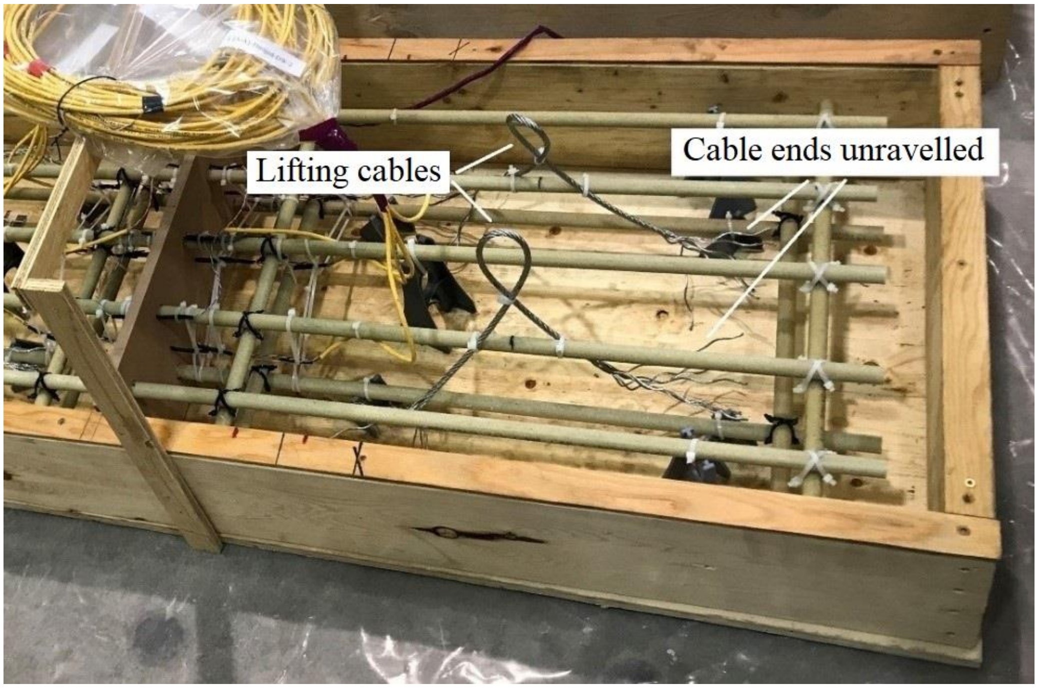

Figure 12 Lifting cables

In order to keep the thermal break from moving during the cast, a piece of wood was temporarily fixed on top while pouring concrete. It was removed immediately after concrete pouring was completed. See Figure 13 for details. Due to the presence of inside thermistors, pouring of concrete and vibration were done with extra caution. In order not to damage the thermistors, vibration was not used directly in the portion of the slab with the highest concentration of instrumentation, but was done at a distance of more than 200 mm from the thermistors.

After casting, the slabs and cylinders were covered by plastic sheets to prevent early-age cracks. After 24 hours the plastic sheets were removed and the specimens were covered with wet burlaps. To subject the cylinders to the same curing conditions as the slabs, they were covered with similar wet burlaps for seven days.

Figure 13 Temporary “fixer” for thermal break during cast

3.5 Test Setup

The test setup for all specimens was the same as the one used in Phase I of this program (Boila, 2018). During structural tests, the slab and the support gear were placed on two large (650 mm x 650 mm) concrete blocks. Two rollers on top of the concrete blocks supported the slab and allowed for its rotation. As shown in Figure 14, one roller (support A) was in the middle of the slab right behind the thermal break, and the other roller (support B) was at the far end of the slab, simulating the inside part of the balcony.

Three jacks were used to apply downward pressure on the slab at the supports to stabilize the slab during loading. One was in the middle, above roller support A, and the other two were above support B. The support A was assumed to have a negative moment due to the applied point load at the free end of the cantilever. The aim of this support was to simulate a wall between the balcony and the inside section of the slab, as well as to prevent the rotation of the slab. The aim of jacks at support B was to prevent the slab from being moved upward due to the downward point load that was applied at the tip of the cantilever during test. The jacks and supports at points A and B helped to fix the specimen in place during test. The test setup is shown in Figure 14.

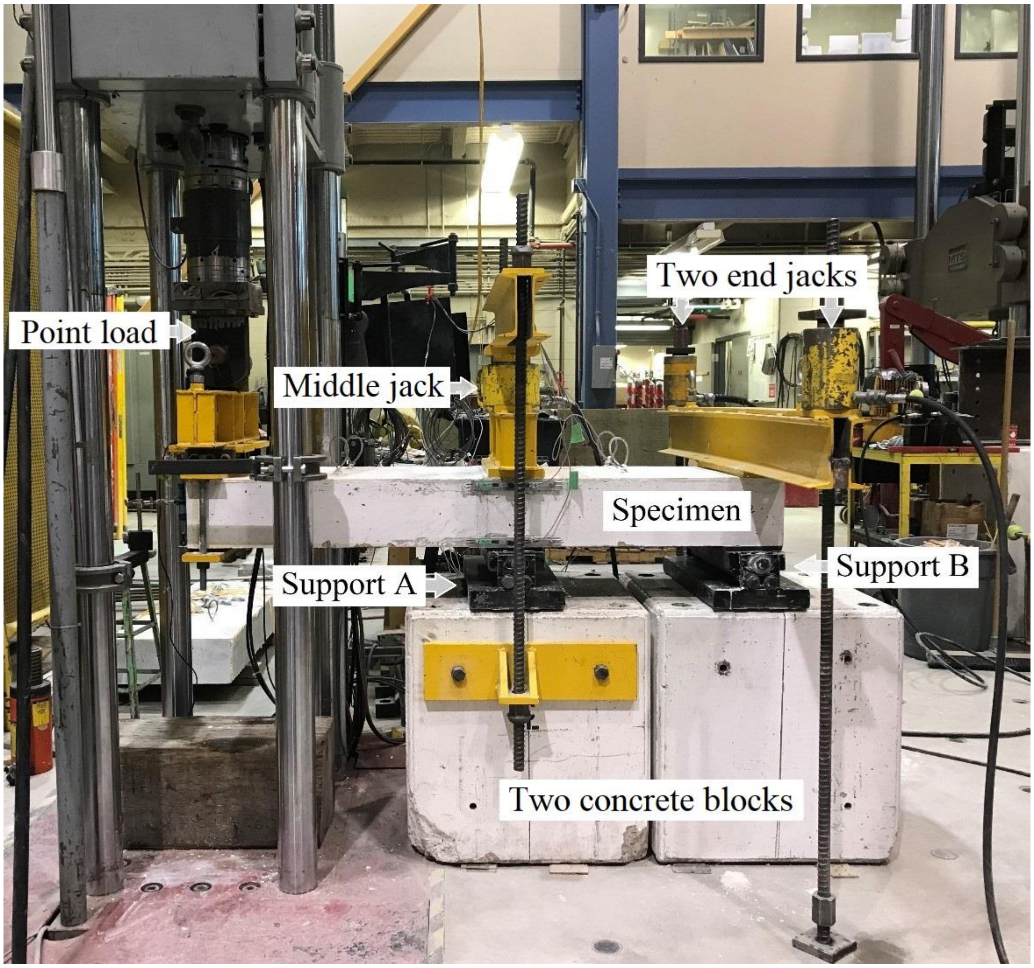

Figure 14 Support setup during structural test

A line load was applied in the downward direction at the tip of the cantilever and spread evenly across the width of the slab tip using a 50 mm wide steel plate. The steel loading plate was placed on top of a 10 mm thick neoprene pad over the entire width of the slab.

The next chapter outlines the results which were obtained from the structural testing program, as well as interpretations of these results.

Chapter 4 Structural Results and Analysis

This chapter includes the results and analysis of structural testing of the nine specimens. The results are presented for each specimen in terms of strain in the rebars, strain on concrete surface, and deflection under monotonic load at the tip of the cantilever.

All specimens were tested structurally to failure by the application of a static monotonic load at the tip of the cantilever.

4.1 Strains in Reinforcement

The naming convention that was used for strain gauges, can be found in section 3.3. Table 15 shows the naming convention and grouping for specimens, and their ultimate load.

Table 15 Grouping of specimens based on thermal break

Specimen #	Specimen ID	Type of Thermal Break	Failure Load (kN)
1	AR1	Armatherm™ 500	75
2	AR2		63.5
3	AR3		65
4	DOW1	DOW	82
5	DOW2		82.5
6	DOW3		80
7	UHMW1	UHMW	82
8	UHMW2		75
9	UHMW3		78

Figure 15 shows the strain gauge data for the AR specimens, that is, specimens with Armatherm™ 500 thermal break. In Figure 15, all plots were terminated at the failure load for each slab. In each slab the positive values from the three strain gauges which were installed on top rebar (namely ST, MT, NT) show that this rebar was in tension throughout the loading.

Before the first crack was observed at loads of about 18 kN, the strain gauges on the compression rebar have negative values for all the specimens shown in Figure 15. This is because the bottom rebars were in compression. The values changed to positive after the first crack occurred. The bottom rebars started to act in tension because the neutral axis surpassed them, and moved closer to the extreme compression fibre. It is well known that the depth of compression zone in GFRP reinforced concrete reduces significantly after cracking.

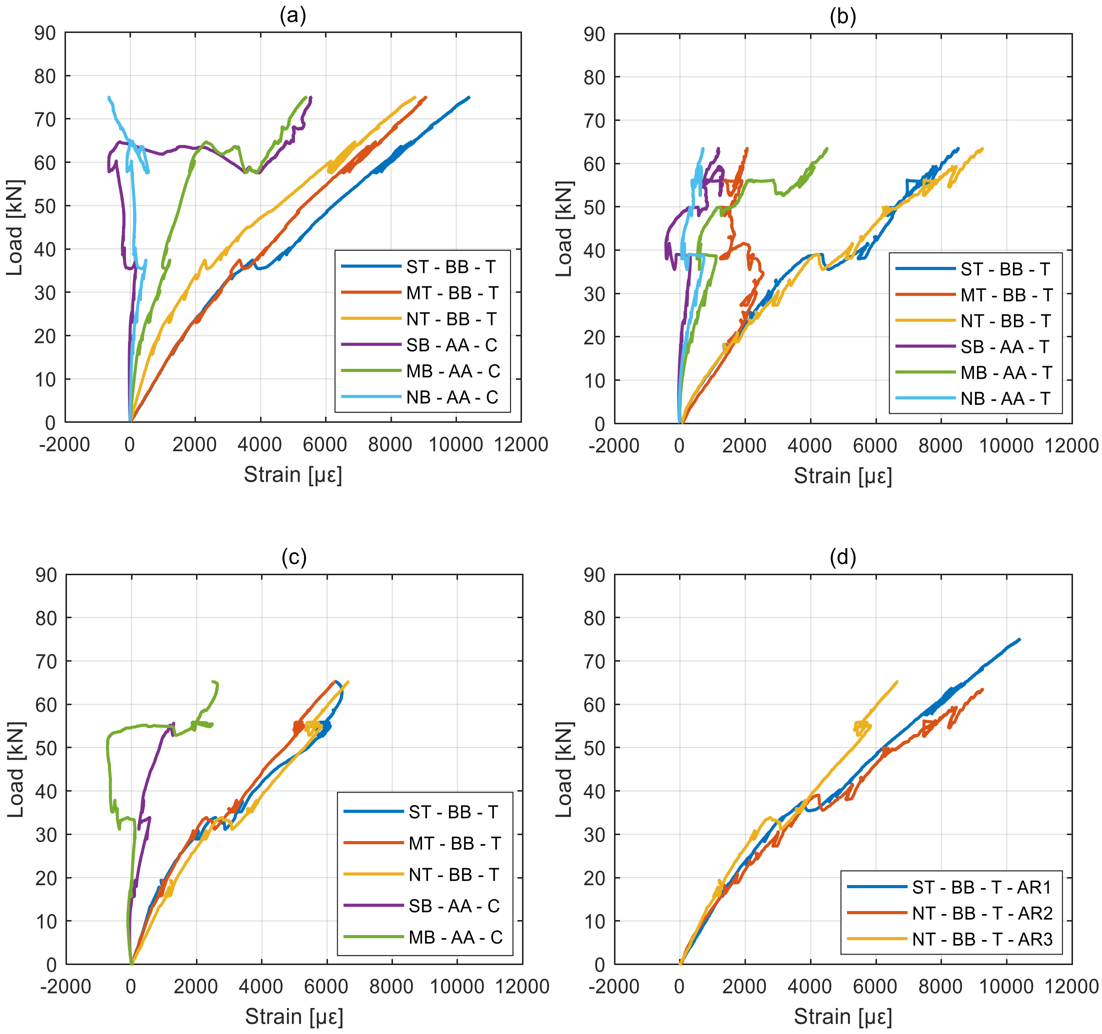

Figure 15 Strain in reinforcement at the maximum moment location: (a) AR1, (b) AR2, (c) AR3 and (d) maximum strains from all AR specimens

As seen in Figures 15 (a), (b) and (c), for all three specimens AR1, AR2 and AR3 both the top and bottom strain gauges show linear elastic deformation until loads of about 37 kN, 38 kN, and 34 kN respectively. Some fluctuating elastic deformation without increase in load around these loads is a sign of dilation increase between the concrete and the thermal break, or compression of the thermal break. This was accompanied by increase in compression strain recorded on the compression rebars. Afterwards, linear elastic deformation continues until second plateau at loads of 65 kN, 55 kN, and 55 kN for the slabs AR1, AR2 and AR3 that most likely represent the compression deformation in the thermal break prior to the slab failure.

A direct comparison of the results from the three AR specimens is shown in Figure 15 (d): The plots show linear elastic behaviour up to the first crack for each slab. The three maximum strain plots have a consistent behaviour in tension. However, the AR1 specimen shows the largest strain in the instrumented rebar.

Figure 16 shows strain gauge data for DOW specimens. In Figure 16 all plots were terminated at the failure load for each slab.

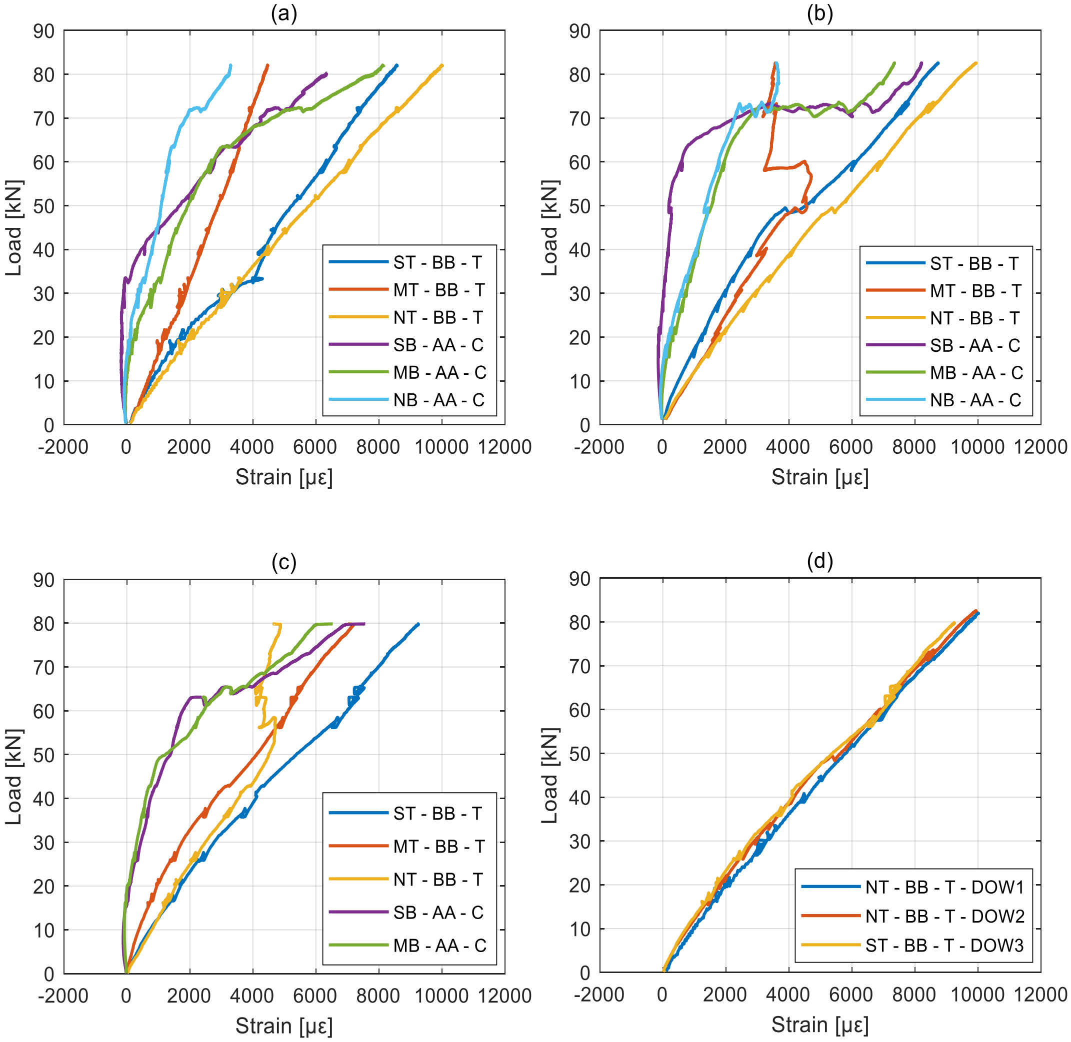

Figure 16 Strain in reinforcement at the maximum moment location: (a) DOW1, (b) DOW2, (c) DOW3 and (d) maximum strains for all DOW specimens

As seen in Figures 16 (a), (b), and (c) the neutral axis of all specimens shifted at around 10 kN to a location below the compression reinforcement, closer to the maximum compressive fiber in the cross section. This is clear from Figure 16, because the bottom rebars started to act in tension. For DOW3 in Figure 16 (c), the NB gauge did not work properly, and therefore there are no data for it.

For all three specimens DOW1, DOW2 and DOW3 tension rebars show linear elastic deformation throughout the loading. Contrary to the AR specimens, the signs of compression of the thermal break due to load are less pronounced. In slab DOW2 this was the most visible with sudden increase in strain under constant load in the bottom rebar at load of 70 kN. Smaller signs of compression can be shown in slab DOW1 at 71 kN, and in slab DOW3 at 63 kN. In the tension rebar, there is a notable change in the direction of the strain in slab DOW2 at 50 kN in the strain gauge that was placed in the area of the thermal break, and also in the gauge that was on the cantilever end of the slab. The crack width that was measured at that location suddenly increased from 0.2 mm to 0.5 mm between the loads of 40 kN and 60 kN, when those measurements took place. This explains the erratic measurements from strain gauge MT-BB-T in DOW2 after 50 kN. There is some limited disturbance in the load-strain behaviour at 34 kN for DOW1, and 43 kN for DOW3.

The maximum strains for all DOW specimens are shown in Figure 16 (d). For all slabs the plots show linear elastic behaviour up to failure. The behaviour of these three specimens was nearly identical, as shown in Figure 16 (d).

Figure 17 shows strain gauge data for UHMW specimens. In Figure 17 all plots were terminated at the failure load for each slab. In all three slabs the three strain gauges ST, MT, NT which were installed on top rebars show positive values which indicates that those rebars were in tension. The behaviour of the specimens was similar to the DOW specimens, with no notable changes in the slope of the tensile strain plots throughout the loading. The specimens' neutral axis shifted to the outermost compression fibre and caused the two layers of reinforcement to be in tension after approximately 20 kN.

The bottom strain gauges show linear elastic deformation until loads of about 74 kN, 72 kN, for UHMW1 and UHMW2 specimens in Figures 17 (a) and (b). The behaviour of bottom strain gauge for UHMW3 in Figure 17 (c) is somewhat different: While MB and NB show elastic linear deformation until a load of 70 kN, SB shows linear elastic deformation until a load of 53 kN. After reviewing the measurements of dilation for the specimen, it shows that the dilation in UHMW3 doubled between 40 kN and 60 kN, which is most likely the reason for this change in strain at that strain gauge, NB is the farthest from the loading point and shows the least deformation. See Figure 17 (c). All UHMW specimens show signs of increased tensile strains without increase in load after 70 kN, which most likely was caused by the compression in thermal break.

Figure 17 (d) shows the comparison of the three maximum strain plots from each of the UHMW slabs. The plots indicate that all specimens displayed a similar behaviour in tension.

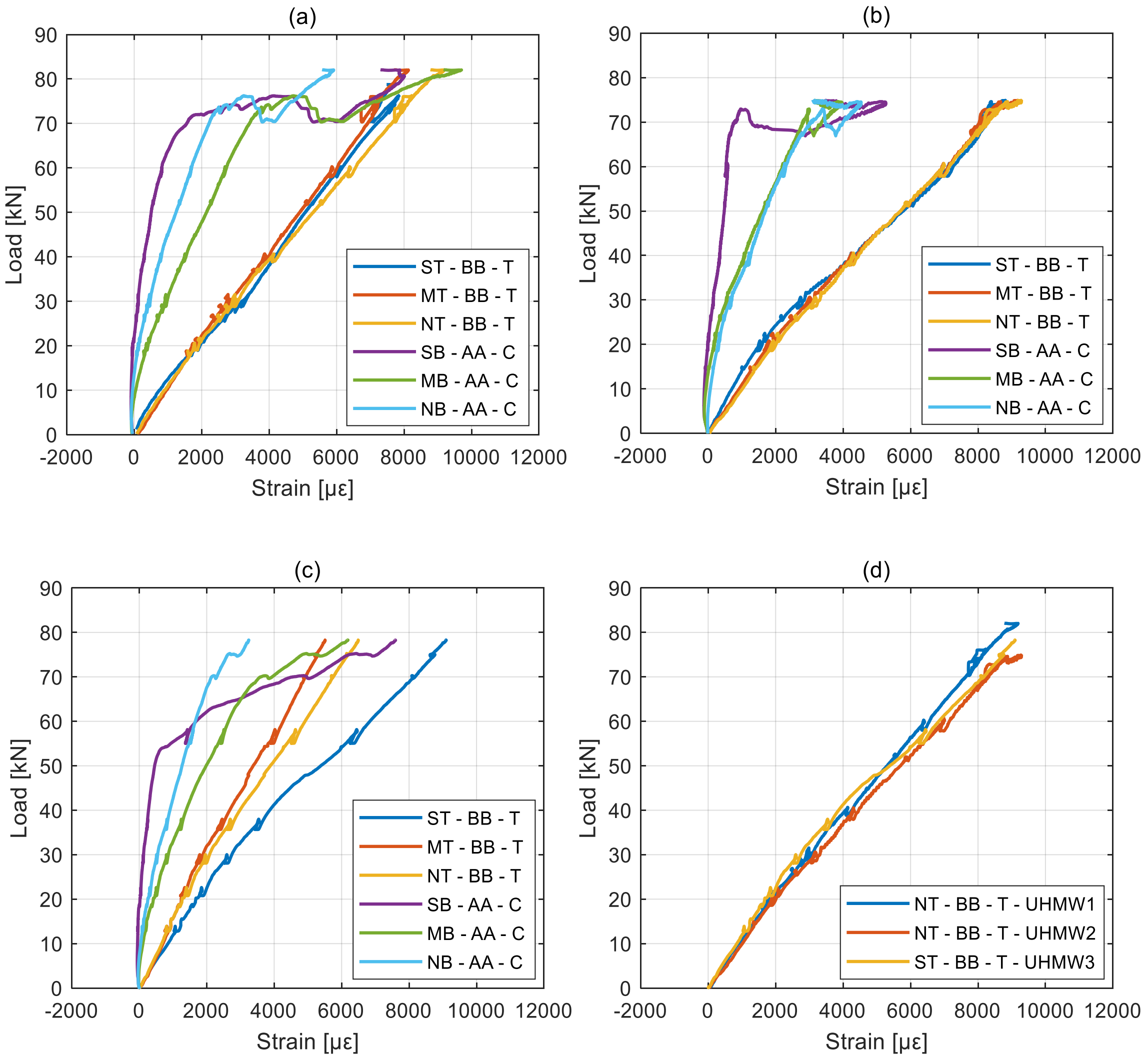

Figure 17 Strain in reinforcement at the maximum moment location: (a) UHMW1, (b) UHMW2, (c) UHMW3 and (d) maximum strains for all UHMW specimens

4.2 Concrete PI Gauge Results

The data from PI gauges were plotted as elongation or contraction [strain] versus load [kN]. On each of the specimens, two PI gauges per slab side were installed: PI gauges 1 and 4 were in tension (on the top) and PI gauges 2 and 3 were in compression (at the bottom). Moreover, PI gauges 1 and 2 were installed on the east side, and 3 and 4 were installed on the west side of each slab.

PI gauges 1 and 2 had the thermal break within their gauge length, and therefore were recording the dilation at the thermal break-concrete interface (PI gauge 1), and compression of the thermal break (PI gauge 2). Each PI gauge graph was terminated at failure load.

Figures 18 (a), (b), and (c) show PI gauge data for the AR specimens, and Figure 18 (d) shows a direct comparison of the maximum elongation in the three AR slabs tested in this program. The aim of installing PI gauges was to record the deformation in concrete in the vicinity of the thermal break. All graphs in AR1 shown in Figure 18 (a) except PI-G3 are linear up to a load of about 37 kN followed by a more rapid deformation increase, and a second noticeable increase in deformation at the load of 60 kN that is mostly due to thermal break compression. From the deformation observed in PI-G3, that only shows a vertical graph with no increase in deformation after 20 kN, it was concluded that this PI gauge was not working properly. The thermal break began to compress more rapidly at the load of 60 kN, which was followed by a sharper decrease in stiffness of the recorded deformation. It is also noted that the same events were reflected on the rebar strain graphs shown in Figure 15 (a). This means that the onset of dilation between the concrete and the thermal break led to increased strains in the GFRP bars at that location. Figure 18 (a) also shows that the neutral axis shifted drastically, but remained between the location of the PI gauge in compression and the compression reinforcement until failure. The amount of elongation at the top was +0.01361 and the amount of contraction was -0.01359 at the bottom of the slab. These largest values were recorded in the two gauges that were installed with the thermal break in the gauge length, PI-G1 and PI-G2.

All four deformations shown for AR2 in Figure 18 (b) are linear up to a load of about 38 kN, followed by a more rapid deformation increase, especially in compression. This indicates that the thermal break began to compress more rapidly at that load, which was the case with the slab AR1. The maximum amount of elongation at the top of this slab was smaller than in slab AR1 and was equal to +0.00877 and the amount of contraction was -0.00695 at the bottom of the slab. These largest values were recorded in the two gauges PI-G1 that was installed with the thermal break in the gauge length, and PI-G3. The onset of visible compression on the bottom of the slab and dilation in the tension at the top of the slab started in slab AR3 at 34 kN, which is very consistent with the data obtained from slabs AR1 and AR2. Further compression of the thermal break is visible in Figure 18 (c) at 55 kN. The amount of elongation at the top was +0.00607 and the amount of contraction was -0.01664 at the bottom of the slab. These largest values were recorded in the two gauges that were installed with the thermal break in their gauge length, PI-G1 and PI-G2.

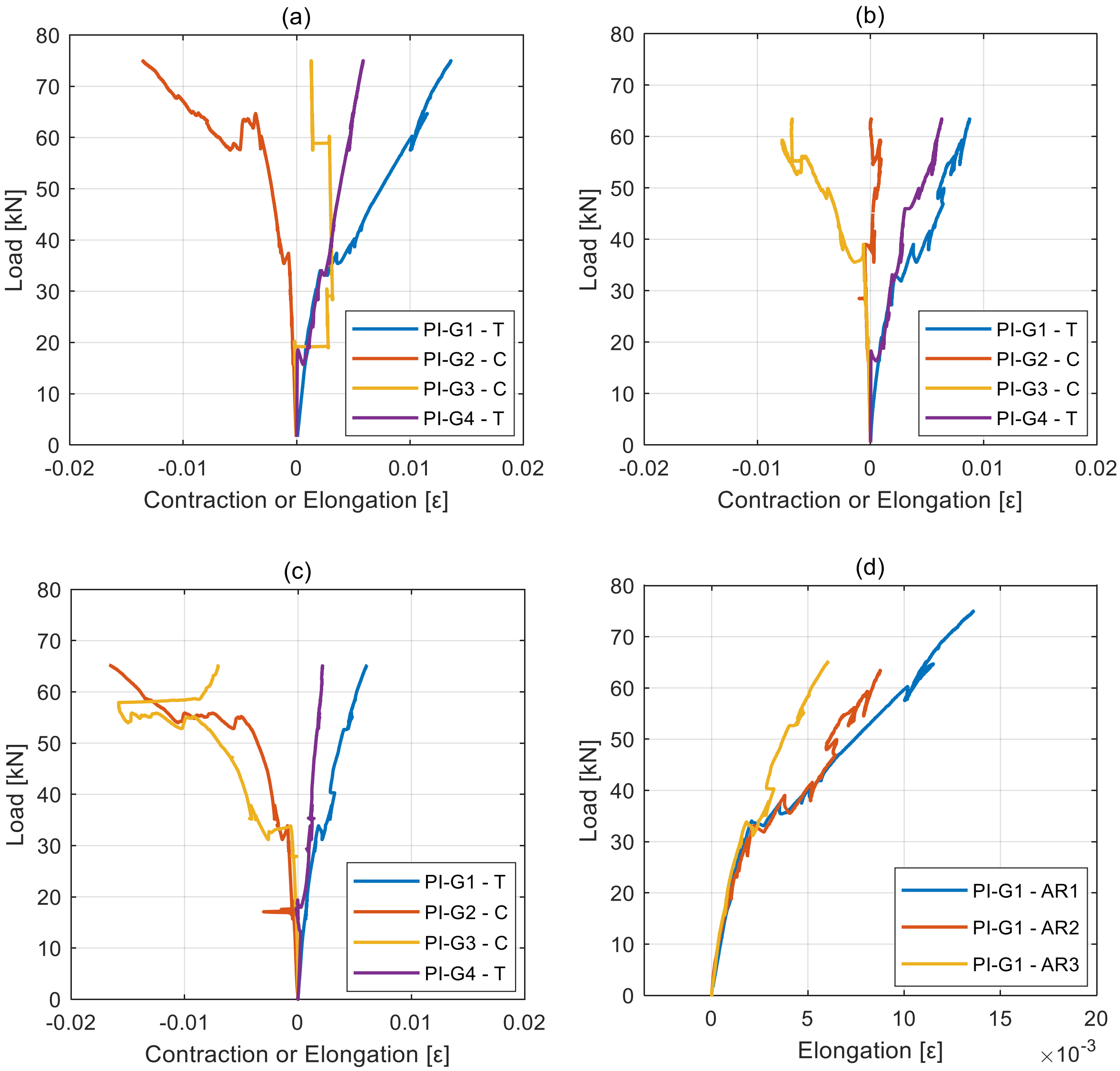

Figure 18 Contraction and elongation in concrete at the thermal break location: (a) AR1, (b) AR2, (c) AR3 and (d) maximum elongation from all AR specimens

Maximum elongation in the three AR slabs is plotted in Figure 18 (d). The graph shows consistent onset of dilation, or debonding from the thermal break, shortly after 30 kN. The three lines for the three specimens then deviate throughout the loading until failure.

Figure 19 shows PI gauge data for the DOW specimens.

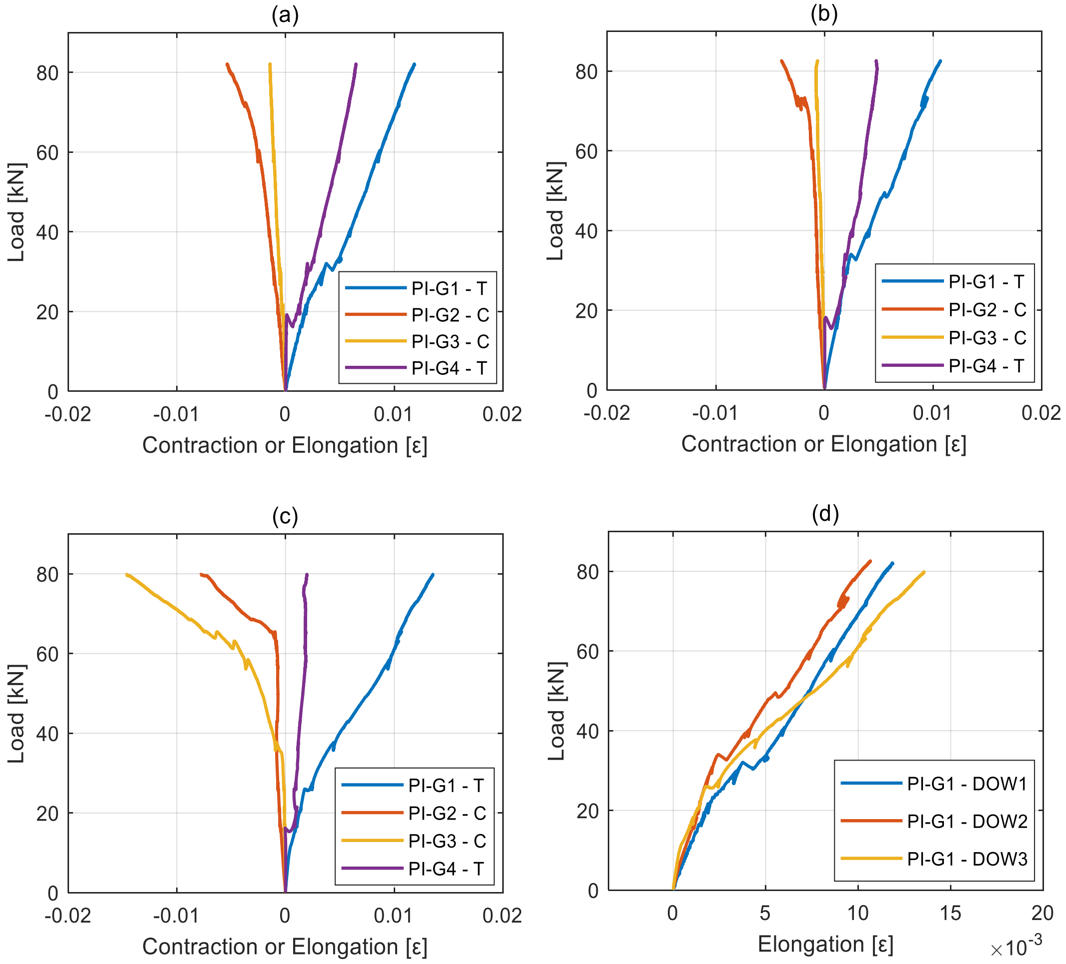

Figure 19 Contraction and elongation in concrete at the thermal break location: (a) DOW1, (b) DOW2, (c) DOW3 and (d) maximum elongation from all DOW specimens

When Figure 19 is compared with the recorded rebar strains in Figure 16, there is much less similarities between the two compared to what was found for the AR specimens. There is a small dip in the strains measured by PI-G1 that corresponds to the similar dip in strain in strain gauge ST-BB-T in slab DOW1 at around 30 kN. In compression, it can be seen that the compressibility of the DOW break is smaller compared to Armatherm, as the strain increase in the PI-gauge measurement is much smaller for DOW slabs. It is only noticeable for slabs DOW2 from gauge PI-G2-C at 70 kN and DOW3 from both compression PI-gauges at a load of 63 kN. In tension, however the early onset of dilation between the thermal break and concrete was reflected by visible drops in the strain values at the time of first dilation at around 20 kN for all specimens.

Maximum elongation in the DOW slabs is plotted in Figure 19 (d). The graph shows that DOW1, DOW2 and DOW3 reached the maximum elongation of 0.01189, 0.01066 and 0.01358, respectively. The average elongation for the three DOW slabs is 0.01204.

Figure 20 shows PI gauge data for the UHMW specimens. For UHMW1, PI-G2 and PI-G3 show linear behaviour up to 70 kN, past which they show rapid deformation which is due to thermal break compression at that load. From Figures 20 (a) and 20 (b), it can be seen that UHMW thermal break has a relatively low compressibility, compared to Armatherm discussed previously. UHMW only starts to show visible compression at a load of about 70 kN.

It can be seen that the rapid increase in contraction at 75 kN in Figure 20 (a) corresponds to the onset of a strain plateau in GFRP rebars in Figure 17 (a). Apart from this similarity, it can be seen that the compressive deformation as measured using PI gauges in UHMW slabs did not reflect the strain recorded in the GFRP bars. This behaviour is similar to that of the DOW slabs discussed earlier, and is clear in slab UHMW1 and the response from PI-G2.

The tension behavior in Figures 20 (a), (b) and (c) measured by PI-G1 and PI-G4 is different. The onset of dilation between the thermal break and the concrete was recorded at 19 kN, 15 kN and 16 kN respectively for slabs UHMW1, UHMW2 and UHMW3. Overall, PI-G1 and PI-G4 show relatively rapid elongation after these loads, which is due to the early onset of dilation between the thermal break and concrete.

The maximum elongation in the UHMW slabs is plotted in Figure 20 (d). The graph shows that UHMW1, UHMW2 and UHMW3 reached the maximum elongation of 0.01328, 0.0155 and 0.00754, respectively. The average elongation for the three UHMW slabs is 0.01211.

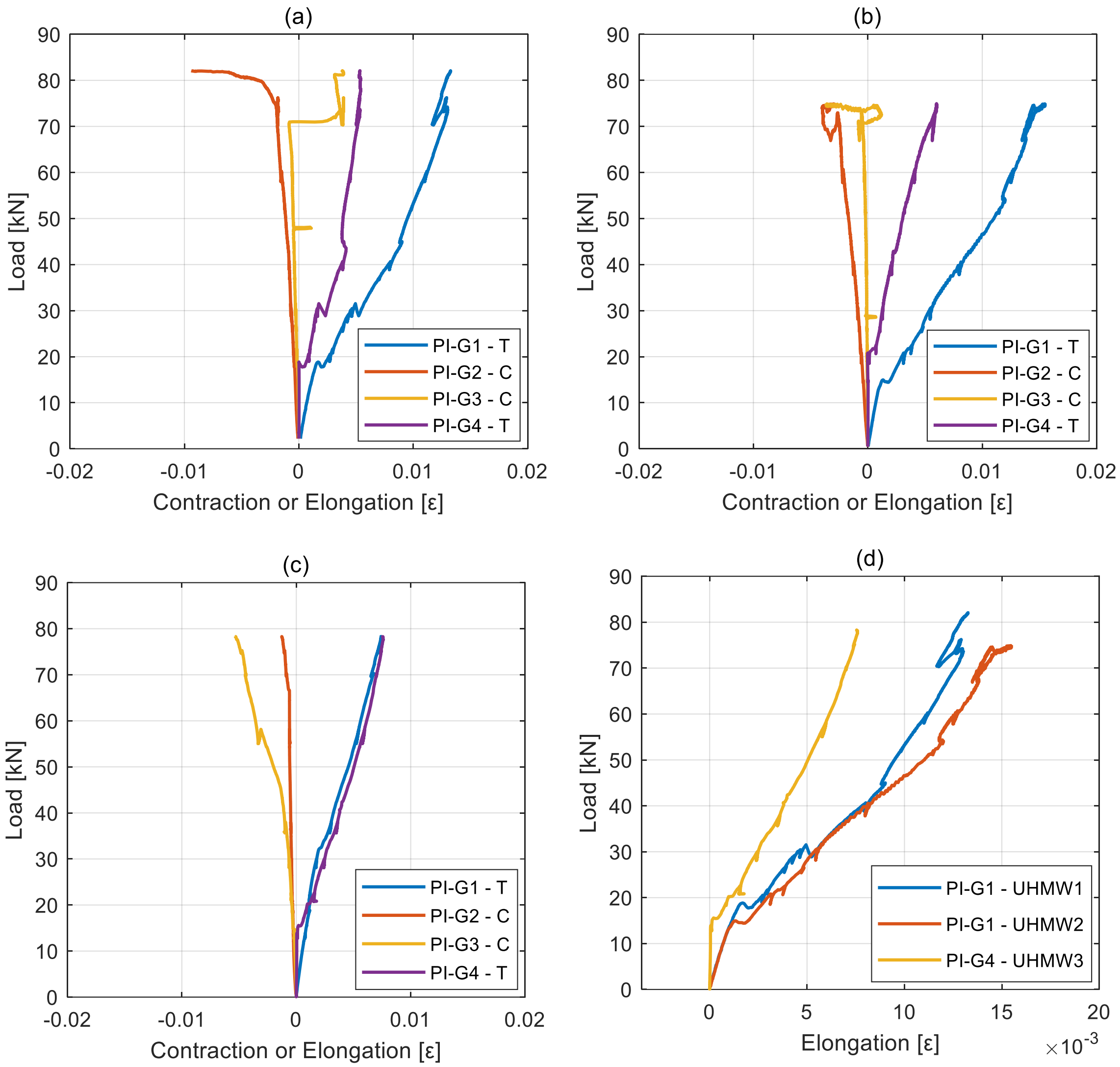

Figure 20 Contraction and elongation in concrete at the thermal break location: (a) UHMW1, (b) UHMW2, (c) UHMW3 and (d) maximum elongation from all UHMW specimens

The dilation between the thermal break and concrete was calculated by subtracting PI-G4 from PI-G1 and plotted as shown in Figure 21. The dilation between the thermal break and concrete is clearly shown to initiate at 19 kN for slabs AR, at 18 kN for slabs DOW and at 17 kN for slabs UHMW. The data are very consistent in the three specimens for each slab type. This onset can be delayed if bond agents were used at the interface.

The largest total dilation on each side of the thermal break for AR slabs was 1.56 mm at a load of about 75 kN. For DOW slabs the largest dilation was 2.33 mm at a load of about 80 kN. For UHMW slabs the largest dilation was 1.91 mm at a load of about 75 kN.

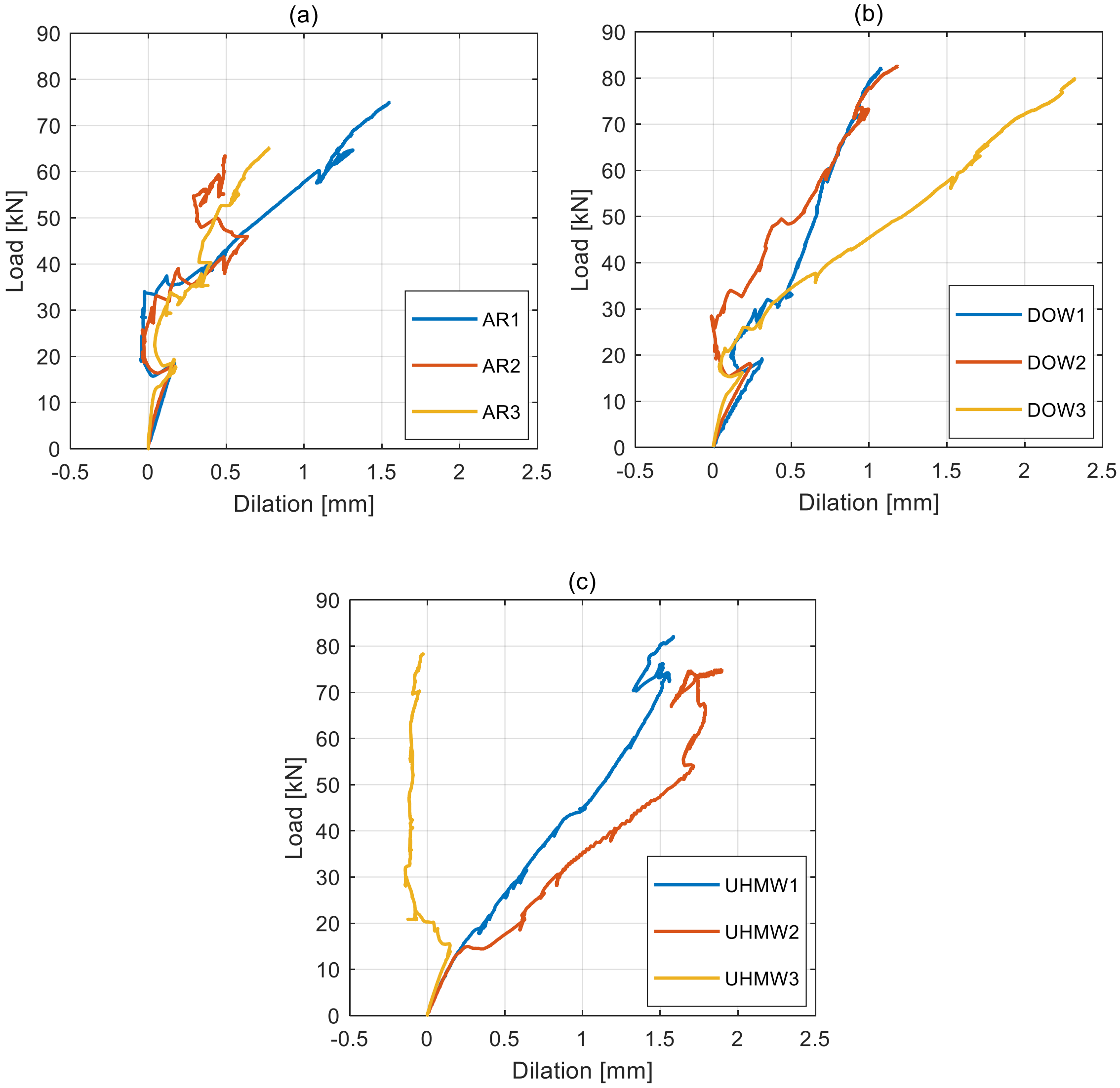

Figure 21 Dilation between concrete and thermal break at the maximum moment location: (a) AR, (b) DOW and (c) UHMW

4.3 Load Deflection Response

The data from LVDT were plotted as deflection [mm] as a function of load [kN]. The LVDT was installed at the tip of the cantilevered end of each slab, and monitored the deflection of the bottom of the slab.

Figure 22 (a) shows the load-deflection curves for AR slabs. The first drop in the curve indicates cracking of the slabs that occurred at 18.5 kN, 18.3 kN and 17.8 kN for AR1, AR2 and AR3, respectively. The failure loads were 75, 63.5, and 65 kN for AR1, AR2 and AR3 respectively.

Figure 22 (b) shows the load-deflection curves for DOW slabs. The first drop in the curve indicates cracking of the slabs that occurred at 19 kN, 18.2 kN and 16 kN for DOW1, DOW2 and DOW3 slabs, respectively. The failure loads of the slabs were 82, 82.5, and 80 kN for DOW1, DOW2 and DOW3 respectively.

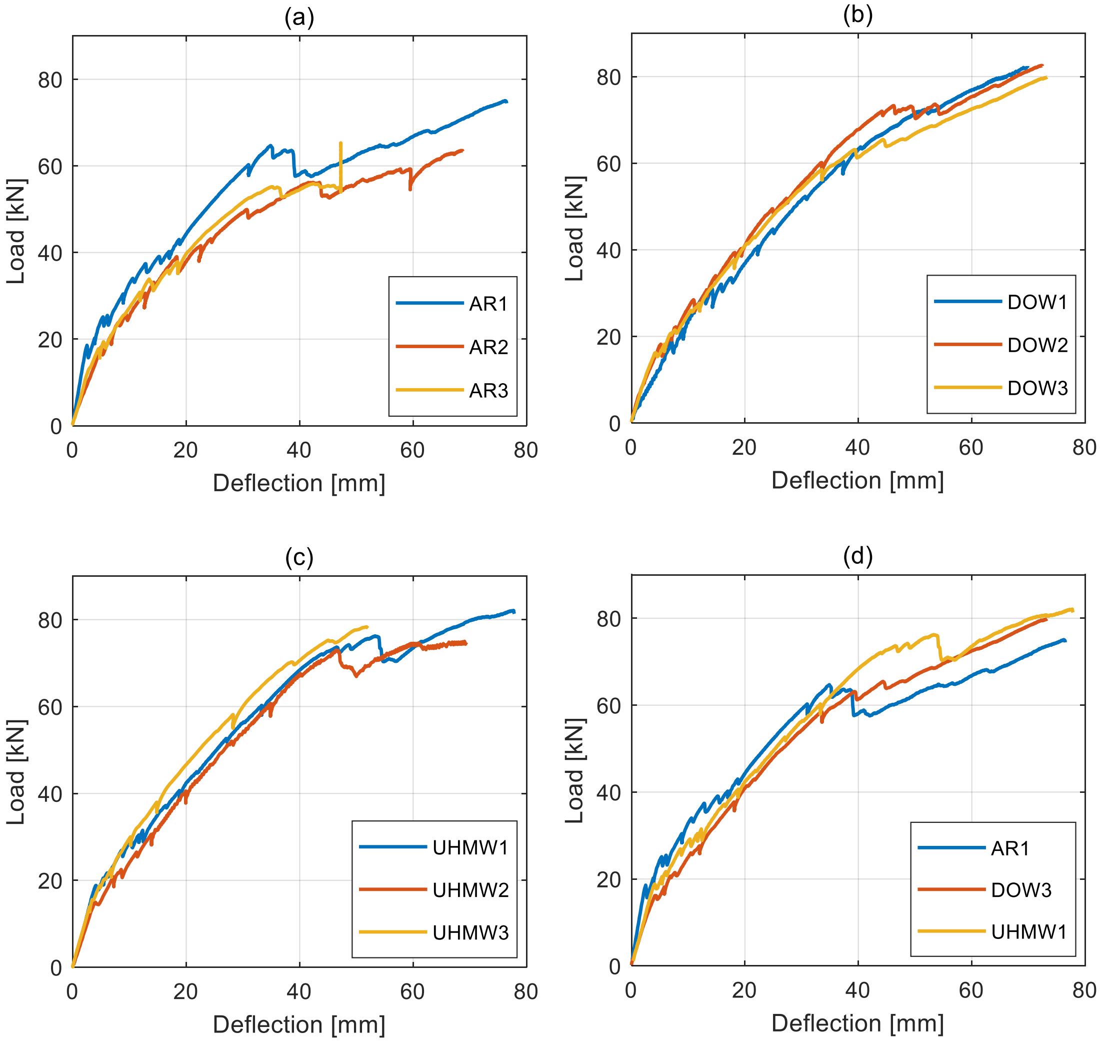

Figure 22 Deflection at the cantilever side of the slabs: (a) AR slabs, (b) DOW slabs, (c) UHMW slabs and (d) comparison of maximum deflections from each group of slabs

Figure 22 (c) shows the load-deflection curves for UHMW slabs. The first drop in the curve indicates cracking of the slabs which occurred at 18.8 kN, 15 kN and 14 kN for UHMW1, UHMW2 and UHMW3 slabs, respectively. The failure loads were 82, 75, and 78 kN for UHMW1, UHMW2 and UHMW3 slabs respectively.

In all three plots shown in Figures 22 (a), (b) and (c) the load-deflection curve is not linear, contrary to what would be expected for a GFRP reinforced slab. The nonlinearity of the curve is due to the thermal break that was inserted at the location of maximum moment in the slabs. The thermal break was compressed throughout the loading process and yielded the nonlinear load-deflection relationships. In Phase I of this research project, GFRP specimens were tested with and without Armatherm^{TM} 500 thermal breaks: The deflection in both specimens was similar up to a load of about 35 kN. At loads higher than 35 kN, the deflection of the specimen with a thermal break increased more rapidly. Just prior to failure, the total deflection in the specimen containing the thermal break was 23% more than the deflection in the specimen with no thermal break (Boila, 2018).

As per CSA S806 (2017), the maximum allowable deflection at service load for a typical balcony floor slab with a clear span length of 1.83 m is 5.1 mm, which is found by dividing the clear span length by 360. From Figures 22 (a), (c), and (b) at a load of 19.7 kN the largest deflection for AR specimens is 3.7 mm, the largest deflection in UHMW specimens is 5.1 mm, and the largest deflection in DOW specimens is 6.5. Thus, the deflection response for AR and UHMW specimens is within the acceptable limit.

The maximum load-deflection curve from each group was plotted in Figure 22 (d). This provides a direct comparison of the maximum deflection among the three groups of slabs. The results show that the specimen with the UHMW thermal break has the largest deflection of 78 mm, while the specimen with DOW thermal break has the smallest deflection of 73 mm. The deflection for AR1 is 76.5 mm. All three slabs cracked at similar loads, and the apparent stiffness of the slabs was comparable, with AR slabs performing marginally better until the load of around 60 kN.

Table 16 Depth of neutral axis for Armatherm^{TM} 500 specimens

Specimen	Average cracking load [kN]	ST-BB-T [με]	SB-AA-C [με]	Neutral axis 'c' [mm]	Average neutral axis 'c' [mm]
AR1	18	1421	-20.66	50	46
AR2		1340	+21.35	47	
AR3		844	+72.67	40	

Using experimental strain profiles, the average depth of neutral axis at cracking load of 18 kN was estimated to be 46 mm for Armatherm^{TM} 500 specimens, as shown in Table 16. Since all three groups of specimens (AR, DOW, and UHMW) had the same reinforcement, only the data from Armatherm group is presented.

4.4 Crack Widths and Interface Dilation Measurements

The dilation between thermal break and concrete was measured for each specimen. For each slab crack widths on the west of the slab on the two sides of thermal break, shown as points A and B in Figure 23, were measured. Figure 23 is a general outline of where dilation between concrete and thermal break as well as crack widths were measured in all specimens. Measurements of dilation between concrete and the thermal break as well as the crack widths were done to compare the performance of the three thermal breaks.

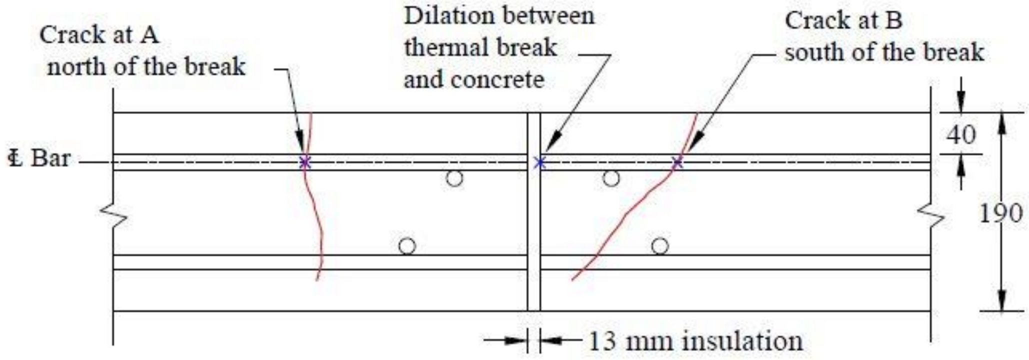

Figure 23 Dilation and crack widths measured at points A and B on west side of each slab

Crack width measurements on the two sides of the thermal break for all nine specimens are shown in Tables 17, 18, and 19. The crack width and dilation at the location of the thermal break was measured using an optical microscope.

DOW specimens showed dilation with concrete on both sides (at both A and B ends), while Armatherm^{TM} 500 and UHMW showed dilation only on one side (on the south of thermal break only, at B end).

Table 17 Measured crack widths and dilation for AR1, AR2 & AR3 specimens

Load [kN]	Specimens	Crack Width at ‘A’ [mm]	Crack Width at ‘B’ [mm]	Dilation on the Interface at ‘B’ End [mm]
20	AR_1	0.1	_	0.15
	AR_2	0.08	_	0.08
	AR_3	0.175	0.09	0.125
	Average	0.12	_	0.12
30	AR_1	0.2	0.075	0.275
	AR_2	0.15	0.05	0.09
	AR_3	_	_	0.2
	Average	0.18	0.06	0.19
40	AR_1	0.3	0.2	0.325
	AR_2	0.175	0.09	0.125
	AR_3	0.3	0.275	0.375
	Average	0.26	0.19	0.28
60	AR_1	0.425	0.3	0.65
	AR_2	0.35	0.3	0.4
	AR_3	0.5	0.5	0.4
	Average	0.43	0.37	0.48

To calculate the total dilation for each group of specimens, average dilation at A was added to average dilation at B. At a load of 20 kN, DOW specimens have a dilation of 0.12 at point A and a dilation of 0.075 at point B. So, at this load the average total dilation for DOW specimens is 0.20, while at the same load Armatherm^{TM} 500 specimens only have an average dilation of 0.12 at B and zero dilation at A. UHMW specimens’ average dilation is also only at B, and it is 0.14. Therefore, DOW specimens show the largest dilations at 20 kN.

As discussed in section 4.2, dilation at a service load of 19.7 kN was calculated for all three thermal break groups using PI gauge data as well. For slabs AR, DOW and UHMW dilation between the thermal break and concrete started at 19 kN, 18 kN and 17 kN respectively.

For all specimen groups dilation between the thermal break and concrete occurred at around 20 kN, and increased with load. AR slabs had the smallest dilation at the interface with concrete, while DOW slabs showed the largest dilation, on average.

For use in structural applications, the load at which the first sign of interface dilation appears will need to be increased. Otherwise, water may start to seep into the structure and cause serviceability problems. The surface of the thermal breaks had no treatment to increase bond with concrete. Means to increase the load at which the dilation on the interface occurs will need to be investigated in future research.

Table 18 Measured crack widths and dilation for DOW1, DOW2 & DOW3 specimens

Load [kN]	Specimens	Crack Width at ‘A’ [mm]	Crack Width at ‘B’ [mm]	Dilation on the Interfaces [mm]	
				at ‘A’ End	at ‘B’ End
20	DOW$_1$	0.1	_	0.05	0.075
	DOW$_2$	0.1	_	0.15	_
	DOW$_3$	0.15	_	0.15	_
	Average	0.12	_	0.12	_
30	DOW$_1$	0.1	_	0.075	0.15
	DOW$_2$	0.15	0.1	0.25	_
	DOW$_3$	0.2	0.08	0.175	_
	Average	0.15	0.09	0.17	_
40	DOW$_1$	0.2	0.125	0.1	0.2
	DOW$_2$	0.2	0.2	0.3	_
	DOW$_3$	0.25	0.15	0.125	0.1
	Average	0.22	0.16	0.17	0.15
60	DOW$_1$	0.3	0.2	0.2	0.25
	DOW$_2$	0.2	0.5	0.3	_
	DOW$_3$	0.3	0.1	0.25	0.175
	Average	0.27	0.27	0.25	0.21

Table 19 Measured crack widths and dilation for UHMW1, UHMW2 & UHMW3 specimens

Load [kN]	Specimens	Crack Width at ‘A’ [mm]	Crack Width at ‘B’ [mm]	Dilation on the Interface at ‘B’ End [mm]
20	UHMW$_1$	0.1	_	0.15
	UHMW$_2$	0.075	_	0.1
	UHMW$_3$	0.175	0.1	0.175
	Average	0.12	_	0.14
30	UHMW$_1$	0.1	0.1	0.2
	UHMW$_2$	0.125	0.1	0.25
	UHMW$_3$	0.38	0.15	0.225
	Average	0.21	0.12	0.23
40	UHMW$_1$	0.1	0.2	0.25
	UHMW$_2$	0.2	0.1	0.3
	UHMW$_3$	0.4	0.315	0.25
	Average	0.23	0.21	0.27
60	UHMW$_1$	0.1	0.35	0.3
	UHMW$_2$	0.3	0.17	0.7
	UHMW$_3$	0.6	0.7	0.5
	Average	0.33	0.41	0.5

4.5 Failure Mode

Figure 24 shows that the mode of failure for AR3 was shear failure. The thickness of the slab would have to be increased, or shear reinforcement would have to be included to prevent this type of failure. Neither of the two options was feasible for this project, due to limitations on testing of the slabs. The larger thickness would have made the slabs too heavy for handling at Red River College, and additional reinforcement would have made the thermal testing not representative of typical balcony slab reinforcement. It is understood that with proper detailing of slab thickness, the shear failure could be avoided in practice.

The first cracks that started to form close to the middle support near the thermal break were flexural cracks, on the cantilever side. The cracks later continued in a soft slope at 11 degrees on the west side and 21 degrees on the east. They started at the top in the tension zone and moved to the bottom/compression zone of the slab, as the depth of neutral axis decreased. Vertical cracks formed at lower loads and as the load increased, diagonal shear cracks started to appear as well. As shown in Figure 25, a visible crack opened at the bottom of AR3 slab between the thermal break and concrete at a load of 30 kN. This dilation took place on the cantilever side of the specimen.

(a) west side (b) east side

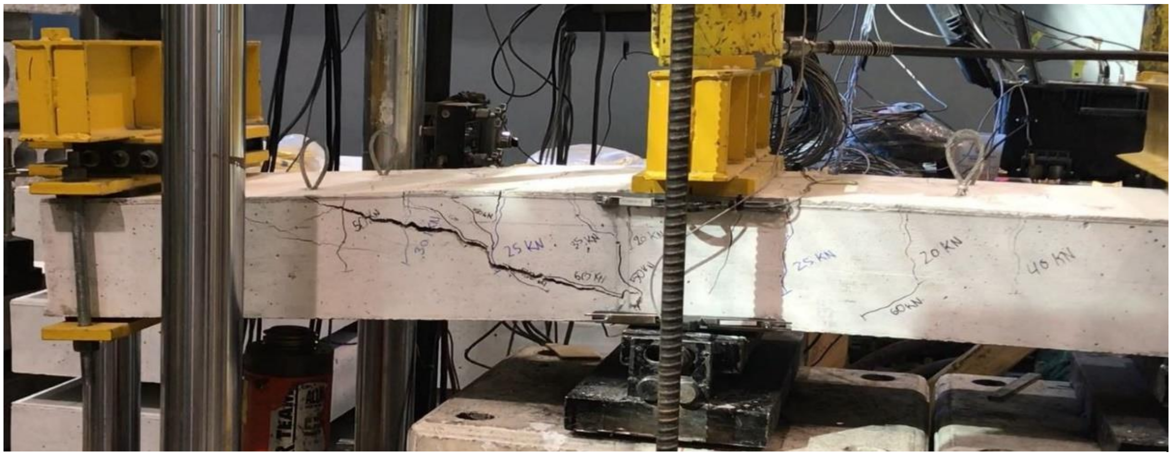

(c) east side

Figure 24 West and east sides of the cantilever end of AR3

Figure 25 Crack under the slab close to support at the cantilever end of AR3

Figure 26 shows the west side of AR3, UHMW3, and DOW3 (from top to bottom) after failure, while Figure 27 shows the east side of the same slabs. These three slabs were tested structurally only.

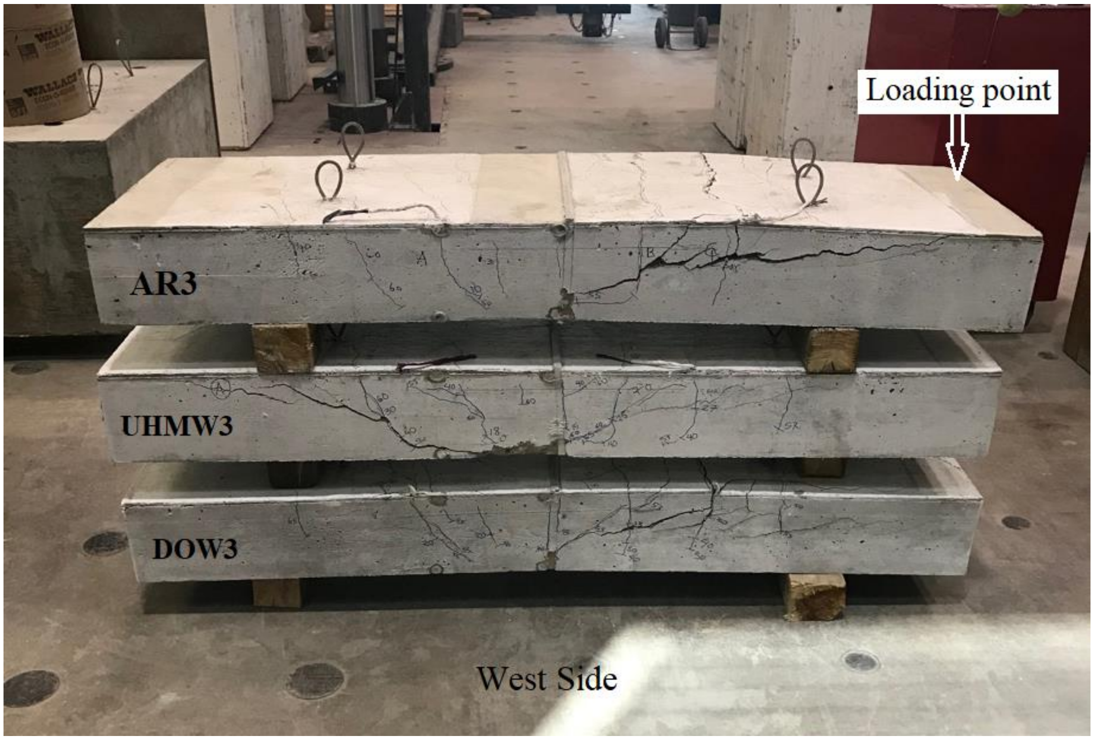

Figure 26 West side: AR3, UHMW3 and DOW3

Figure 27 East side: AR3, UHMW3 and DOW3

The AR3 and DOW3 slabs failed at the cantilever side. UHMW3 failed at the inside/north side of the slab between the two supports. Supports A and B provided insufficient pressure for all three slabs, and so the slab supports did not provide sufficient fixity. These caused small cracks everywhere on two sides of the middle support for all three specimens. The pressure at the supports was not increased for the remaining tests, so that the results from all specimens could be compared.

Shear failure occurred for AR3 and DOW3 slabs at the cantilever end. There are some noticeable differences in the slope of the shear cracks in AR3 and DOW3. In AR3 the concrete shear crack has a flat slope and is longer. In DOW3 the crack starts at lower loads and its slop increases rapidly.

Figures 28 and 29 show the west and east sides of AR1, AR2, UHMW1, UHMW2, DOW1, and DOW2 after failure.

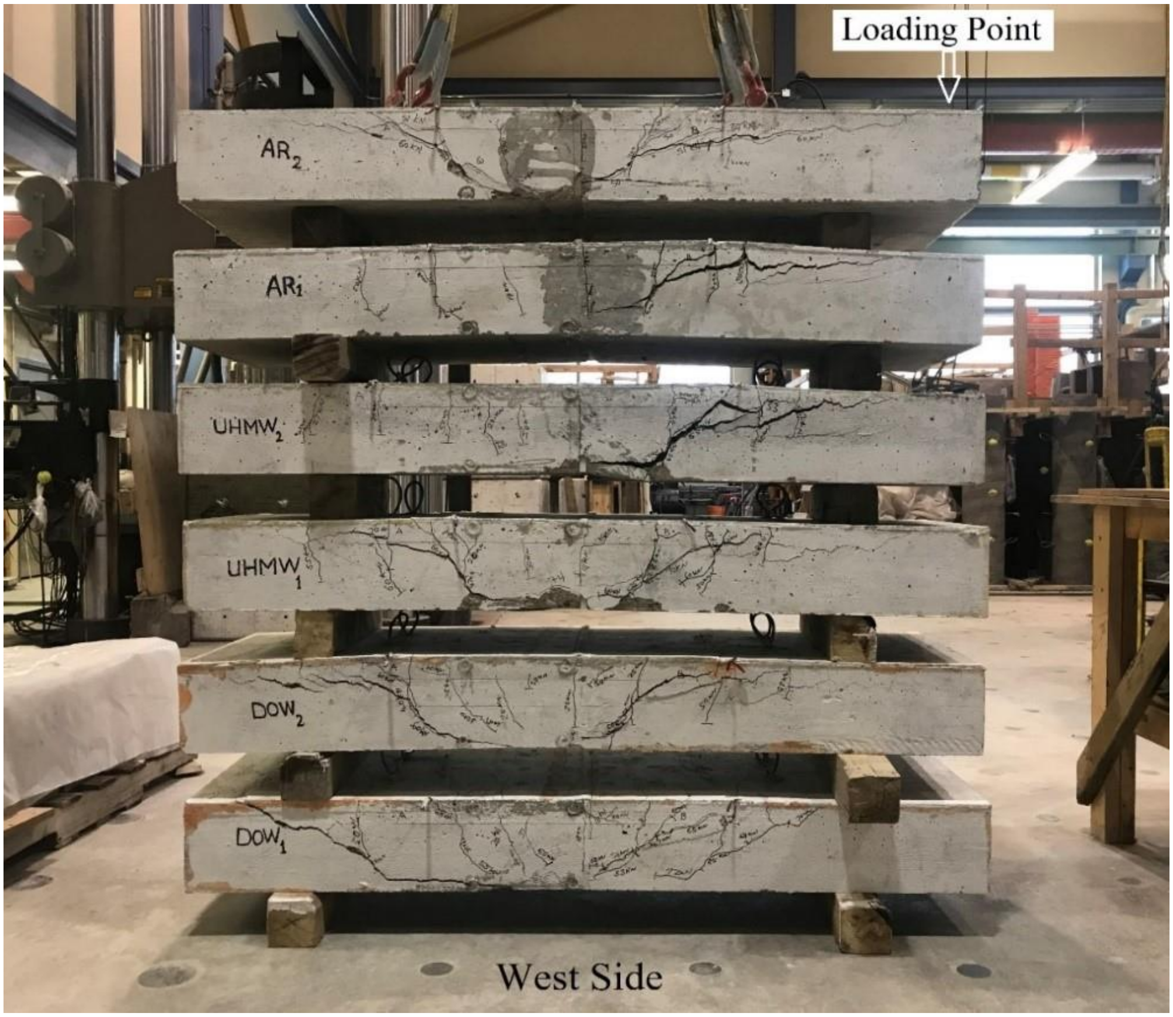

Figure 28 West side: AR1, AR2, UHMW1, UHMW2, DOW1 and DOW2

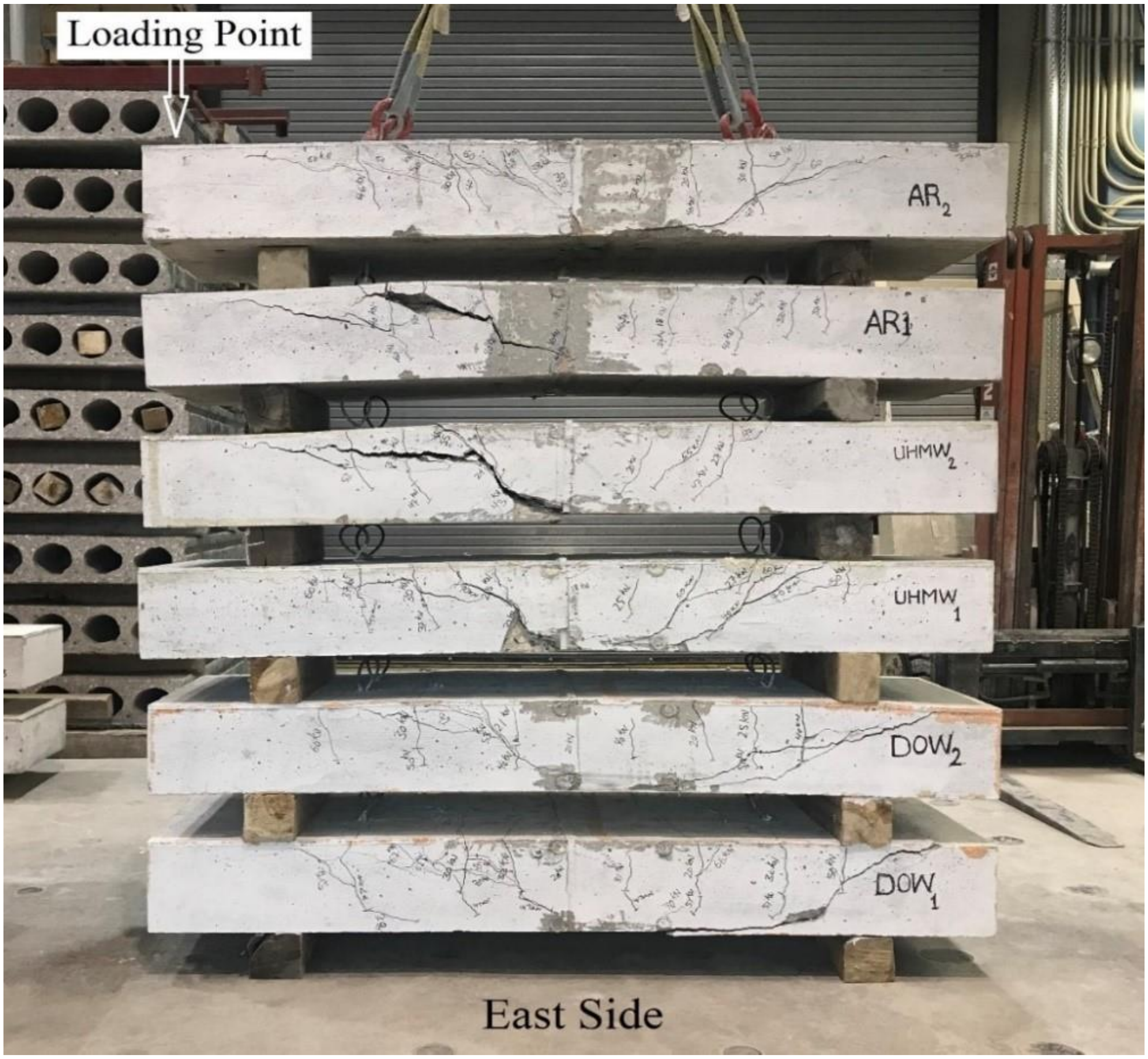

Figure 29 East side: AR1, AR2, UHMW1, UHMW2, DOW1 and DOW2

The angles of shear failure on both west and east sides for all 9 slabs were measured and are shown in Table 20. Overall, these angles show that the shear cracks followed the load path.

As seen in Table 20, the specimens with UHMW thermal break show larger angles than the specimens with AR and DOW breaks. Specimens with Armatherm^{TM} 500 had the smallest angles. However, it must be noted that the specimens with DOW breaks had a higher failure load.

Table 20 Shear crack angles on west and east sides of slabs

Shear Crack Angle [Degrees °]				
Specimens	West Side		East Side	
	Balcony Side	Floor Side	Balcony Side	Floor Side
AR1	21	-	21	-
AR2	16	30	25	18
AR3	11	-	21	-
Average	16	30	22	18
DOW1	25	19	24	19
DOW2	30	22	19	17
DOW3	18	-	28	-
Average	24	20	24	18
UHMW1	22	24	38	28
UHMW2	18	-	19	-
UHMW3	-	21	-	16
Average	20	22	28	22

4.6 Summary of Results from Structural Testing

This section includes a comparison of results in terms of crack widths, failure load, deflection, and thermal break compressibility.

To get the crack widths, the maximum elongation read from PI-G1 was divided by the number of cracks along the length of PI-G1. Table 21 shows a summary of crack widths for the three group of slabs. The AR slabs show an average crack width of 1.2 mm which is larger than that for the other two groups of slabs with DOW and UHMW which show an average crack width of 0.6 mm.

Table 22 contains the load at which the first cracks happened, failure load, and maximum deflection for each group of slabs. Mode of failure for all nine specimens was shear failure.

From Table 22 the average failure loads for AR, DOW, and UHMW slabs are 67.8 kN, 81.5 kN, and 78 kN respectively. The results show that the slabs with DOW thermal break have the largest average failure load compared with the specimens with AR and UHMW breaks.

The average deflections for AR, DOW, and UHMW slabs were 64 mm, 72 mm, and 66 mm respectively. The group of slabs with DOW thermal break shows the largest average deflection of 72 mm, and AR the smallest at 64 mm.

Table 21 Crack width of slabs

Slab	Crack Width [mm]	Average [mm]
AR1	1.17	1.2
AR2	1.26	
AR3	0.14	
DOW1	0.65	0.6
DOW2	0.47	
DOW3	0.19	
UHMW1	0.54	0.6
UHMW2	0.61	
UHMW3	0.51	

Table 22 Experimental values of load at first crack and at failure

Specimens	First Crack [kN]	Failure Load [kN]	Max Deflection [mm]
AR_1	18.5	75	76
AR_2	18.3	63.5	69
AR_3	17.8	65	47
Average AR		67.8	64
DOW_1	19	82	70
DOW_2	18.2	82.5	72
DOW_3	16	80	73
Average DOW		81.5	72
$UHMW_1$	18.8	82	78
$UHMW_2$	15	75	69
$UHMW_3$	14	78	52
Average UHMW		78	66

Figure 30 shows that elongation was linear up to loads of about 15 kN, 26 kN, and 34 kN for UHMW2, DOW3, and AR1, respectively. Beyond these loads a rapid deformation can be seen in all specimens. Similar behaviour was observed in the contraction plots. The specimens behaved linearly up to a load of about 34 kN. A more rapid deformation started from a load of 58 kN until failure. The largest elongation, 0.0155, occurred at a load of about 75 kN. The largest contraction, -0.0166, happened at a load of about 65 kN. The deformations indicate that the thermal break could carry some compressive load up to 56 kN. Figure 30 (a) shows that in the tension zone the dilation at UHMW thermal break started at a lower load compared to other two thermal breaks. On the other hand, in compression zone the three thermal breaks were compressed at the same load of around 55 kN, meaning that their compressive strength is similar, as seen in Figure 30 (b).

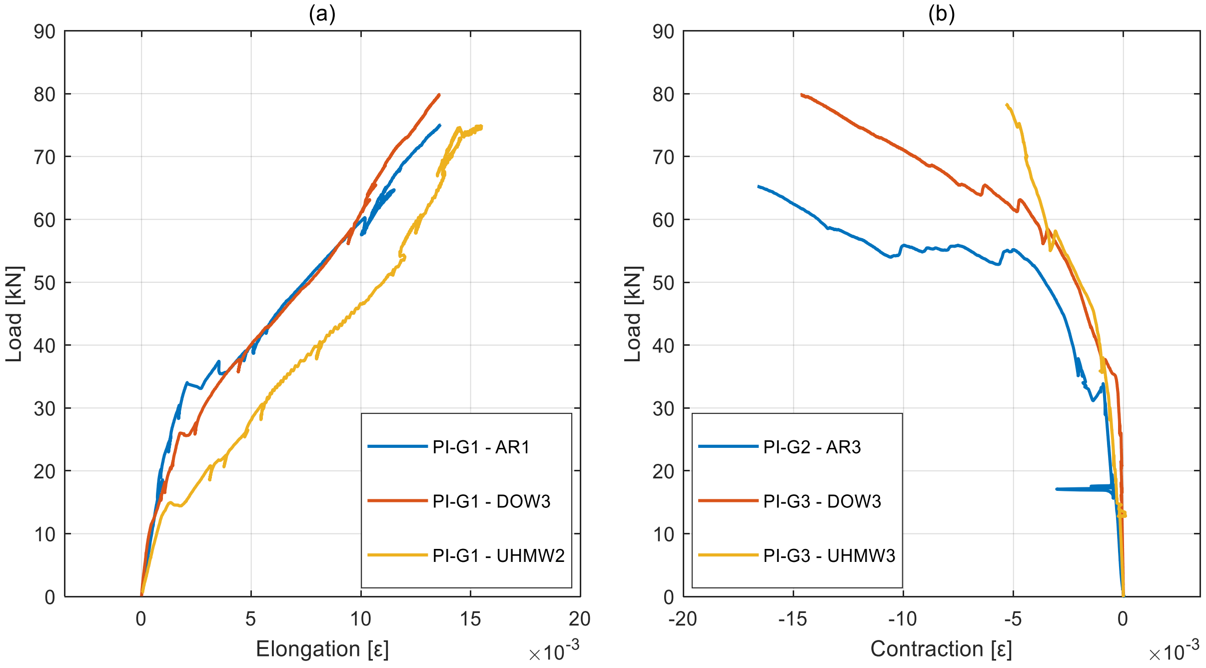

Figure 30 PI gauges on concrete slabs at the thermal break location: (a) largest elongation and (b) largest contraction

4.7 Structural Comparison with Previous Work

One main purpose of this study was to compare test results with results from Phase I of this study (Boila, 2018). The key comparison benchmarks were dilation between thermal break and concrete, as well as slab deflection. Only Armatherm specimens from this work are compared with GFRP reinforced Armatherm specimens from Phase I. Figure 31 below compares the deflection results, and clearly shows that at loads close to the service load, specimens in this study underwent smaller deflection. A thinner thermal break means a smaller gap in concrete between the floor slab and the cantilever slab which means the structure is stronger. Moreover, the GFRP reinforcement scheme used in this study leads to a smaller deflection. For percentage comparison of deflections in the two study, see Table 23 below.

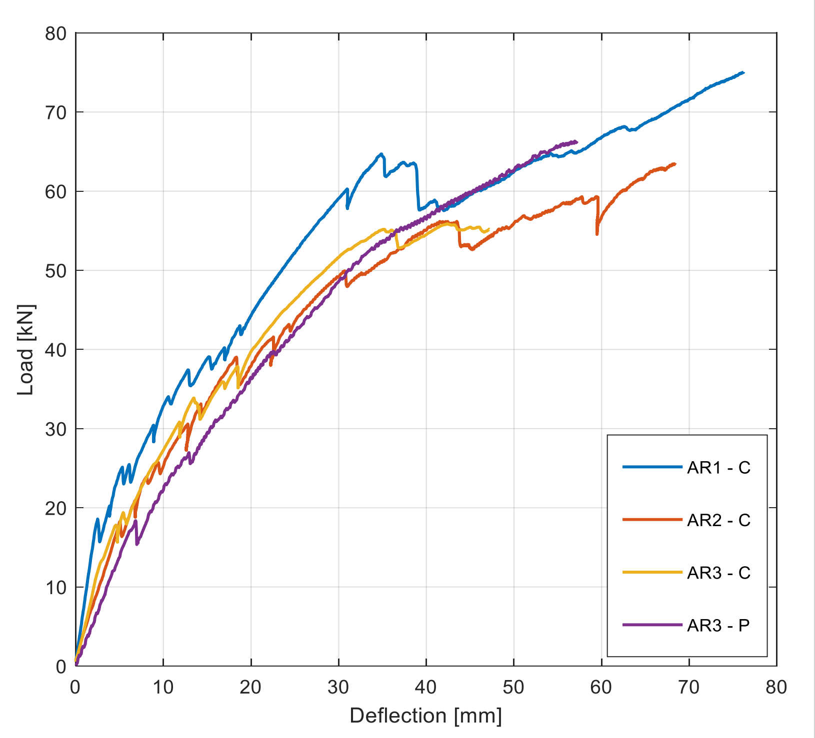

Figure 31 Comparison of maximum deflection between Phase I (Boila, 2018) and Phase II

Table 23 Deflection comparison at 19.7 kN

Sample	Deflection [mm]	
	Phase I	Phase II
AR1	8.8	3.7
AR2	8.7	6.3
AR3	8.8	6.4
Average	8.7	5.4

The above reasons also led to a smaller dilation between thermal break and concrete in this study, compared to the previous study. The dilation between concrete and Armatherm thermal break in the three Armatherm specimens of this study was 47%, 70% and 25% smaller than the dilation recorded between Armatherm and concrete in the previous study.

Chapter 5 Thermal Experimental Program

In this chapter preparations for thermal tests of six balcony slabs are detailed, along with an analysis of the thermal experimental results.

5.1 Materials

Six specimens were tested for their thermal performance prior to structural testing. The specimens were divided into three pairs: Each pair had the same type of 13 mm thermal break. The key difference between these thermal breaks is their thermal conductivity, which is 0.0562 W/mK for Armatherm^{TM} 500 (Armadillo, 2019), 0.2306 W/mK for DOW (Jasper Plastics, 2020), and 0.4093 W/mK for UHMW (Technical Products Inc., 2018).

5.2 Instrumentation for Thermal Tests

A total of 48 thermistors were installed in each slab. Each thermistor had a resistance of 10 kΩ. Thermistors were embedded in four layers (top, on-rebar, middle, bottom). The thermal break itself was placed midway along each slab, perpendicular to longitudinal rebars. The thermistors in the first layer, i.e., the top surface thermistors, were divided into four rows of three. Two rows (six thermistors) were on the cold side (the cantilever side) of the thermal break and the other two rows (six thermistors) on the hot side of the thermal break. The thermistors in the second layer were installed on rebars, which included three thermistors on each side (i.e., on cold and hot sides), and in contact with the thermal break. There was a total of six on-rebar thermistors per slab. The thermistors in the third layer, middle thermistors, were placed in the central vertical plane of the balcony slab below the thermistors on the rebar. There were three rows of middle thermistors on each side of the thermal break. So, the total number of middle thermistors per slab was eighteen. The thermistors in the first row of middle thermistors were in contact with the thermal break. The second row was about 35 mm away from the thermal break and the farthest row was at a distance of about 130 mm away from the thermal break. See Figure 32 for top surface, on-rebar, and middle thermistors.

The thermistors in the fourth layer, bottom surface thermistors, were attached to the bottom surface of the slab. Similar to the top surface thermistors, there were two rows of thermistors on each side of the thermal break. The total number of the bottom surface thermistors was twelve per slab.

Figure 32 Top surface, on rebar, and middle thermistors

In all, a total of 48 thermistors were used in each balcony slab. To label the thermistors in drawings and plots, the following convention was used: cold/hot side – distance from thermal break – layer which thermistor belongs to – section – type of thermal break & slab number. For example, C130-T-A-AR1 means the thermistor is on the cold side, at a distance of 130 mm from thermal break; ‘T’ means it is in the top layer; ‘A’ means section AA, and AR1 means the slab was the first slab with an Armatherm™ 500 thermal break. Each thermistor was at one of the following three distances from the origin/thermal break: 0 (the ones in contact with thermal break), 35 mm, and 130 mm. Thermistor distances from thermal break and other details are shown in Figure 33.

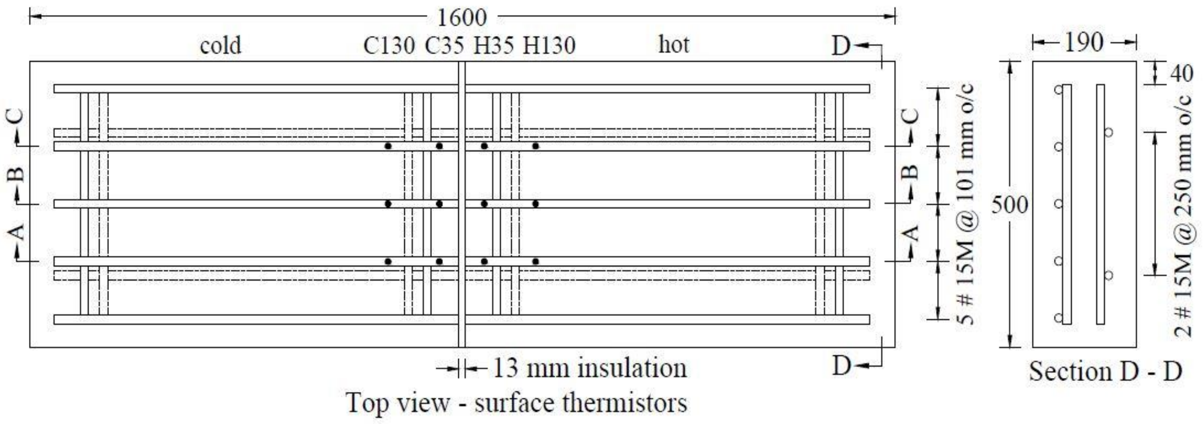

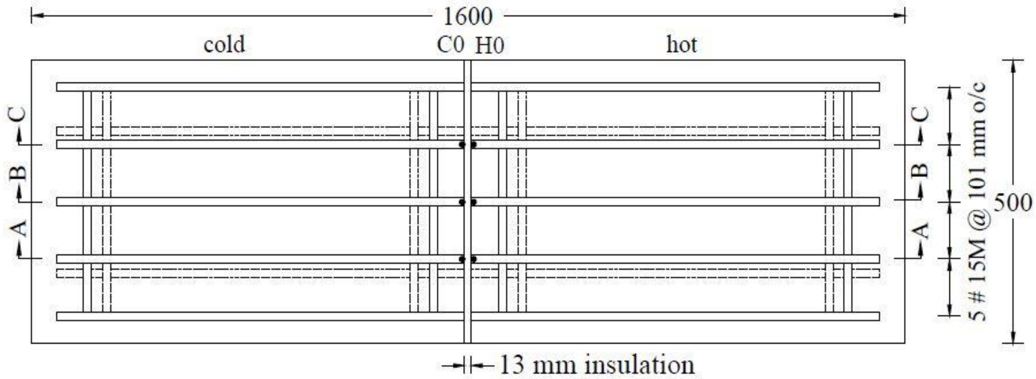

Top view - on rebar thermistors

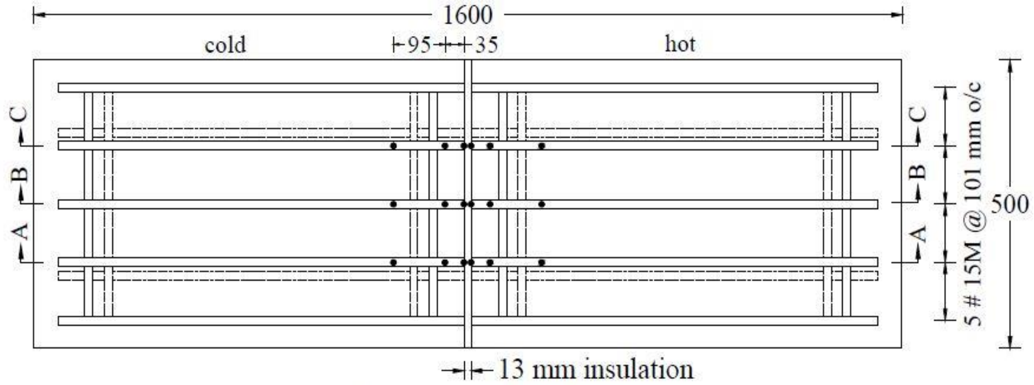

Top view - middle thermistors

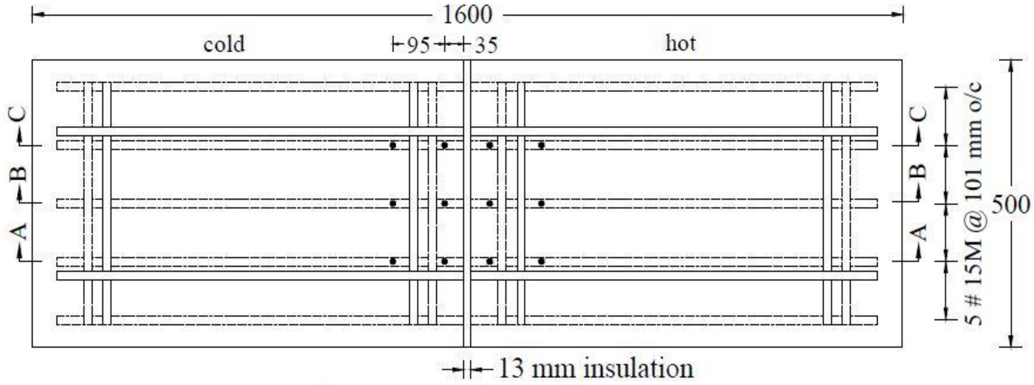

Bottom view - bottom thermistors

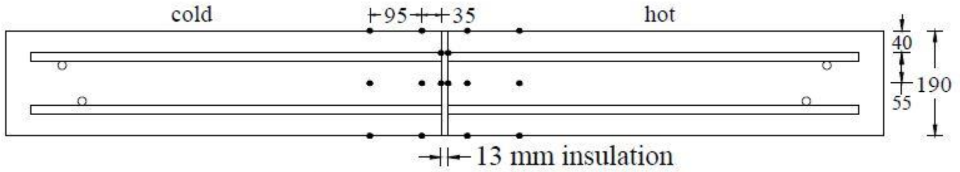

Sections A-A, B-B & C-C thermistors

Figure 33 Thermistor distances from thermal breaks for all four layers

The goal of the thermal tests was to compare the thermal performance of the three different thermal breaks used in this study: Armatherm™ 500, DOW and UHMW. A total of six specimens (three pairs) were tested thermally. Each pair of specimens was insulated with one type of thermal break. Each pair was tested in one run of the test. Specimens were tested under two different temperatures (steady states). See Table 24 for a summary.

Table 24 Different temperatures at which specimens were tested

Specimen	Steady State I (Chamber temperature cold/hot)	Steady State II (Chamber temperature cold/hot)
AR1 & AR2	-30°C /+21°C	—
UHMW1 & UHMW2	-30°C /+21°C	-40°C /+28°C
DOW1 & DOW2	-30°C /+21°C	-40°C /+35°C

At first, all six specimens (AR1 & AR2, UHMW1 & UHMW2, and DOW1 & DOW2) were tested under the first steady state, at the temperature -30°C/+21°C for the cold and hot sides, respectively. The two UHMW and two DOW specimens were additionally tested under a second steady state where the chamber temperature was set to -40°C /+28°C for UHMW1 & 2, and to -40°C/+35°C for DOW1& 2.

5.3 Thermal Test Setup

Thermal tests were carried out on six of the balcony slabs, prior to structural testing, in the Red River College Centre for Applied Research in Sustainable Infrastructure (CARSI) Lab thermal chamber facility. The aim was to measure the temperature distribution across the slabs. The thermal chamber had two compartments separated by an insulated wall, each kept at a different temperature to represent indoor and winter outdoor temperatures. The balcony slabs were set in the wall separating the chambers as shown in Figure 34. The chambers were separated by a 4″ (101.6 mm) Styrofoam wall to reduce heat transfer between the hot and cold compartments.

The thermal chamber was big enough to contain two slabs at a time. Therefore, in every test run two slabs were tested: Two slabs were placed next to each other in the chamber, separated by a 6″ (152.4 mm) layer of insulating Styrofoam to reduce heat transfer between slabs. As shown in Figure 34, Ultra Seal PF-100 Gun Foam was used to seal the gaps between the 4″ thick Styrofoam wall and the outer walls of the thermal chamber, as well as between it and the surface, sides and bottom of the slabs.

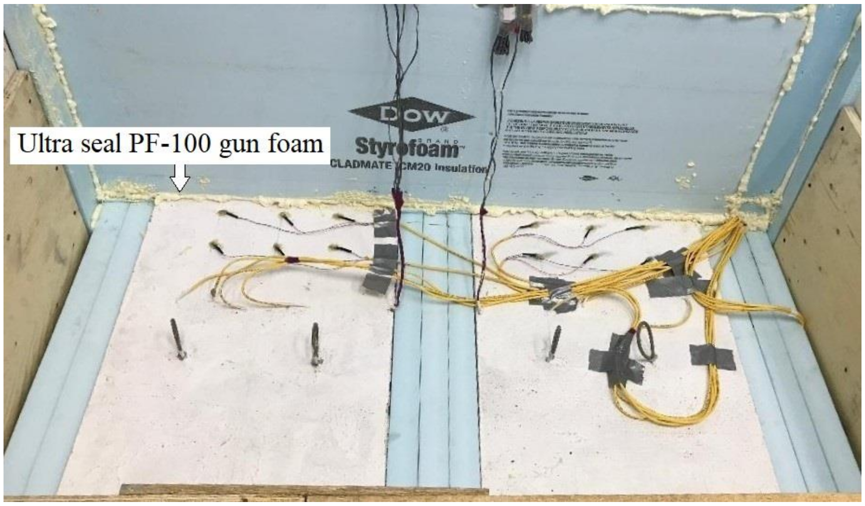

Figure 34 Styrofoam (blue) and gun foam (white) used to thermally separate the cold and hot sides

Each slab was put in the chamber such that the cantilever end was in the cold area. The thermal break is much thinner (0.5 inches) than the insulating Styrofoam wall (4 inches), and it was positioned underneath the edge of Styrofoam wall on the cold side to localize the greatest temperature adjacent to the cold side. See Figure 35 for more clarification.

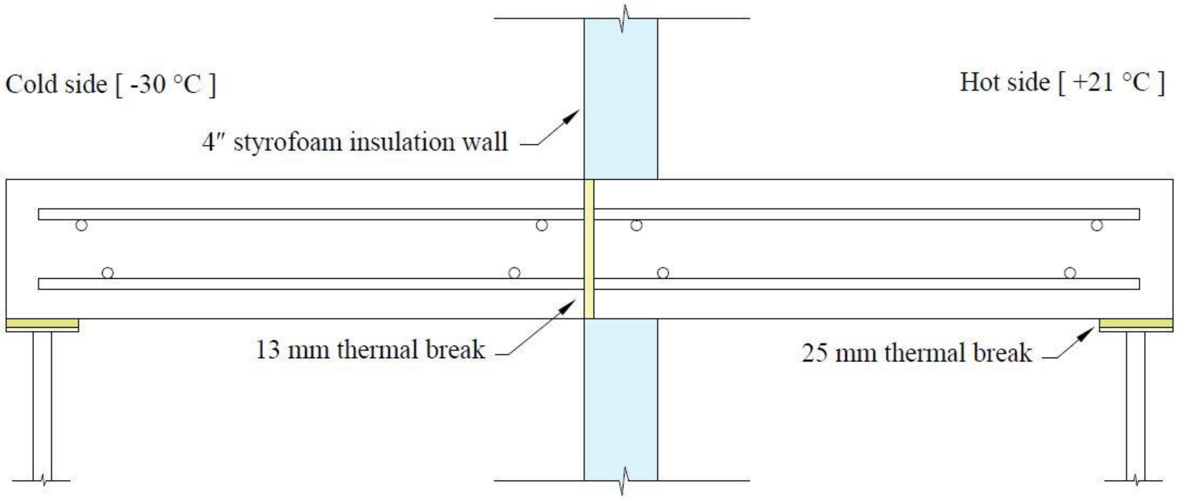

Figure 35 Position of thermal break

Two 50 x 50 mm steel supports were placed under each end of the slab. There were steel plates on top and bottom of supports to hold them in place. Thermal breaks (of dimensions 100 x 100 x 25 mm) were placed between the support and balcony to reduce heat transfer through the steel support. They are shown in yellow in the Figure 35.

The cold and hot compartments of the thermal chamber were each equipped with a fan. The fan on the cold side blew cold air into the compartment and was controlled to maintain the temperature at a fixed and uniform cold temperature. Similarly, the fan on the hot side blew hot air into the compartment and was controlled to maintain the temperature at a fixed and uniform hot temperature. To reduce difficult-to-measure forced convection effects due to the fans, plywood boxes were built around the slabs on both the cold and hot sides. The plywood used for making boxes had a thickness of 12 cm, a height of 100 cm, and width of 150 cm and covered the exposed slabs entirely. The plywood box is shown in Figure 36.

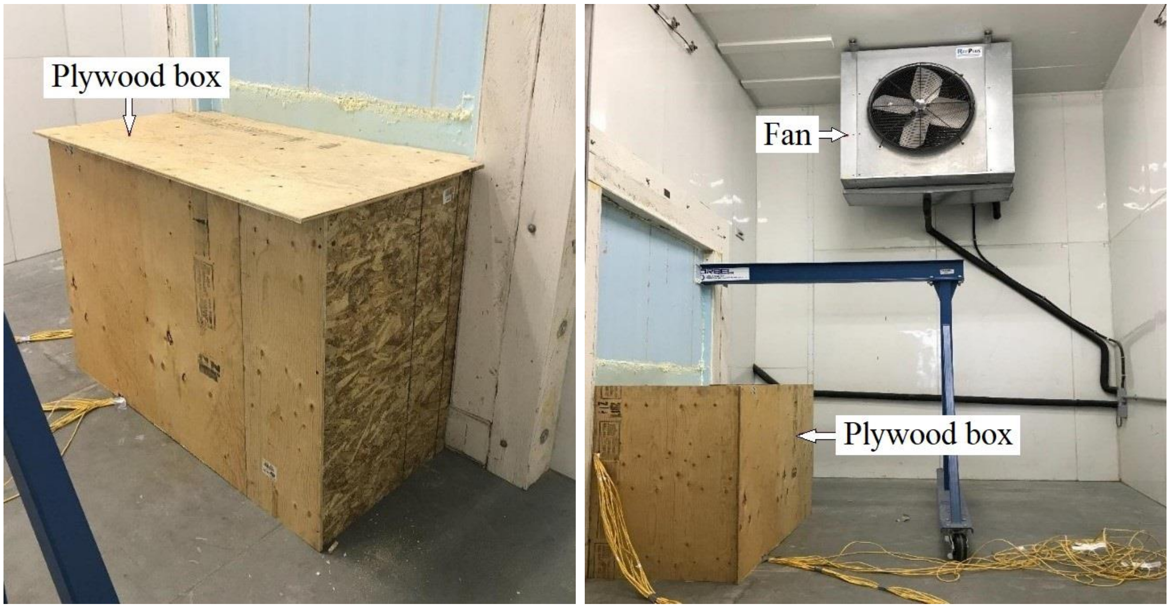

Figure 36 Plywood boxes to ensure uniform heat/cold distribution

The next chapter provides details of the thermal test results as well as interpretations for these results.

Chapter 6 Thermal Results and Analysis

This section includes the temperature results derived from the thermistors that were installed on the surfaces and inside the slabs. The six slabs listed in Table 25 were thermally tested at Red River College's Center for Applied Research in Sustainable Infrastructure (CARSI) Lab and then structurally tested. In this chapter the experimental thermal results for these six specimens are discussed.

The cantilevered end of the slab is exposed to the cold chamber and is called the 'cold side'. The floor end of the slab is exposed to the hot chamber and called the 'hot side'. Specimens were identified based on the type of the thermal break used in the slab. Three types of thermal break were used in this study. Table 25 lists how specimens were labelled.

Table 25 Naming of specimens

Specimen Name	Type of Thermal Break	# of Slabs Tested Thermally
AR1, AR2	Armatherm^{TM} 500	2
UHMW1, UHMW2	Ultra High Molecular Weight Polyethylene	2
DOW1, DOW2	DOW	2

6.1 Estimation of Steady State Slab Temperatures

Steady state slab temperatures were estimated from transient thermistor data using the same general approach for all thermal testing. Thermistor reading was first converted to temperature data using the Steinhart and Hart equation:

$$T = \frac{1}{A + B\ln(R) + C\,[\ln(R)]^3} \qquad (1)$$

Where T is temperature in degrees Kelvin, R is resistance in Ohms measured by thermistor and A, B and C are coefficients. To find the values of coefficients thermistor resistance was measured at three different temperatures as shown in Table 26 (TE Connectivity, 2020).

Table 26 Temperature values used to determine coefficients in equation (1)

	Temperature °C	Resistance Ω	Temperature °K	Coefficients
Low	-35	242681.16	238.15	A = 1.126 x 10^{-3}
Medium	0	32650	273.15	B = 2.346 x 10^{-4}
High	+35	6531.17	308.15	C = 8.617 x 10^{-8}

A typical transient temperature plot is shown in Figure 37 for the cold side SS1 AR1 case. Initially the temperatures decrease and reach pseudo-steady state temperatures after approximately 1500 minutes. Due to the defrost cycle of the refrigeration cycle used to cool the cold side there are temperature spikes in the data. Average steady state temperatures were estimated based on 560 minutes of data beginning at approximately 2400 minutes. The averaged ranges are highlighted by the ellipses in Figure 37. This general approach was used for all thermal testing.

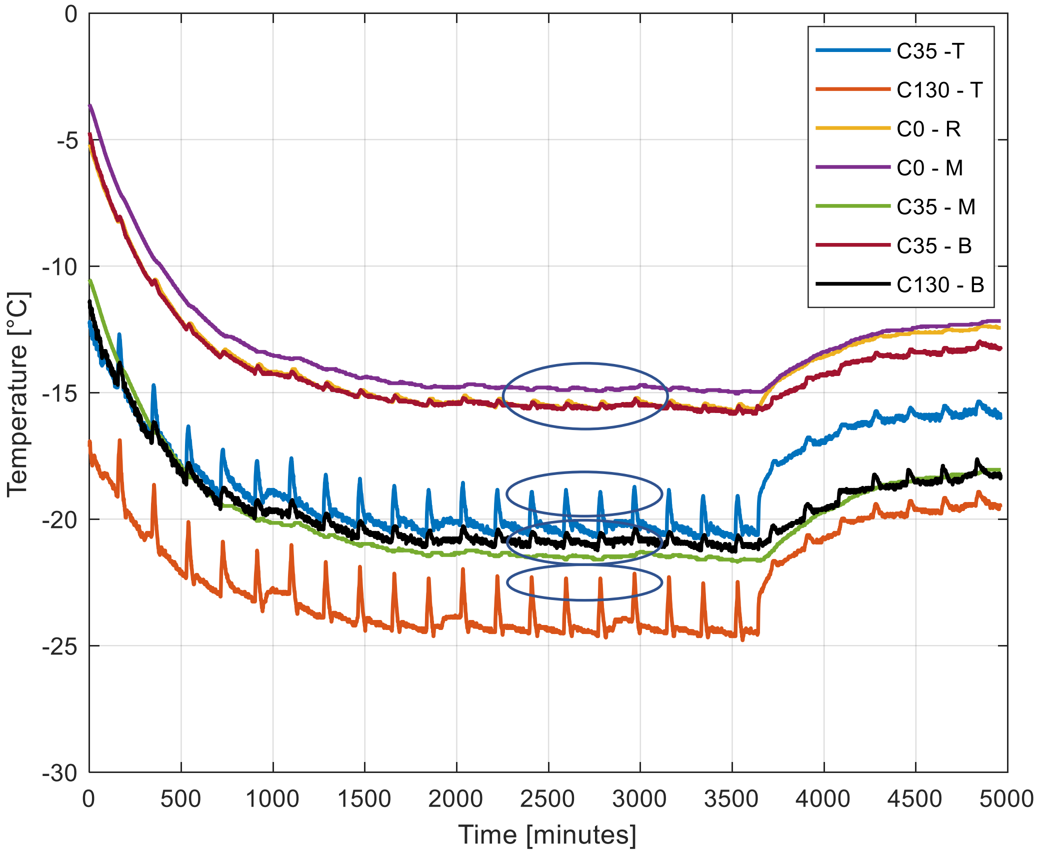

Figure 37 Temperature profile [sec A], cold side, SS1, AR1

Table 27 shows the ranges which were used to calculate the average thermistor temperatures for each specimen. The range was taken peak to peak.

Table 27 Calculation of average thermistor temperature

Specimen	SS1 [minutes]	Range	SS2 [minutes]	Range
AR1	2411 - 2971	561	—	—
AR2	2411 - 2971	561	—	—
DOW1	2026 - 2583	558	3397 - 3953	557
DOW2	2022 - 2586	565	3020 - 3579	560
UHMW1	4303 - 4860	558	8404 - 8967	564
UHMW2	4302 - 4862	561	14063 - 14613	551

6.2 AR1 and AR2

Placement of sections for AR1 and AR2 slabs is shown in Figure 38. Section AA of AR1 was placed next to section AA of AR2. In both AR1 and AR2 slabs 13 mm thick Armatherm^{TM} 500 insulation separated the cold and hot ends.

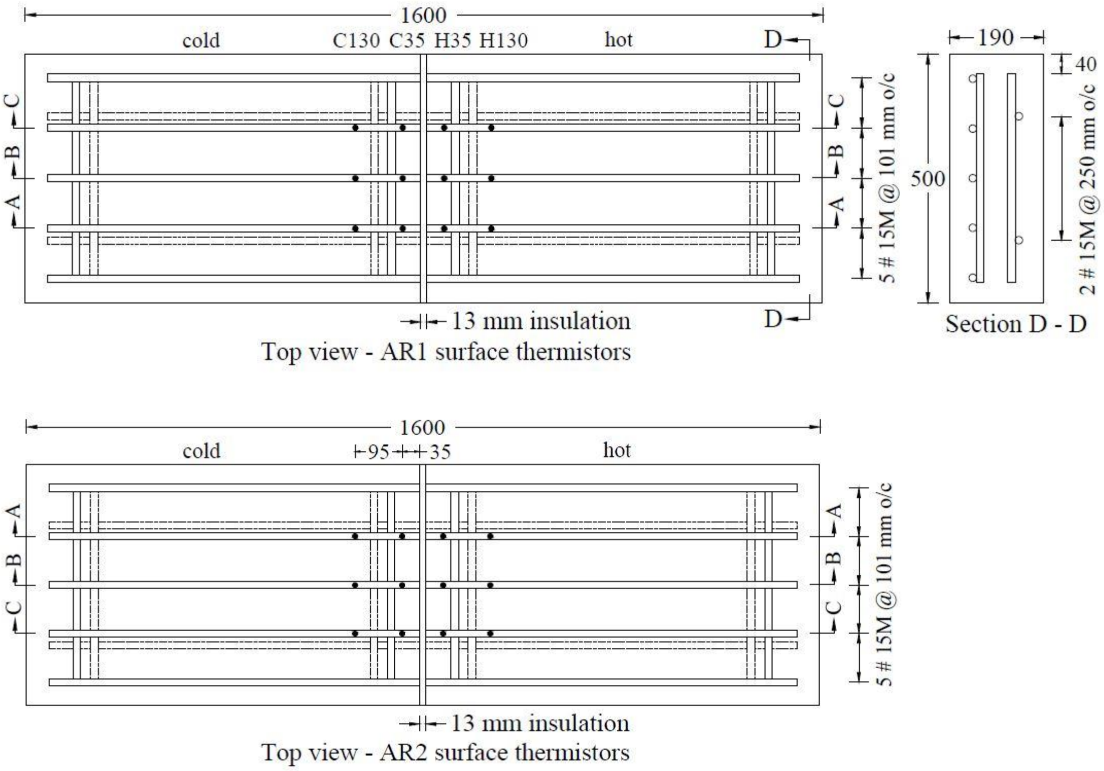

Figure 38 Drawings of AR1 and AR2 specimens inside thermal chamber

AR1 and AR2 were tested only once, with a steady state temperature of -30 °C / +21 °C. Table 28 shows the average temperature recorded by each thermistor in sections A, B, and C on both cold and hot sides of AR1 and AR2. The values recorded by C130-M for section A, and H35-B for section B do not make sense, and have been underlined in the Table 28.

Table 28 SS1 temperatures for AR1 and AR2

Thermistor Name	SS1 Temperatures for AR1			SS1 Temperatures for AR2		
	Section [A]	Section [B]	Section [C]	Section [A]	Section [B]	Section [C]
C35 – T	-20.17	-20.63	-20.78	-22.03	-22.42	-21.92
C130 – T	-24.13	-23.59	-24.15	-26.04	-25.29	-24.64
C0 – R	-15.49	-15.93	-16.21	-17.22	-17.62	-15.22
C0 – M	-14.86	-15.31	-15.16	-16.78	-17.22	-16.93
C35 – M	-21.49	-17.35	-17.30	-18.38	-18.94	-18.74
C130 – M	+16.11	-21.39	-21.31	-22.86	-22.63	-22.48
C35 – B	-15.55	-16.26	-16.62	-23.47	-23.30	-23.67
C130 – B	-20.86	-20.88	-21.14	-18.20	-20.11	-20.41
H35 – T	+6.59	+6.68	+6.78	+5.87	+6.09	+6.50
H130 – T	+14.71	+14.99	+15.47	+14.64	+15.02	+15.84
H0 – R	+3.42	+2.41	+2.19	+1.23	+3.63	+3.60
H0 – M	+5.07	+5.26	+5.17	+3.82	+4.09	+4.22
H35 – M	+7.02	+7.40	+31.23	+5.67	+6.28	+6.30
H130 – M	+12.46	+15.91	+12.19	+11.69	+12.09	+12.41
H35 – B	+6.41	-195.95	+6.01	+4.75	+4.33	+5.69
H130 – B	+14.09	+13.71	+14.30	+14.38	+25.98	+15.17

Figure 39 shows the location and recorded temperature of each thermistor for the first AR1 steady state case. The AR1 temperature distribution in sections A-A, B-B and C-C, accounting for thermistor errors, are nominally the same. The temperatures on the top surface of the cold side are lower than the middle and bottom temperatures suggesting a weak convection effect at the top surface that lowers the temperatures. The temperature difference across the Armatherm^{TM} 500 is lower where the thermistors are attached to the rebar, indicating locally higher heat transfer rates through the Armatherm^{TM} 500 at the rebar.

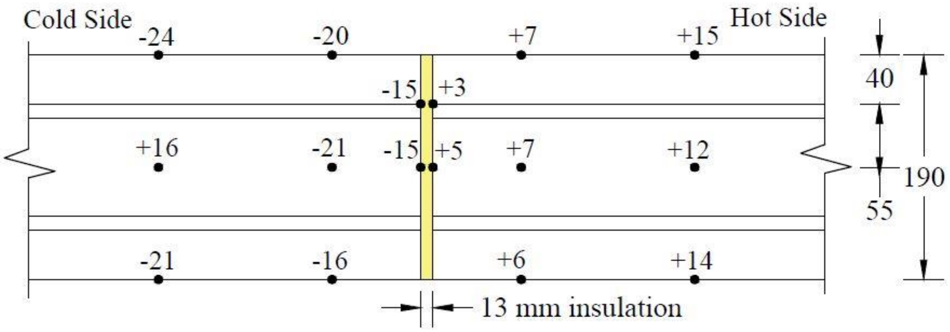

Section A-A [Thermistors] - AR1

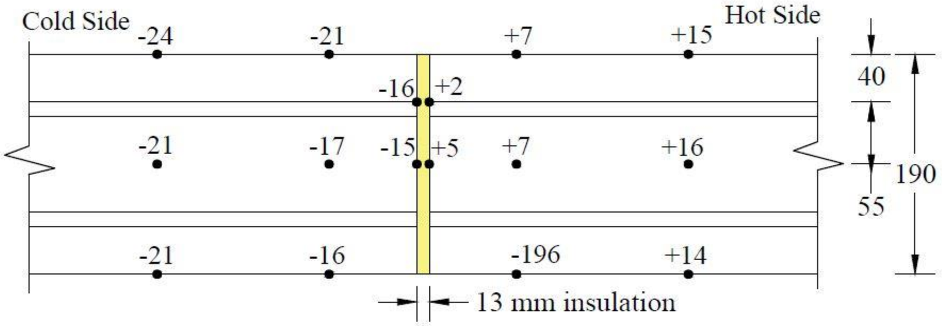

Section B-B [Thermistors] - AR1

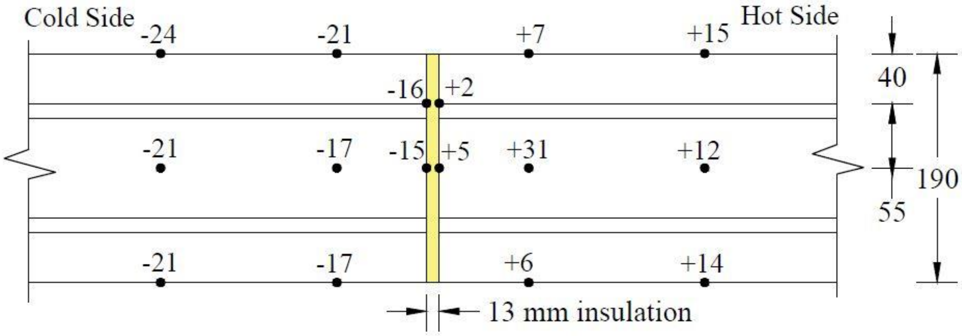

Section C-C [Thermistors] - AR1

Figure 39 Sections AA/ BB/ CC for AR1 – SS1

Figure 40 shows the location and recorded temperature of each thermistor for the first AR2 steady state case. The AR2 temperature distribution in sections A-A, B-B and C-C, accounting for thermistor errors, are nominally the same. In this case, the temperatures on the top and bottom surfaces of the cold side are lower than the middle temperatures suggesting a weak convection effect at the top and bottom surfaces that lowers the temperatures. The temperature difference across the Armatherm^{TM} 500 for sections A-A and CC are lower where the thermistors are attached to the rebar, indicating locally higher heat transfer rates through the Armatherm ^{TM} 500 at the rebar.

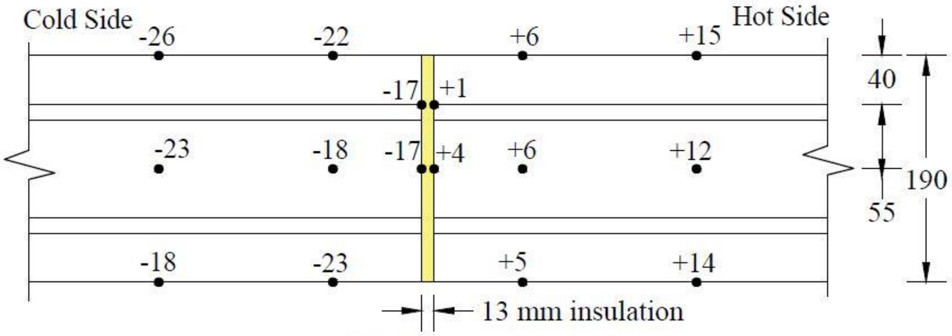

Section A-A [Thermistors] - AR2

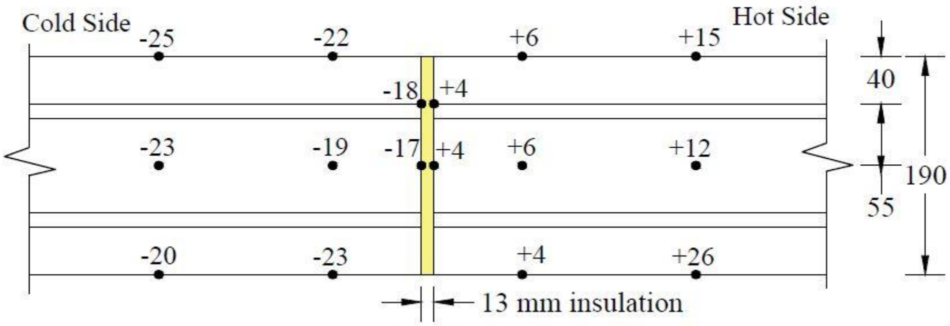

Section B-B [Thermistors] - AR2

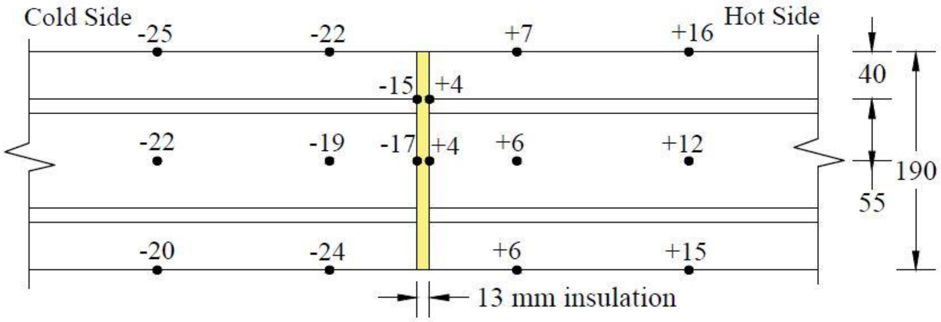

Section C-C [Thermistors] - AR2

Figure 40 Sections AA/ BB/ CC for AR2 – SS1

6.3 DOW1 and DOW2

This section discusses the temperature distribution through the slabs with DOW thermal barriers. Thermistor placement for all slabs was the same and is defined in Figure 41. Section CC of DOW1 was placed next to section AA of DOW2. In each slab a 13 mm thick DOW insulation separated the cold and hot ends.

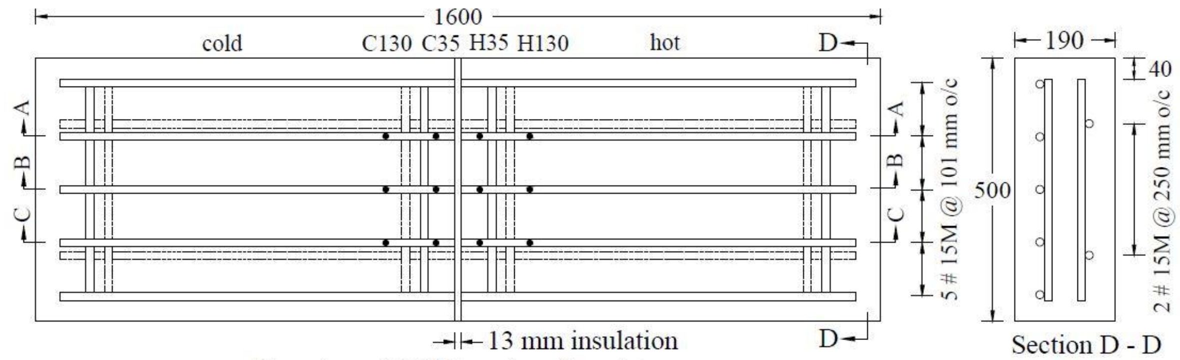

Top view - DOW1 surface thermistors

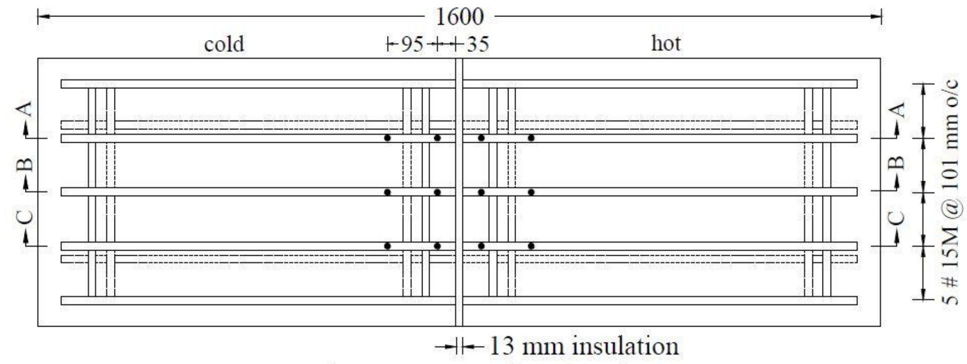

Top view - DOW2 surface thermistors

Figure 41 Drawings of DOW1 and DOW2 inside thermal chamber

DOW1 and DOW2 were tested at steady state temperature of -30 °C / +21 °C. Table 29 shows the average temperature recorded by each thermistor in sections A, B, and C on both cold and hot sides of DOW1 and DOW2. Some values in Table 29 do not make sense, and have been underlined.

Table 29 SS1 temperatures for DOW1 and DOW2

Thermistor Name	SS1 Temperatures for DOW1			SS1 Temperatures for DOW2		
	Section [A]	Section [B]	Section [C]	Section [A]	Section [B]	Section [C]
C35 – T	-17.87	-16.95	-15.92	-19.06	-19.41	-18.77
C130 – T	-20.82	-20.26	-19.76	-22.58	-22.01	+21.96
C0 – R	-10.32	-11.15	-11.35	-13.78	+416853	-14.05
C0 – M	-11.74	-11.48	-10.55	-14.05	-14.41	-14.26
C35 – M	-13.75	-13.59	-12.43	-17.44	-17.54	-16.22
C130 – M	-18.80	-18.14	-17.98	-20.19	-22.40	-23.08
C35 – B	-14.33	-13.25	-12.56	-14.90	-15.33	-14.89
C130 – B	-19.54	-18.98	-17.90	-21.68	-21.23	-21.04
H35 – T	+6.39	+6.39	+7.57	+4.76	+4.37	+3.91
H130 – T	+12.44	+12.97	+14.00	+11.40	+11.26	+11.64
H0 – R	+3.06	+3.39	+4.41	+1.73	+0.98	+1.37
H0 – M	+4.31	+4.98	+5.34	+2.50	+2.49	+2.53
H35 – M	+6.45	+6.86	+7.38	+3.28	+4.59	+4.14
H130 – M	+11.47	+11.46	+12.31	+5.69	+9.46	+9.79
H35 – B	+6.41	+8.93	+9.00	+416853	+4.29	-185.31
H130 – B	+13.50	+13.55	-183	+11.72	-183.89	+14.44

Figure 42 shows the location and recorded temperature of each thermistor for the first DOW1 steady state case. The DOW1 temperature distribution in sections A-A, B-B and C-C, accounting for thermistor errors, are nominally the same. In this case, the temperatures on the top and bottom surfaces of the cold side are lower than the middle temperatures suggesting a weak convection effect at the top and bottom surfaces that lowers the temperatures.

The temperature difference across the DOW insulation for sections A-A and C-C are lower where the thermistors are attached to the rebar, indicating locally higher heat transfer rates through the DOW insulation at the rebar.

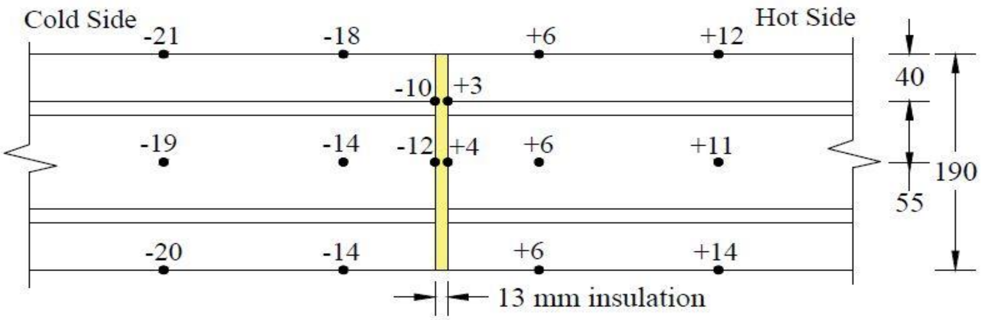

Section A-A [Thermistors] - DOW1 - SS1

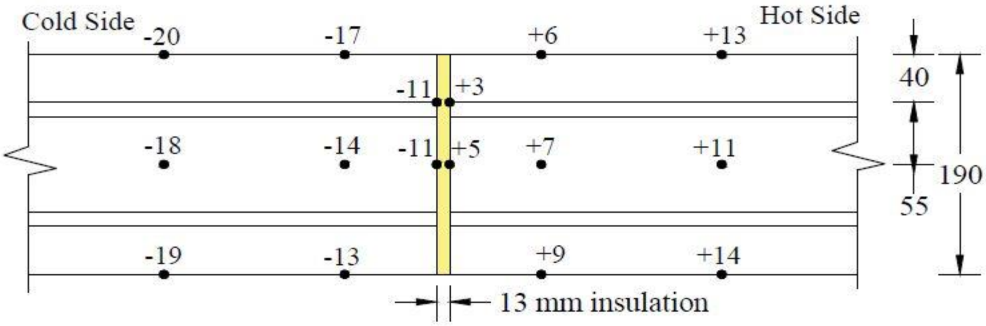

Section B-B [Thermistors] - DOW1 - SS1

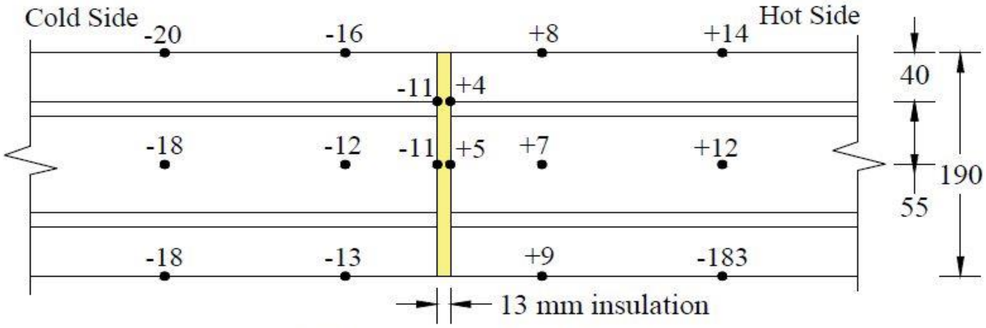

Section C-C [Thermistors] - DOW1 - SS1

Figure 42 Sections AA/ BB/ CC for DOW1 – SS1

Figure 43 shows the location and recorded temperature of each thermistor for the first DOW2 steady state case. The DOW2 temperature distribution in sections A-A, B-B and C-C, accounting for thermistor errors, are nominally the same. In this case, the temperatures on the top and bottom surfaces of the cold side are lower than the middle temperatures suggesting a weak convection effect at the top and bottom surfaces that lowers the temperatures. The temperature difference across the DOW insulation for sections A-A and C-C are lower where the thermistors are attached to the rebar, indicating locally higher heat transfer rates through the DOW insulation at the rebar.

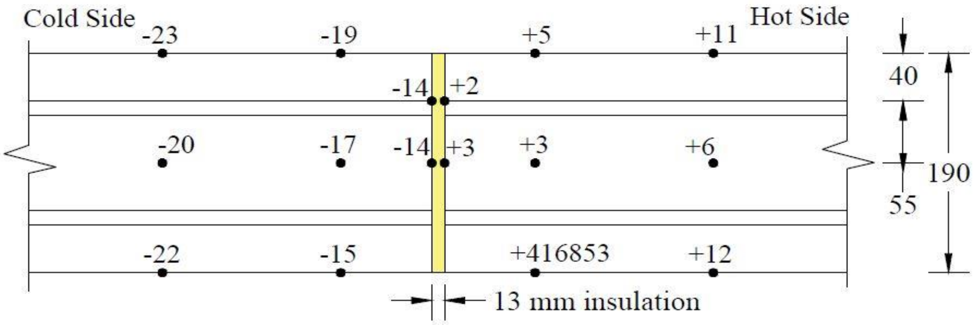

Section A-A [Thermistors] - DOW2 - SS1

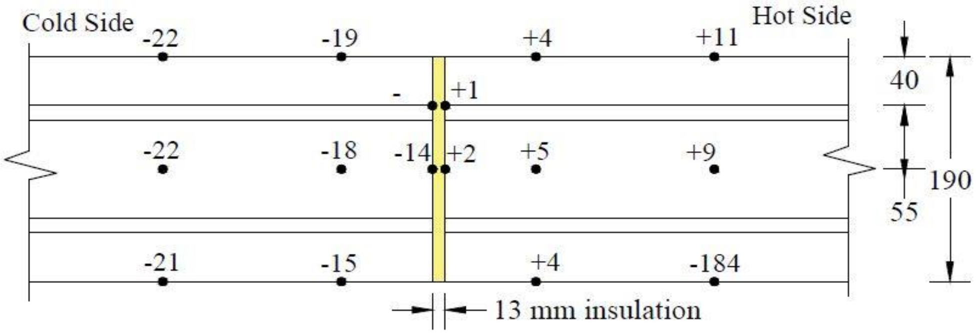

Section B-B [Thermistors] - DOW2 - SS1

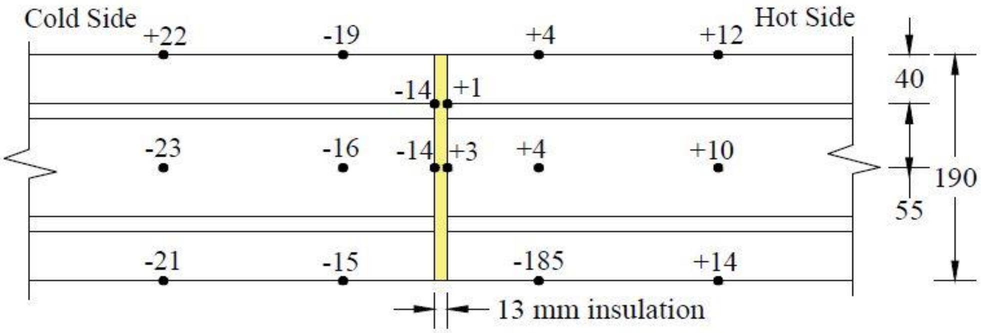

Section C-C [Thermistors] - DOW2 - SS1

Figure 43 Sections AA/ BB/ CC for DOW2 – SS1

6.4 UHMW1 and UHMW2

Figure 44 shows a drawing of UHMW1 and UHMW2 slabs with thermistor placement. Section AA of UHMW1 slab was placed next to section CC of UHMW2 slab. In each slab 13 mm thick UHMW insulation separated the cold and hot ends.

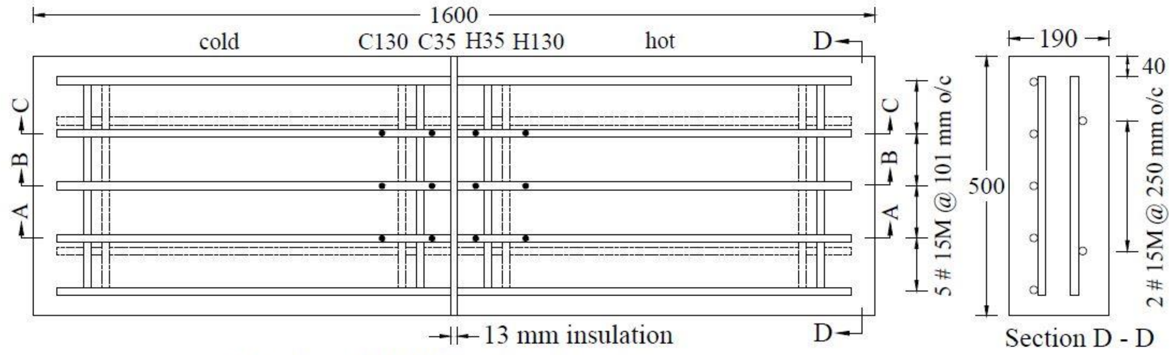

Top view - UHMW1 surface thermistors

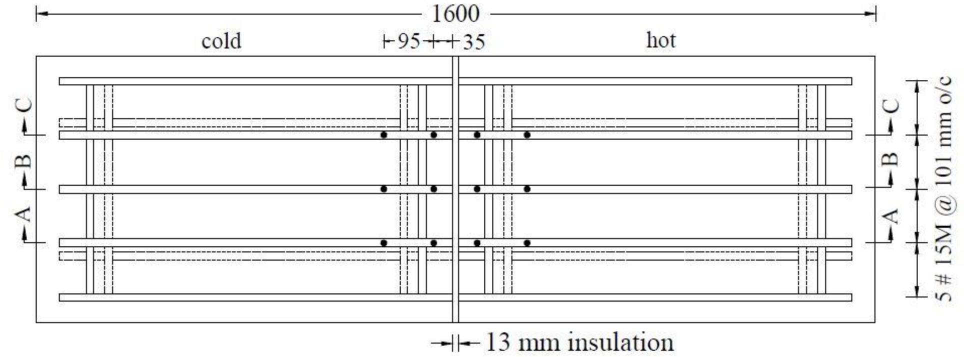

Top view - UHMW2 surface thermistors

Figure 44 Drawings of UHMW1 and UHMW2 specimens inside thermal chamber

UHMW1 and UHMW2 were tested at steady state temperature of -30 °C / +21 °C. Table 30 shows the average temperature recorded by each thermistor in sections A, B, and C on both cold and hot sides of UHMW1 and UHMW2. Some values in the Table 30 do not make sense, and have been underlined.

Table 30 SS1 temperatures for UHMW1 and UHMW2

Thermistor Name	SS1 Temperatures for UHMW1			SS1 Temperatures for UHMW2		
	Section [A]	Section [B]	Section [C]	Section [A]	Section [B]	Section [C]
C35 – T	-16.62	-15.72	-15.72	-12.58	-12.53	-13.98
C130 – T	-19.93	-20.20	-19.94	-18.08	-18.88	-19.38
C0 – R	-10.15	-10.24	-10.29	-7.36	-7.49	-7.94
C0 – M	-9.00	-10.04	-9.12	-6.82	-6.95	-7.43
C35 – M	-11.74	-12.29	-12.01	-8.89	-10.15	-10.17
C130 – M	-16.97	-17.44	-17.32	-14.98	-15.96	-16.37
C35 – B	-12.92	-13.02	-14.14	-23.55	-12.21	-11.42
C130 – B	-18.18	-18.46	-18.72	-16.92	-16.97	-18.28
H35 – T	-1.77	-1.60	-1.43	+2.48	+2.29	+2.01
H130 – T	+8.05	+8.57	+8.64	+20.87	+9.99	+9.49
H0 – R	-4.56	-4.57	-4.20	-1.56	-1.40	-1.96
H0 – M	-3.66	-3.71	-2.83	-1.24	-1.34	-3.41
H35 – M	-31	-1.18	-1.03	+0.08	+1.48	-19.07
H130 – M	+5.97	+5.93	+6.06	+8.11	+8.02	+7.66
H35 – B	-0.13	+0.31	+0.90	+31.29	+3.45	+2.39
H130 – B	+8.35	+10.04	+9.62	+11.22	+10.56	+10.78

Figure 45 shows the location and recorded temperature of each thermistor for the first UHMW1 steady state case. The negative temperatures on the hot side of UHMW barrier suggested that the 13 mm UHMW does not provide an adequate thermal barrier between the cold side and hot side of the slab. The UHMW1 temperature distribution in sections A-A, B-B and C-C, accounting for thermistor errors, are nominally the same. In this case, the temperatures on the top and bottom surfaces of the cold side are lower than the middle temperatures due to surface contact with the cold air. The temperature difference across the UHMW1 insulation is nominally the same where the thermistors are attached to rebar and where they are not attached to the rebar. In contrast to the AR and DOW case, in the UHMW1 case it suggests the heat transfer rate through the UHMW insulation at the rebar was not elevated close to the rebar.

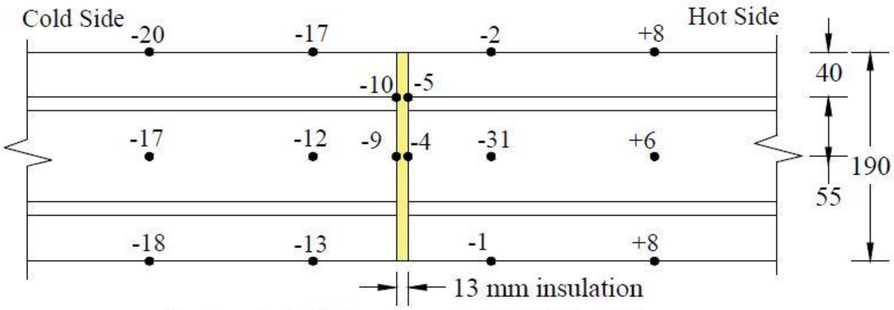

Section A-A [Thermistors] - UHMW1 - SS1

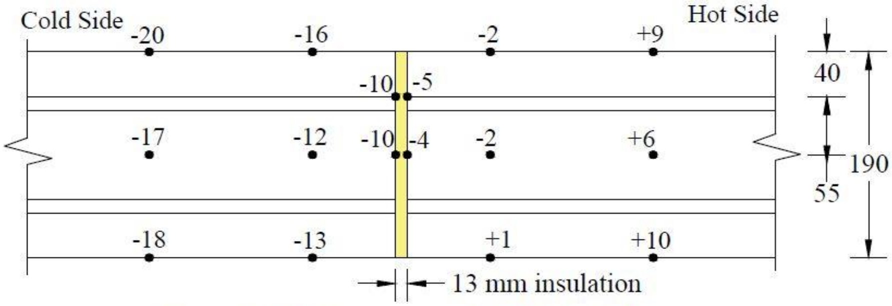

Section B-B [Thermistors] - UHMW1 - SS1

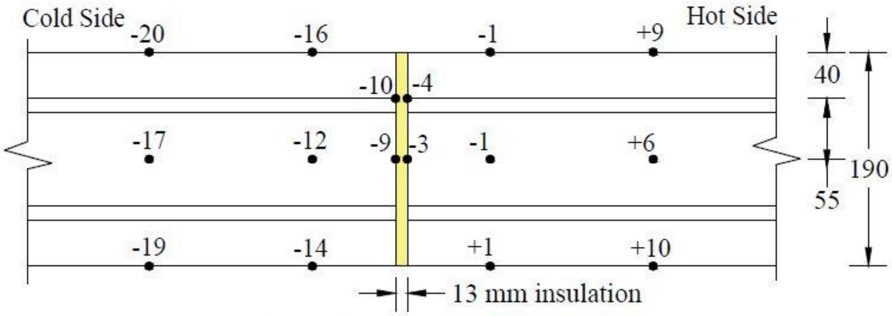

Section C-C [Thermistors] - UHMW1 - SS1

Figure 45 Sections AA/ BB/ CC for UHMW1 – SS1

As can be seen from Figure 45, most of the thermistors which are in contact and close to thermal break on the hot side recorded negative values. This means that there is a relatively high heat transfer rate through UHMW resulting in small temperature differences across the UHMW and lower temperatures that extend well into the hot side (about 50 mm). To be used in a balcony slab, the thermal break is expected to significantly reduce heat transfer and maintain temperatures above the dew temperature on the hot side of the thermal break. In this study, UHMW thermal break did not provide sufficient insulation in the tested balcony slabs.

Figure 46 shows the location and recorded temperature of each thermistor for the first UHMW2 steady state case. The UHMW2 temperature distribution in sections A-A, B-B and C-C, accounting for thermistor errors, are nominally the same. In this case, the temperatures on the top and bottom surfaces of the cold side are lower than the middle temperatures due to surface contact with the cold air. In contrast to the AR and DOW case, there is no distinct trend with respect to the temperature difference across the UHMW insulation where the thermistors are attached to rebar and where they are not attached to the rebar.

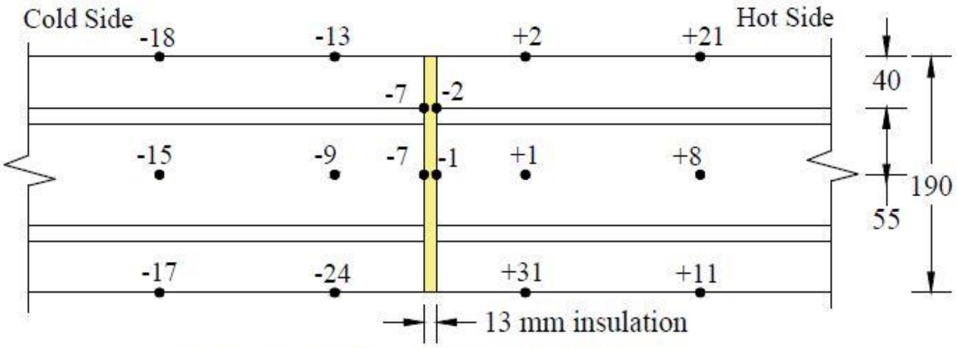

Section A-A [Thermistors] - UHMW2 - SS1

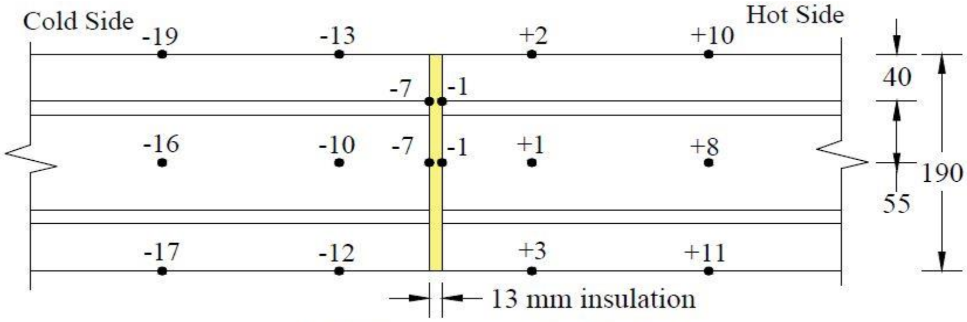

Section B-B [Thermistors] - UHMW2 - SS1

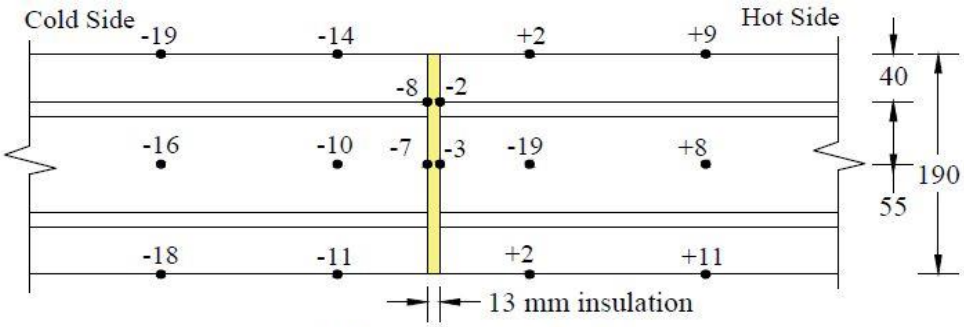

Section C-C [Thermistors] - UHMW2 - SS1

Figure 46 Sections AA/ BB/ CC for UHMW2 – SS1

The general results of UHMW2 are consistent with the UHMW1 results and UHMW is shown to provide insufficient thermal insulation.

The temperature difference across the Dow and Armatherm™ 500 thermal breaks was lower for on rebar thermistors compared to thermistors not attached to rebar by an average of 1.85 and 1.65 °C respectively. This means rebars contributed to conduction of heat between the cold and the hot sides. It must be noted that GFRP rebars are a lot less conductive of heat than steel and as shown by Phase I of this research project, rebar contribution to heat transfer increases when steel is used for reinforcement. The lower temperature difference across thermal break on rebar thermistors was not consistently observed for the UHMW thermal break. There was no distinct trend with respect to the temperature difference across the UHMW insulation where the thermistors are attached to rebar and where they are not attached to the rebar.

Based on the data, it was concluded that Armatherm™ 500 thermal break provided the best insulation in balcony slabs. It prevented heat flow between the inside and outside more than DOW and UHMW. UHMW thermal break provided the least insulation in preventing heat flow from cold side to the hot side. In the specimens fitted with UHMW, thermistors on the hot side recorded negative temperatures.

As mentioned in chapter four, one main purpose of this work was to compare test results with those obtained in Phase I of the program (Boila 2018). Thermal tests for both phases of the program were implemented using the same thermal chambers at Red River College in Winnipeg and under practically the same conditions. Steady state temperatures in Phase I were -31°C and +21°C. In this study steady state temperatures were -30 °C and +21°C.

The key comparison benchmark in thermal tests was the temperature difference observed across the thermal break. Table 31 shows temperature differences across the Armatherm$^{\text{TM}}$ 500 thermal break in two specimens from this study and one specimen from Phase I. Only two Armatherm specimens from this study were thermally tested, and in Phase I only one GFRP reinforced Armatherm specimen was tested thermally. The data shown in Table 31 below were taken from Figures 39 and 40 of this thesis and Figure 38 (a) of Phase I (Boila 2018).

Thermal break thickness in this work was 13 mm, which is half the thickness of the same break in Phase I. As a result, it was expected that the temperature difference along the current specimens would be smaller, i.e., that there would be more heat transfer through the thermal break. The question was by how much. As seen in the Table 31, on average the temperature difference along the current specimens was 26% less than that observed in phase I. Considering that the current breaks were half the thickness, this is an encouraging result.

Table 31 Temperature difference across Armatherm for Phase I (Boila, 2018) & Phase II

Specimen	Average Temperature Difference Across the Break [°C]
AR1 & AR2 – sec A	19.2
AR1 & AR2 – sec C	19.5
AR – previous work	26.6

The next chapter provides an overall discussion of the results of this study as well as the structural and thermal conclusions drawn from the results.

Chapter 7 Conclusions and Recommendations

This chapter includes conclusions drawn from the structural and thermal experimental results of the research, as well as recommendations for future work.

This study was conducted in order to evaluate the thermal and structural performance of three types of thermal breaks in GFRP reinforced concrete cantilevered balcony slabs. A total of eleven balcony slabs were experimentally tested. All specimens were reinforced with #15M GFRP rebars and included a thermal break midway along their length. The dimensions of all specimens were 1600 mm by 500 mm by 190 mm.

Of the nine main specimens, six were tested thermally and all nine were tested structurally. The three types of thermal barriers whose thermal and structural performance was evaluated were: Armatherm^{TM} 500, DOW, and UHMW.

Three pairs of slabs were tested thermally, each pair with the same type of thermal break. Thermal tests were carried out in a dual thermal chamber. Typical Winnipeg winter conditions were simulated in which the cold and hot sides were at about -30 °C and +21 °C respectively. The amount of heat exchange through each slab (and its thermal break) was measured using 10 kΩ thermistors.

Structural tests for all eleven specimens were carried out to failure by applying a static monotonic load at the tip of the cantilever. Strain gauges were installed to measure the strain on rebars. PI gauges were installed on concrete to measure strain, dilation between thermal break and concrete, as well as crack widths in concrete. The deflection due to a static monotonic load applied at the cantilevered end was measured using an LVDT.

The results show that specimens with Armatherm^{TM} 500 exhibited a better thermal and structural performance than specimens with DOW thermal break. Specimens with UHMW thermal breaks did not perform as well, both structurally and thermally.

The results of this work may be used by future researchers with an interest in balcony thermal break systems.

7.1 Conclusions from Thermal Tests

In thermal chamber experiments, in specimens with Armatherm^{TM} 500, on average, the temperature difference across the thermal break was 27% and 72% greater than the temperature difference across the thermal breaks in DOW and UHMW specimens, respectively.

In specimens with Armatherm^{TM} 500 no negative temperatures were recorded on the hot side. But in specimens with UHMW negative temperature values were recorded on the hot side, which means UHMW was not an efficient thermal barrier. DOW break was more efficient than UHMW by 45%, but less efficient than Armatherm^{TM} 500 by 27%. Temperatures recorded by the on-rebar thermistors close to the thermal break on the hot side of DOW specimens were on average 13% lower than temperatures recorded by the similar thermistors for Armatherm^{TM} 500 specimens. That showed that DOW was not as efficient as Armatherm^{TM} 500 in reducing heat loss from the hot side to the cold side of the concrete slab.

The thermal results obtained from the testing of specimens are in line with the information provided by the suppliers of these products according to which the thermal conductivity of Armatherm^{TM} 500 is 0.0562 W/mK which is smaller than that of DOW at 0.2306 W/mK, and UHMW at 0.4093 W/mK.

It was concluded that Armatherm^{TM} 500 is the most effective thermal barrier to reduce heat loss through balcony slabs. For DOW specimens no negative temperatures were recorded on the hot side. In contrast, specimens with UHMW thermal break were not effective in preventing heat flow.

7.2 Conclusions from Structural Tests

The average dilation between thermal break and concrete in Armatherm specimens of this Phase was less than that of Armatherm specimens in Phase I: at service load the initial two specimens of this study showed 47%, 70% and 25% smaller dilation compared with specimens 1, 2 and 3 in Boila's study, respectively. Thus, it can be concluded that using a larger number of smaller diameter GFRP bars reduced the dilation at the thermal break interface with concrete.

From PI gauge data as shown in Figure 21, the dilation between Armatherm^{TM} 500 and concrete was the smallest among the three types of thermal breaks in this study: at service load the dilation in slabs with Armatherm^{TM} 500 was 33% and 18% smaller than the dilation in slabs with DOW and UHMW thermal breaks, respectively.

All specimens in this work failed in shear. Specimens with DOW break showed the largest average failure load of 81.5 kN, which was 20% and 4% larger than specimens with Armatherm^{TM} 500 and UHMW breaks respectively.

Armatherm^{TM} 500 specimens had the smallest deflection at service load: Results from LVDT sensors at service load indicated that the largest deflection in Armatherm^{TM} 500 slabs was 27% and 42% smaller than the largest deflections in UHMW and DOW slabs respectively.

In summary, from the three types of thermal breaks considered in this study, Armatherm^{TM} 500 is a better thermal break in combination with GFRP reinforcement in the slabs tested. Structural tests in this study showed that this combination has an acceptable structural performance at service load.

For use in structural applications, the bond between thermal break and concrete must be made stronger such that the first sign of dilation at the interface initiates at higher loads. Otherwise, if dilation happens at lower loads, water may start to seep into the structure and cause serviceability problems.

7.3 Recommendations for Future Work

Using novel materials instead of steel to reinforce structures is still in its infancy. GFRP is one of the most promising materials to replace steel. Including a thermal barrier means that structures such as balconies will be better insulated and, as a result, buildings will exchange less heat with the outside. The key challenge is whether the combination of thermal break and GFRP reinforcement will provide the desired structural and thermal performance. This thesis contributed to investigating this question. Below are some recommendations for future work.

Further tests may be done using DOW because its thermal performance was acceptable: there were no negative temperatures recorded on the hot side of DOW thermal break. Moreover, it showed the highest failure load during structural testing.

There are other thermal barriers on the market as well, such as the one produced by Schöck Isokorb®. Future work does not have to be limited to the thermal breaks that were tested in this work.

In this study the surface of the thermal breaks were not treated to increase bond with concrete. Future research should consider ways to increase the bond between thermal break and concrete.

Although the general thermal properties of the materials which make up the thermal breaks in this study were provided by their suppliers, it would still have been helpful to directly test the materials' thermal properties. This was to be done as part of this study, in Red River College, but an appropriate apparatus was not available at the time this study took place. Future research may consider directly testing thermal break materials for their thermal properties.

References

ACI Committee 440. (2015). Guide for the Design and Construction of Structural Concrete Reinforced with FRP Bars - ACI 440.1R-15.

Armadillo. (2019). Armatherm^{TM} Thermal Break Connections.

ASTM International. (2019). Standard Test Method for Compressive Strength of Cylindrical Concrete Specimens (C39/C39M - 18). West Conshohocken, PA 19428-2959. United States.

B&B FRP Manufacturing Inc. (2018). Why GFRP Rebars & Not Steel. Retrieved from https://www.bandbfrp.com/whygfrprebar

Boila, S. N. (2018). Thermal & Structural Performance of a Cast in Place Reinforced Concrete Balcony Thermal Break. Manitoba.

Chafik, M. (2015). Investigate the Impact of a Low U-Value Framing Condition and an Insulated Curb Condition at Cantilevered Concrete Balcony Slabs in High-Rise MURBs. Ryerson.

Concrete Construction. (2019). Insulating Concrete Balconies. Retrieved from https://www.concreteconstruction.net/how-to/materials/insulating-concrete-balconies_o

CSA-S6. (2019). Commentary on CAN/CSA-S6-19 , Canadian Highway Bridge Design Code.

CSA S806. (2017). Design and Construction of Building Structures with Fibre-Reinforced Polymers.

Dacko, T. (2020). Thermal Breaks Provide Energy Efficiency in Concrete Reinforced Condo. Retrieved from https://www.forconstructionpros.com/concrete/article/21106578/thermal-breaks-provide-energy-efficiency-in-concrete-reinforced-condo

Eugenijus, G., Edgaras, T., Gribniak, V., & Gintaris Kaklauskas, Aleksandr K. Arnautov, V. T. (2013). FRP Reinforcement for Concrete Structures. Engineering Structures and Technologies. Taylor & Francis. Retrieved from https://www.researchgate.net/publication/288828931_Application_of_FRP_in_Concrete_Structures

Fabreeka International Inc. (2016). Fabreeka-TIM Structural Thermal Break. Thermal Insulation Material.

Faza, S. S. (1991). Bending and Bond Behavior and Design of Concrete Beams Reinforced with Fiber-Reinforced Plastic Rebars. West Virginia.

GangaRao, H. V. S., Taly, N., & Vijay, P. V. (2007). Reinforced Concrete Design with FRP Composites. (Taylor & Francis Group, Ed.). New York: CRC Press.

Ge, H., Ruth McClung, V., & Zhang, S. (2013). Impact of Balcony Thermal Bridges on the Overall Thermal Performance of Multi-Unit Residential Buildings: A Case Study. Energy & Buildings, 60, 163–173.

Goulouti, K. (2016). Thermal and Structural Performance of a New Fiber-Reinforced Polymer Thermal Break for Energy-Efficient Constructions. École Polytechnique Fédérale de Lausanne, Switzerland.

Goulouti, K., Castro, J. De, & Keller, T. (2015). Aramid/Glass Fiber-Reinforced Thermal Break - Thermal and Structural Performance. Composite Structures, 136, 113–123.

Goulouti, K., Castro, J. De, & Keller, T. (2016). Aramid/Glass Fiber-Reinforced Thermal Break - Structural System Performance. Composite Structures, 152, 455–463.

Günaslan, S. E., Karaşin, A., & Öncü, M. E. (2014). Properties of FRP Materials for Strengthening. IJISET, 1(09 December).

ISIS Canada. (2007). Reinforcing Concrete Structures with Fibre Reinforced Polymers - Design Manual No.3 (2nd ed.). Winnipeg.

Jasper Plastics. (2020). JP Series Polyurethane Thermal Column Bearing Blocks. Retrieved from https://www.jasperplastics.info/thermal-bearing-blocks

Jeetendra, C., Suresh, K., & Hussain, A. (2015). Application of FRP in Concrete Structures. International Journal of Engineering Associates, 4(December), 50–51. Retrieved from https://www.researchgate.net/publication/288828931_Application_of_FRP_in_Concrete_Structures

Johnston Industrial Plastics. (2018). UHMW Polyethylene Rod. Johnston Industrial Plastics Limited. Winnipeg. Retrieved from https://www.johnstonplastics.com

Nanni, A., Luca, A. De, & Zadeh, H. J. (2014). Reinforced Concrete with FRP Bars Mechanics and Design. (Taylor & Francis Group, Ed.). New York: CRC Press.

National Research Council Canada. (2015). National Building Code of Canada (Fourteenth). Ottawa: Canadian Commission on Building and Fire Codes, NRC Canada.

Pultrall. (2018). Glass Fiber Reinforcement Polymer (GFRP). Retrieved from https://www.pultrall.com/dbfiles/Document/36201834822PMDOCen54.pdf

RDH. (2013). The Importance of Slab Edge & Balcony Thermal Bridges, Report #4.

Saunders, P. (2020). Improving Insulation for Retirement Residences. Retrieved from https://www.canadianconsultingengineer.com

TE Connectivity. (2020). Steinhart & Hart Equation for 10 kΩ Thermistors. Retrieved from www.meas-spec.com

Technical Products Inc. (2018). UHMW Material Specifications. Retrieved from https://www.technicalproductsinc.com/pdf/Specs/UHMW Specs.pdf

Appendix A – Structural Test Results for Two Initial Specimens

A key initial objective of the experimental program was to evaluate the serviceability performance of GFRP reinforced balcony slabs with thermal break. Two initial specimens were tested with 25 mm Armatherm^{TM} 500 thermal break, and 5 #15M GFRP rebars. Similar specimens had been previously tested by Boila with the same thermal break, and 2 #25M GFRP bars (2018).

This step was designed to investigate the effect of increasing the number of reinforcing bars on the dilation at the thermal break. See Table A1 and Figure A1 for reinforcement details, with all dimensions in mm.

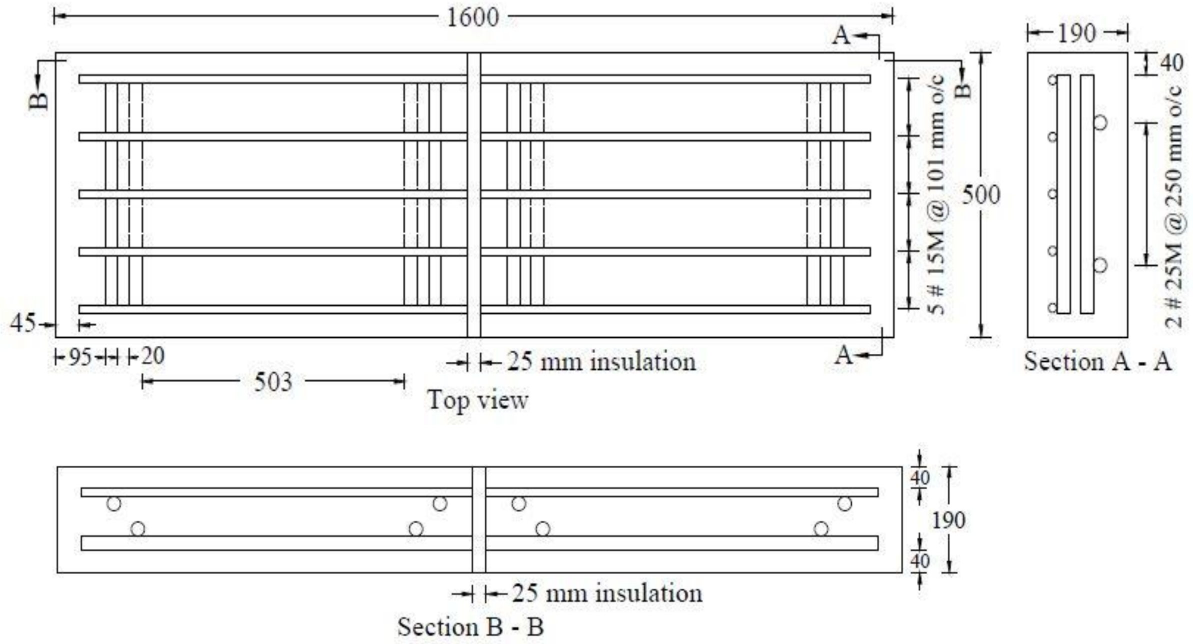

Figure A 1 GFRP reinforced slab (all dimensions are in mm)

A.1 Test Specimen GFRP Reinforcement Area and Number of Rebars

In the design calculations for a full scale balcony slab in Phase I, Boila (2018) considered 4 #25M top rebars. For this Phase a decision was made by the research team to instead consider 10 #15M top rebars for a full scale balcony slab. The following calculation was done to show that 4 #25M and 10 #15M GFRP rebars provide the same reinforcement area. It must be noted that specimens in both Phase I and Phase II were cut-outs of full scale balcony slabs because the lifting equipment at Red River College in Winnipeg could not lift full scale balconies into the thermal chamber. The cut-out specimens in Phase I had 2 #25M top rebars while the cut-out specimens in this work had 5 #15M rebars.

The following procedure is the calculation of the area and number of #15M GFRP rebars which provide the same area of reinforcement as in Phase I by Boila (2018). The same area of reinforcement was considered so that the results from this work can be compared with the results from Phase I.

Top reinforcement area for full scale specimens:

Area #25M = 572.3 mm^2 (Pultrall, 2018)
Area #15M = 232.9 mm^2 (Pultrall, 2018)

4 # 25M = 4 (572.3 mm^2) = 2289 mm^2 area of top rebars for Phase I
10 # 15M = 10 (232.9 mm^2) = 2329 mm^2 area of top rebars for Phase II

Top reinforcement area for the cut-out specimens:

Area of 2 #25M = 2 (572.3 mm^2) = 1145 mm^2 area of top rebars for Phase I
Area of 5 #15M = 2 (232.9 mm^2) = 1165 mm^2 area of top rebars for Phase II

Spacing of top rebars:

Spacing = (width) (area #15)/ (total area) = (500) (232.9)/ (1165) = 101 mm (ISIS Canada, 2007). Therefore, 5 #15M @ 101 mm o/c were used for top reinforcement in each specimen in this work.

Due to shear lag, fibers near the outer surface are stressed more than those near the center of the bar (Faza, 1991). Therefore, tensile strength depends on bar diameter. Smaller diameter bars are more efficient.

A.2 General – Description of Specimens

Two specimens were built and structurally tested to failure. Both specimens had a 25 mm Armatherm^{TM} 500 thermal break. The two sides of the slab on which PI gauges were installed were denoted as west and east. The strain gauges were labeled based on the three longitudinal sections of AA, BB, and CC as shown in Figure A2 with all dimensions are in mm.

Table A 1 Reinforcement for the two initial specimens

# Specimens	Specimen Reinforcement	Bar Spacing [mm]	Thermal Break
2	top: 5 #15M GFRP	101	25mm Armatherm $^{\text{TM}}$ 500
	bottom: 2 #25M GFRP	250	

A.3 Instrumentation

Strain gauges, PI gauges, and LVDT were installed on the two specimens tested at the beginning of this research. This section describes the preparation and instrumentation of the two initial specimens.

Strain Gauges: The purpose of using strain gauges is to measure the longitudinal strain on rebars. A total of three strain gauges (350 ohm) were used in each specimen. Strain gauges were installed on top of the following rebars: middle-top [MT] on section BB, and middle-bottom [MB] on sections AA, and CC. Strain gauges were installed at points where rebars crossed the thermal break. Therefore, gauges were inside the thermal break. Instrumentation is shown in Figure A2, where the red dots represent the strain gauges.

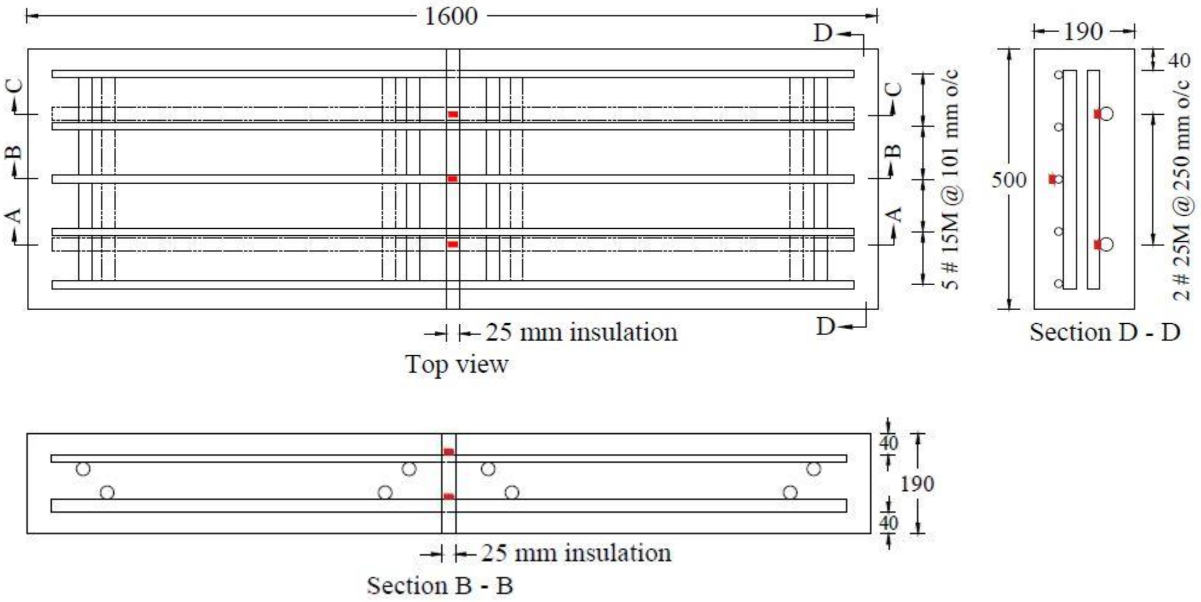

Figure A 2 Location of strain gauges shown as red dots

PI Gauges: The purpose of using PI gauges is to measure the strain and crack widths on concrete as well as measuring the dilation between the concrete and thermal break. A total of four 200 mm PI gauges were installed on the west and east sides of both specimens. One PI gauge was installed in the tension area on top of the west side, and another PI gauge was installed in compression at the bottom of the west side. The same was done on the east side. On the west side the top and bottom PI gauges, named PI gauges 4 and 3 respectively, were installed just behind the thermal break, on the support side of the slab (north). For the east side the top and bottom PI gauges, named PI gauges 1 and 2 respectively, were installed such that they crossed the thermal break towards the support part of the slab. See Figure A3 for a sketch of PI gauge locations on both specimens.

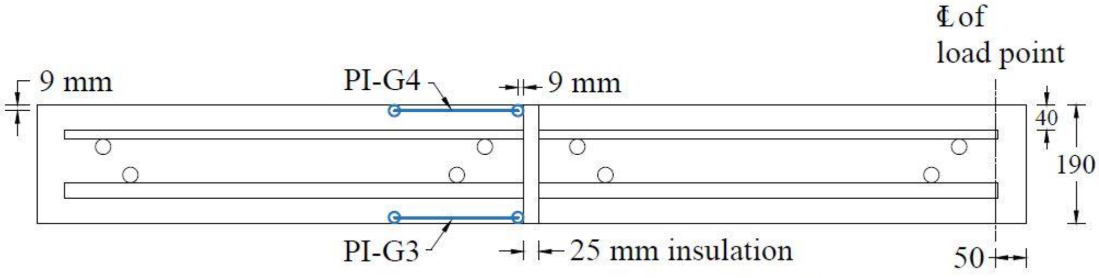

West edge - PI gauges behind thermal break

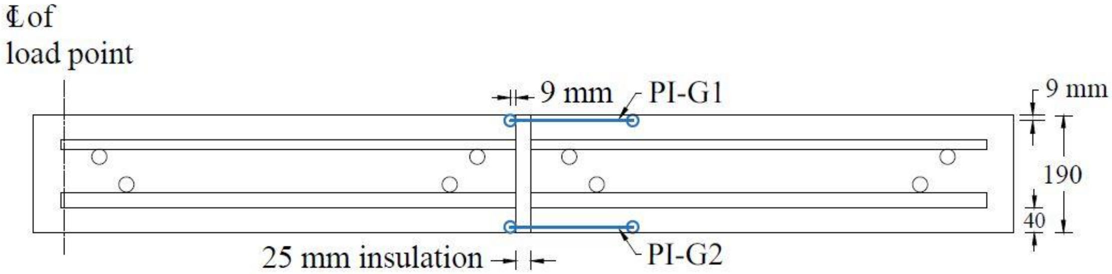

East edge - PI gauges crossing thermal break

Figure A 3 Sketch of PI gauges for specimens

Linear Variable Deflection Transducers (LVDT): For both specimens, an LVDT was installed at the cantilever end. As can be seen in Figure A4, the LVDT was 90 mm away from the load point. The two specimens were tested structurally to failure by the application of a static monotonic load at the tip of the cantilever. The test was carried out under deflection control and was set at 2 mm/minutes. The test for each specimen lasted about an hour.

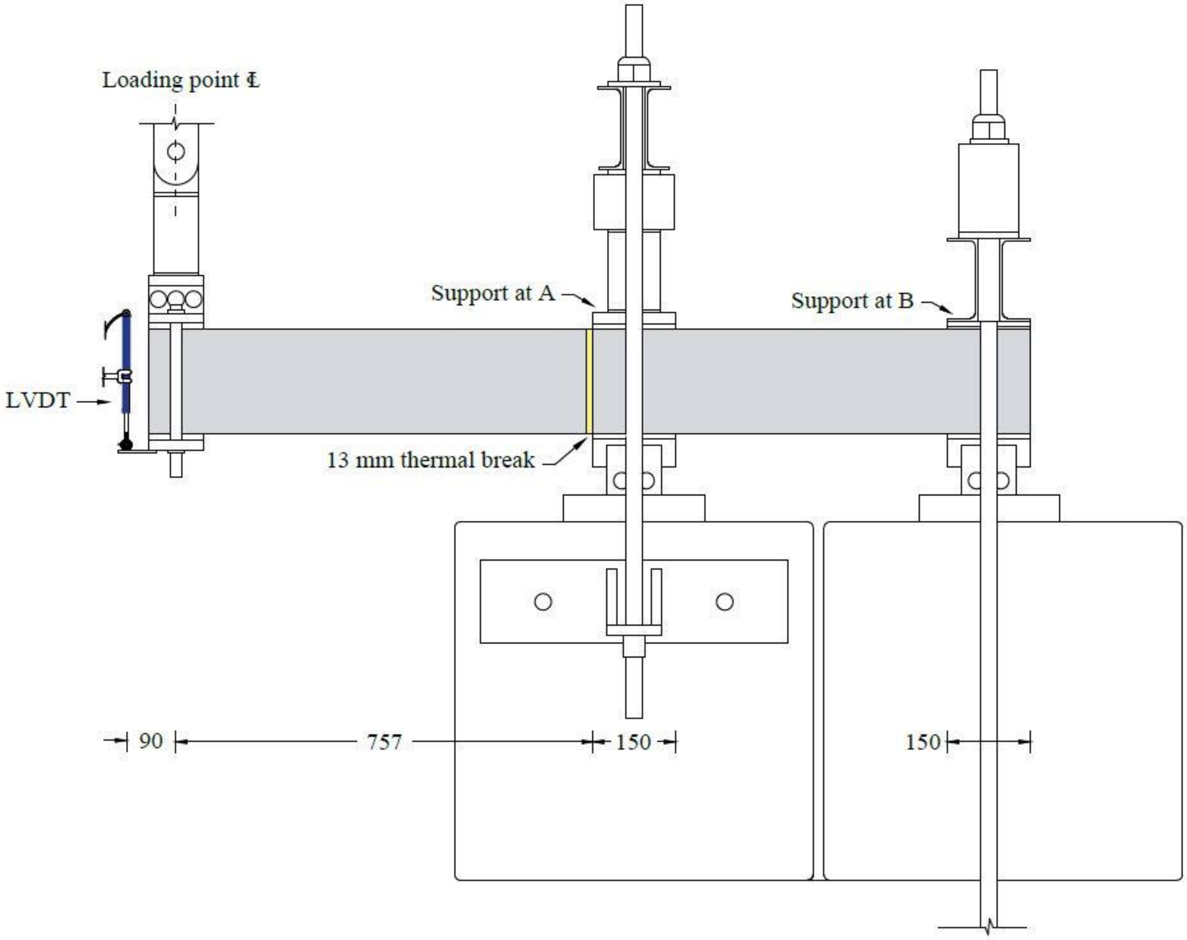

Figure A 4 LVDT position from loading point (all dimensions are in mm)

A.4 Test Results

Strain in the Reinforcement: The strain data in the tension reinforcement were plotted versus load [kN] until failure. Figure A5 shows strain results for the two initial specimens. For each specimen three strain gauges were installed on the reinforcement at the location of the thermal break. One strain gauge in the middle of top rebar (MT) on section BB to measure the maximum tensile strains, and the two strain gauges in the middle of the bottom rebars (MB) on sections AA and CC to monitor if the specimen was loaded symmetrically. As an example: MB-CC means that the strain gauge is positioned on the middle of the bottom rebar on section CC.

From Figures A5 (a) and (b), the two plots of strain in reinforcement from both specimens are similar. Since the strain gauges were installed inside the thermal break, the top strain gauges did not show any change in stiffness at first cracking. It was observed during testing that the first cracks appeared at loads of 14 kN and 9.7 kN in the first and second specimens, respectively. After the first crack, the bottom rebar strains shifted to positive strains which is a sign that the neutral axis moved below the bottom rebars. In the first specimen a difference between the strain at the two bottom gauge lines MB-CC and MB-AA was observed. The strain graph of middle bottom MB-AA shows larger positive strains compared to MB-CC strain gauge. This means that the slab was not loaded symmetrically, and that section AA experienced larger loads in comparison to section CC. This is possible for many reasons, such as the support was not leveled properly, or the slab had more significant cracking on section AA. The maximum failure load for the first specimen was 71 kN and the maximum load for the second specimen was 77 kN.

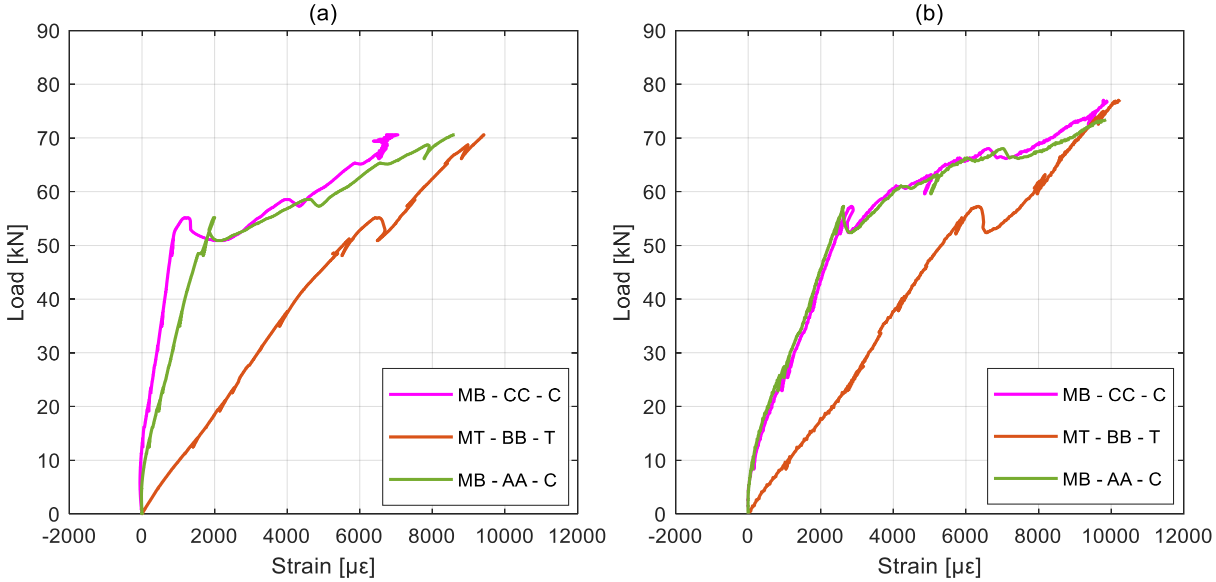

Figure A 5 Strain in reinforcement at maximum moment location: (a) slab1 and (b) slab2

PI Gauges: PI gauges were installed on each specimen to measure the strain and crack widths on concrete. Figure A6 shows the location of PI gauges on the west and east sides of the second specimen. PI gauge locations for the first specimen were the same as that shown in Figure A6.

Two PI gauges were installed per slab side: PI gauges 1 and 2 were installed on the east side, and 3 and 4 on the west side of the slab. PI gauges 1 and 4 were in tension (on the top) and PI gauges 2 and 3 were in compression (at the bottom). PI gauges 1 and 2 had the thermal break within their gauge length. PI gauge 1 recorded the dilation at the thermal break-concrete interface. PI gauge 2 recorded compression of the thermal break.

(a) west edge (b) east edge

Figure A 6 Location of PI gauges on second specimen

As can be seen in Figure A7, the data from PI gauges was plotted as elongation or contraction in mm with load until failure.

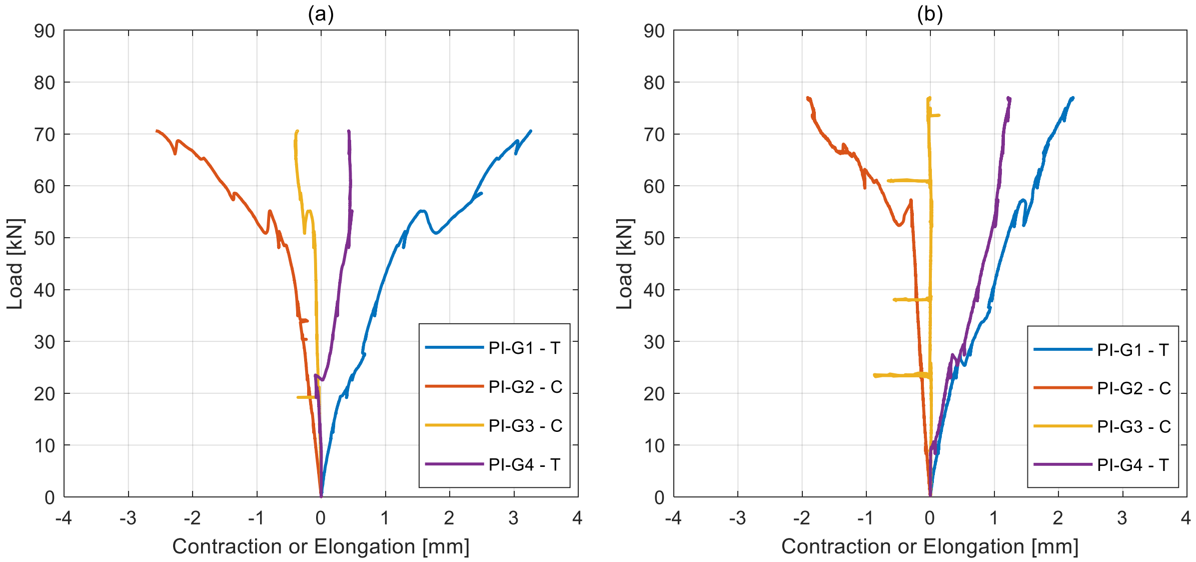

Figure A 7 Contraction and elongation of PI gauges on concrete: (a) slab 1 and (b) slab 2

PI gauge data captured the deformation in concrete and thermal break, as explained below. From Figure A7 (a), the results of PI-G2 and PI-G3 are almost linear up to a load of about 55 kN, followed by a rapid increase in compression. This indicates that the thermal break began to compress more rapidly at that load. The results PI-G1 and PI-G4 are linear up to a load of about 24 kN, followed by a small drop in load. This is a sign that the thermal break began to separate from the concrete at that load. The amount of contraction was -2.6 mm at the bottom of the slab and the amount of elongation was 3.3 mm at the top of the slab. These largest values were recorded in the two gauges that were installed with the thermal break in the gauge length, namely PI-G1 and PI-G2. Similar behaviour was observed in slab 2, shown in Figure A7.

Load Deflection Response: An LVDT was installed at the tip of the cantilevered end of each slab to measure deflection. Figure A8 shows its position.

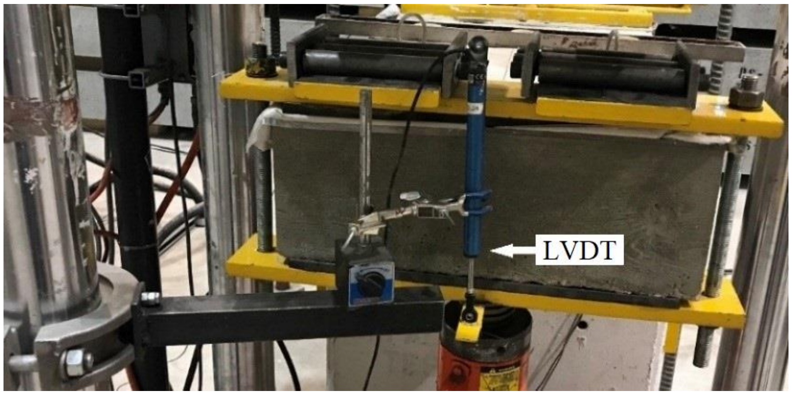

Figure A 8 Location of LVDT on specimens

The test was conducted using deflection control at a rate of 2 mm per minute. The data from LVDT were plotted in Figure A9 as deflections in mm with respect to load until failure.

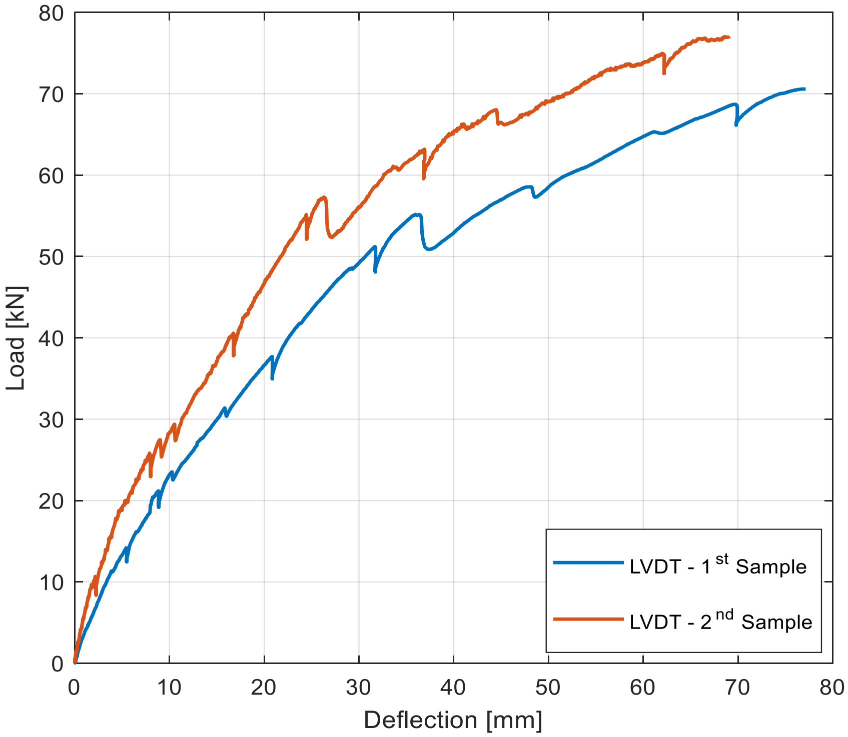

Figure A 9 Load Deflection for the two specimens

The data show a linearly increasing deflection up to a load of about 10 kN when the first cracking has started. The graphs after cracking are non-linear up to a failure load of about 71 and 77 kN for the two specimens, respectively. The nonlinearity of the behaviour after the load of approximately 57 kN is due to the thermal break, as FRP-reinforced specimens exhibit linear behaviour until failure, unless they are heavily reinforced with GFRP rebars. The nonlinearity means that the thermal break was compressing during the testing and affecting the behaviour of the slabs. Maximum deflection for the first and second specimens was 81 mm and 75 mm, respectively.

A.5 Crack Widths

Table A2 shows the dilation between concrete and thermal break and crack width in mm at various loads for the two specimens. Figure A10 shows a cross section of the second specimen, the dilation between thermal break and concrete, as well as the crack locations. The location of cracks on the slab are identified in Figure A10 as ‘A’ and ‘B’ on the two sides of the thermal break. The crack at A is at a distance of 205 mm north of thermal break, while the crack at B is at a distance of 125 mm south of the thermal break.

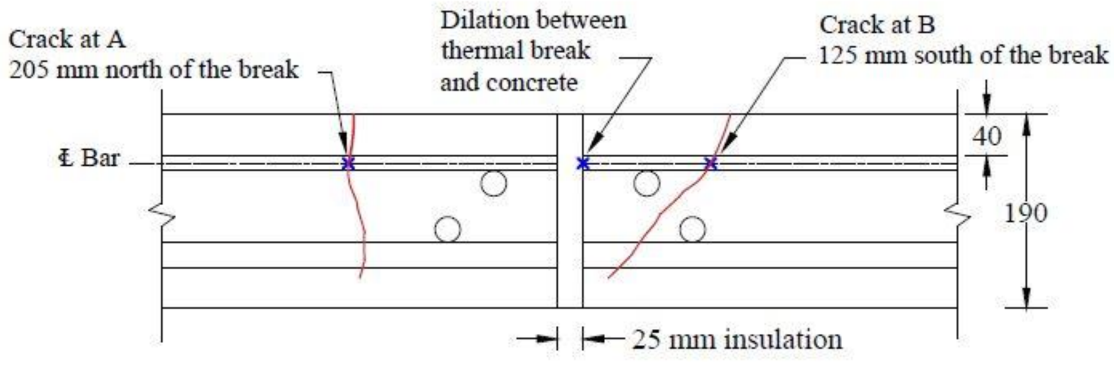

Figure A 10 Dilation and cracking cross section on the west side for the 2nd specimen

The widths of cracks due to various loads as read at the centerline of rebar are summarized in Table A2. Dilations between concrete and thermal break were measured on the west side of the specimen. The first cracks started at loads of 14 kN and 10 kN for the first and second specimens respectively. For the three GFRP reinforced specimens with thermal break tested by Boila (2018) the first crack and dilation started at 15 kN, 14 kN, and 18 kN for the first, second, and third specimens respectively. Thus, the onset of dilation between thermal break and concrete occurred at similar loads for the two initial specimens in this work and in the specimens tested by Boila (2018).

Table A 2 Crack width and dilation

Specimens	Load [kN]	Crack Width at ‘A’ [mm]	Crack Width at ‘B’ [mm]	Dilation Between Concrete and Thermal Break/Crack Width at ‘B’ End [mm]
1st	35	_	_	0.3
	50	_	_	0.3
	67	_	_	0.4
2nd	10	_	_	0.1
	25	0.1	0.05	0.1
	40	0.18	0.13	0.25
	55	0.35	0.13	0.3
	60	0.35	0.15	0.35
	73	0.38	0.4	0.35

Specimens	First Crack [kN]	Maximum Failure Load [kN]
1st	14	71
2nd	10	77

A.6 Failure Mode

The maximum failure loads were 71 kN and 77 kN for the first and second specimens, respectively. Both specimens failed due to shear at a location close to the support and thermal break. Moreover, dilation between thermal break and concrete was not very visible to the naked eye. Figure A11 is a photo of the dilation for the 2nd specimen.

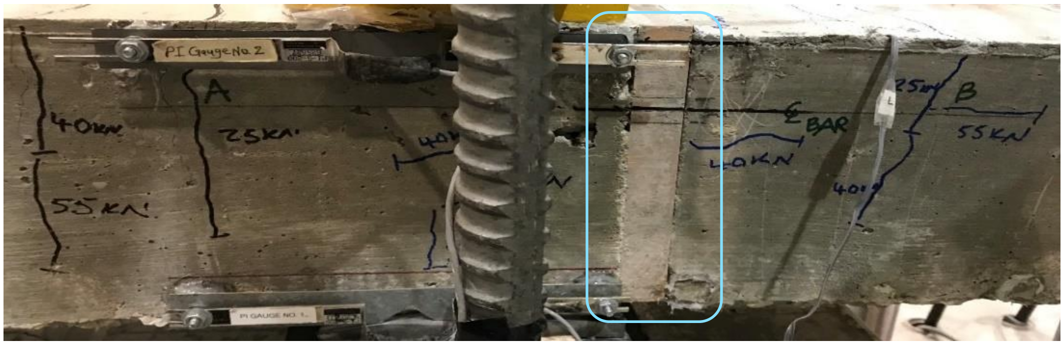

Figure A 11 Dilation between thermal break and concrete, 2nd specimen

A.7 Summary of Results

The initial two specimens were tested with the purpose of comparing the dilation at the thermal break with earlier study by Boila (2018). The only difference between these two specimens and those in the previous work by Boila (2018) was the size and number of the reinforcing bars. The top tension rebars that were previously 2 #25M with a total area of 1145 mm^2 were replaced with 5 #15M with a total area of 1165 mm^2 rebars.

The deflection of specimens 1, 2, and 3 from work by Boila (2018) at a service load of 19.7 kN was 8.83 mm, 8.76 mm, and 8.71 mm, with an average deflection of 8.8 mm. The deflection for the two specimens from this study at the same service load was 8.1 mm and 5.4 mm, with an average deflection of 6.7 mm. Therefore, at a service load of 19.7 kN the average deflection for the two specimens in this study was 24 % smaller compared to the average deflection recorded at the service load by Boila (2018).

Boila (2018) considered a service load of 19.7 kN in their work. In order for the results from this work to be comparable with the results from Boila (2018), the same service load was considered in this work as well.

Data from the top PI-G1 in three specimens tested by Boila (2018) and from the two initial specimens of current work were plotted in Figure A12 to compare the dilation between thermal break and concrete at a service load of 19.7 kN. In both studies, the PI gauges crossed the thermal break and were named PI-G1. In Figure A12, P stands for previous work and C for current work, and the number next to it is the specimen number. Data from three specimens of Boila's work (PI-G1-P1, PI-G1-P2 and PI-G1-P3) and two specimens of this study (PI-G1-C1 and PI-G1-C2) are shown. As seen in Figure A12, the dilations are 0.6, 1.0, and 0. 4 mm for PI-G1-P1, PI-G1-P2, and PI-G1-P3, respectively. The data from PI-G1-C1 and PI-G1-C2 shows a dilation of about 0.3 mm. The initial two specimens of this study show 47%, 70% and 25% smaller dilation compared with specimens 1, 2 and 3 in Boila's study, respectively. It can be concluded that replacement of 2 #25M GFRP rebars with 5 #15M had a positive result on reduction of dilation between thermal break and concrete. The two specimens in this study and all specimens in Boila's study had the same 25 mm Armatherm$^{\text{TM}}$ 500 thermal breaks.

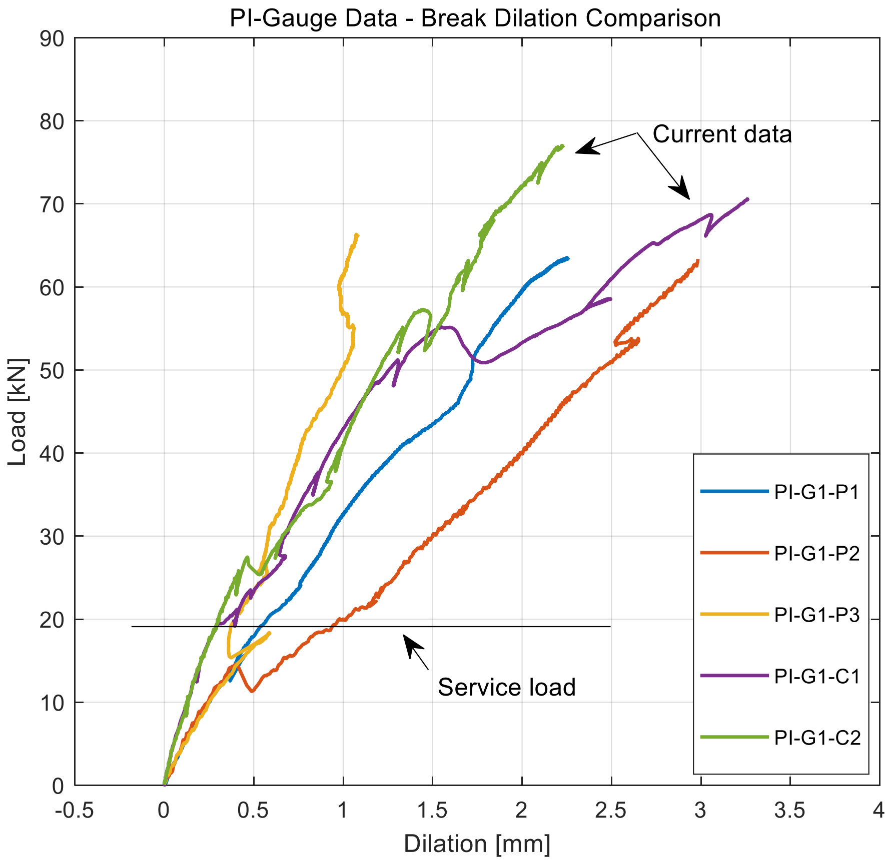

Figure A 12 Top east edge PI gauge results from Boila (2018) and the current study

Since satisfactory structural results were achieved from the two initial specimens, the same reinforcement arrangement was used for the nine main specimens of this study, whose results are discussed in chapter four. The thickness of the thermal break in the nine main specimens was reduced to 13 mm, and three types of thermal breaks were studied.

A.8 Service Load Calculations

Reinforcement concrete density = 25 kN/m^3

Width of slab = 1.0 m based on NBCC 2015 for full scale (1.8 m) balcony slab

Depth of slab = 0.19 m

W_{DL}= (25 kN/m^3) (1m) (0.19m) = 4.75 kN/m is self weight of full-scale balcony

Based on NBCC (National Research Council Canada, 2015) for exterior balconies:

W_{LL}=4.8 kN is the live load for tributary width of 1.0 m

$W_{snow} = I_S [S_s (C_b C_w C_s C_a) + S_r]$

$C_w = C_s = C_a = 1.0$

$C_b = 0.8$

$S_s = 1.9$ kN/m^2 for Winnipeg

$S_r = 0.2$ kN/m^2 for Winnipeg

$I_S = 0.9$ for serviceability limit state (SLS)

$W_{snow} = 0.9 [1.9 (0.8) (1.0) (1.0) (1.0) + 0.2] = (1.55$ kN/m^2) (1m width of full-scale slab) = 1.55 KN/m

$W_{Total} = W_{DL} + W_{LL} + W_{snow}$ = 4.75 kN/m + (4.8 kN/m) + (1.55 kN/m) = 11.1 KN/m

W_{Total} = 11.1 KN/m Total load

Balcony railing self weight

From NBCC 2015, for h = 1070 mm the weight of ¾" glass is 0.478 kN/m^2. We Assume 2 panels of glasses.

P_d = (2) (0.1070 m) (0.478 kN/m^2) = 1 kN/m

P_l = 1.5 kN/m vertical load on guard, from NBCC (4.1.5.14.4)

P = 1 kN/m + 1.5kN/m = 2.5 kN is a line load at the tip of the cantilever

Ms = 11.1 kN/m) (1.8 m) (1.8 m/2) + (2.5 kN) (1.8 m) = 22.48 kN.m

Ms = 22.48 kN.m is the service moment for a full-scale balcony slab of length 1.8 m

For finding an equivalent service point load at the tip of the cantilever:

Ms = (W_S) (1.8 m)

W_S = 22.48 kN.m/ 1.8 m = 12.5 kN

W_S = 12.5 kN is service load for full scale balcony slab

Since we tested only a portion of this slab identical to that in Phase I, this thesis used the service load as defined in Phase I of this work, which was 19 kN.

Appendix B – Thermal Test Results Second Steady State (SS2)

For the thermal experimental part of this research, three pairs of specimens, each pair with the same type of thermal break, were tested in a thermal chamber at Red River College in Winnipeg. The results from the first steady state can be found in chapter six. Thermal tests under a second steady state were also carried out for specimens with DOW and UHMW thermal breaks. Specimens with Armatherm^{TM} 500 were not tested under the second steady state, because thermistors had been taken off those specimens right after the first steady state tests. The following contains the results from the second steady state tests for DOW and UHMW specimens.

B.1 SS2 Temperatures for DOW Specimens

Table B1 shows the average temperatures recorded by each thermistor.

Table B 1 SS2 temperatures for DOW1 and DOW2

Thermistor Name	SS2 Temperatures for DOW1			SS2 Temperatures for DOW2		
	Section [A]	Section [B]	Section [C]	Section [A]	Section [B]	Section [C]
C35 – T	-17.19	-16.06	-14.55	-18.70	-19.02	-18.37
C130 – T	-20.34	-19.58	-18.66	-22.64	-21.93	-18.47
C0 – R	-7.95	-9.09	-9.53	-12.97	-	-13.04
C0 – M	-9.86	-9.35	-8.05	-13.34	-13.48	-13.21
C35 – M	-12.11	-11.68	-10.13	-16.98	-16.89	-15.39
C130 – M	-17.61	-16.70	-16.13	-20.09	-22.15	-22.77
C35 – B	-12.71	-11.06	-9.86	-14.59	-14.58	-13.93
C130 – B	-18.14	-15.97	-14.61	-21.54	-20.75	-20.60
H35 – T	+10.58	+10.81	+12.18	+8.02	+7.68	+7.32
H130 – T	+17.64	+18.38	+19.65	+16.18	+16.12	+16.57
H0 – R	+6.73	+7.32	+8.53	+4.51	+3.82	+4.41
H0 – M	+8.12	+9.09	+9.49	+5.34	+5.54	+5.70
H35 – M	+10.61	+11.15	+11.84	+6.42	+7.83	+7.56
H130 – M	+16.37	+16.38	+17.44	+9.70	+13.70	+14.15
H35 – B	+10.16	+13.15	+13.60	+417115	+7.60	
H130 – B	+18.82	+18.85	-	+16.43	-	+19.77

Thermistors were installed in sections A, B, and C on cold and hot sides of DOW1 and DOW2. The second steady state temperatures for DOW1 and DOW2 was -40 °C / +35 °C. Figure B1 includes drawings of the three sections of DOW1. The drawings show the location and recorded temperature of each thermistor for the second steady state.

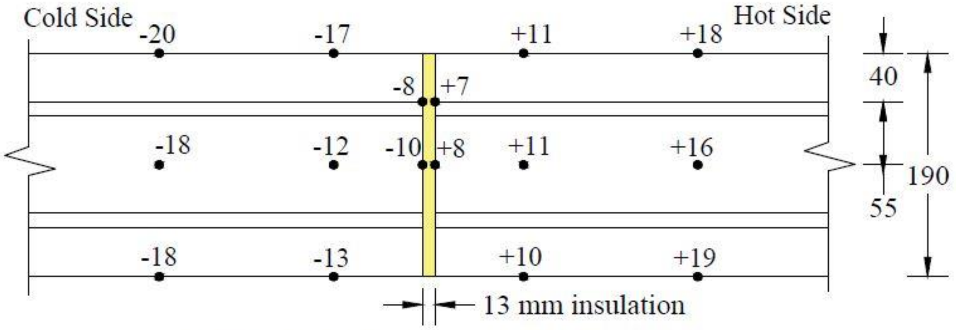

Section A-A [Thermistors] - DOW1 - SS2

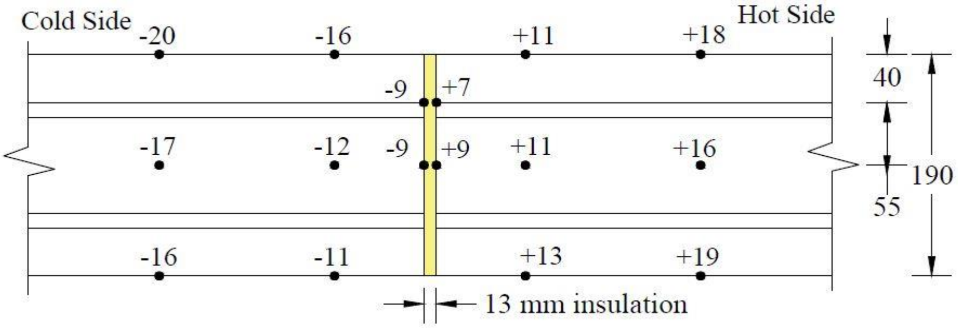

Section B-B [Thermistors] - DOW1 - SS2

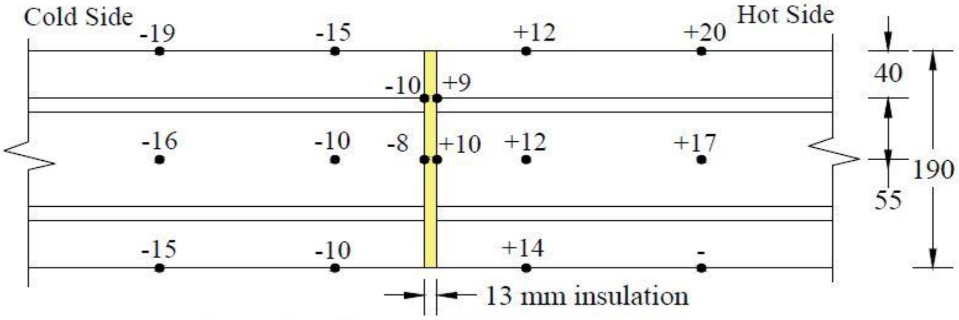

Section C-C [Thermistors] - DOW1 - SS2

Figure B 1 Sections AA/ BB/ CC for DOW1 – SS2

Figure B2 includes drawings of the three sections of DOW2. The drawings show the location and recorded temperature of each thermistor for the second steady state.

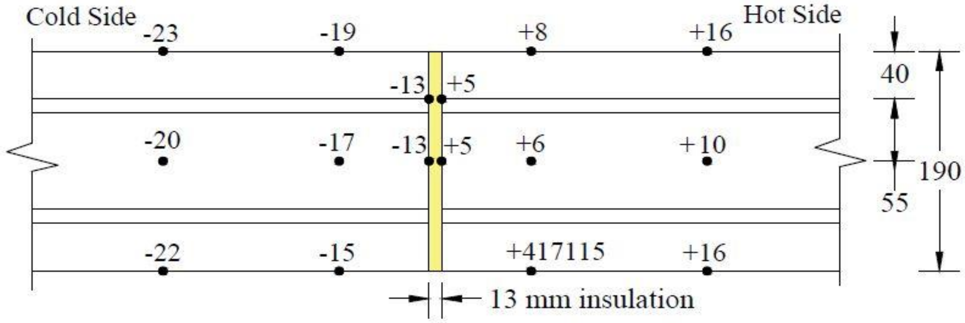

Section A-A [Thermistors] - DOW2 - SS2

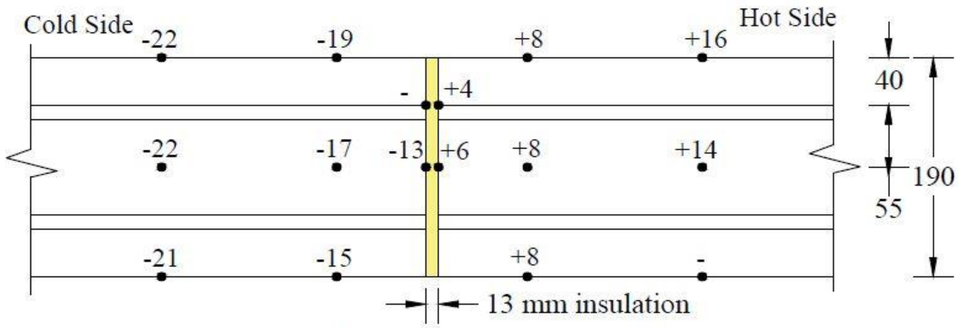

Section B-B [Thermistors] - DOW2 - SS2

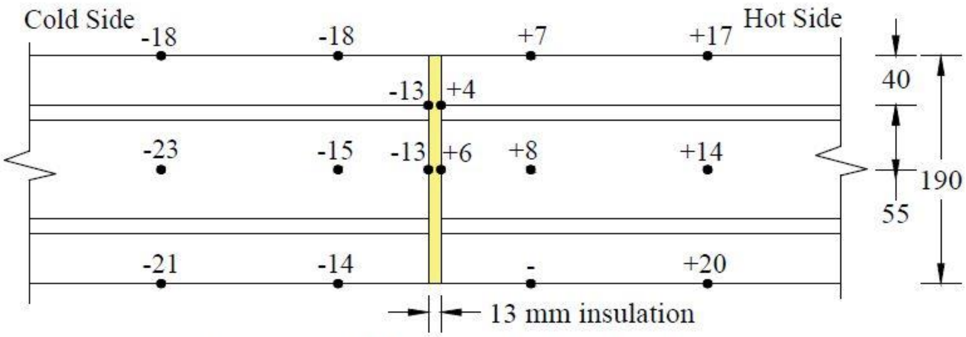

Section C-C [Thermistors] - DOW2 - SS2

Figure B 2 Sections AA/ BB/ CC for DOW2 – SS2

B.2 SS2 Temperatures for UHMW Specimens

For UHMW1 and UHMW2 the second steady state temperature was set at -40 °C / +28 °C. Table B2 shows the average temperatures recorded by each thermistor in sections A, B, and C on cold and hot sides of UHMW1 and UHMW2.

Table B 2 SS2 temperatures for UHMW1 and UHMW2

Thermistor Name	SS2 Temperatures for UHMW1			SS2 Temperatures for UHMW2		
	Section [A]	Section [B]	Section [C]	Section [A]	Section [B]	Section [C]
C35 – T	-13.72	-12.91	-13.70	-8.43	-8.72	-10.74
C130 – T	-19.03	-19.54	-19.40	-16.47	-17.45	-17.87
C0 – R	-5.66	-5.93	-6.19	-1.87	-2.15	-2.82
C0 – M	-4.48	-5.80	-4.87	-1.33	-1.63	-2.18
C35 – M	-8.13	-9.04	-8.67	-3.99	-5.77	-5.85
C130 – M	-15.50	-16.20	-15.98	-12.28	-13.82	-14.34
C35 – B	-10.17	-10.69	-12.75	-25.22	-9.31	-7.28
C130 – B	-18.15	-18.82	-18.83	-13.99	-16.04	-18.13
H35 – T	+4.76	+4.88	+5.27	+10.25	+9.52	+9.41
H130 – T	+17.55	+15.68	+21.49	+21.80	+21.29	+20.71
H0 – R	+1.18	+1.27	+1.47	+5.20	+5.23	+4.46
H0 – M	+15.22	+14.97	+15.31	+4.61	+5.49	+2.96
H35 – M	+5.31	+5.43	+5.55	+7.58	+9.00	-20.98
H130 – M	+2.28	+1.91	+2.78	+18.12	+17.64	+17.69
H35 – B	+6.60	+7.22	+7.26	+36.55	+10.70	+10.01
H130 – B	+18.81	+19.94	+19.60	+22.27	+21.17	+21.54

Figure B3 includes drawings of the three sections of UHMW1. The drawings show the location and recorded temperatures of each thermistor for the second steady state.

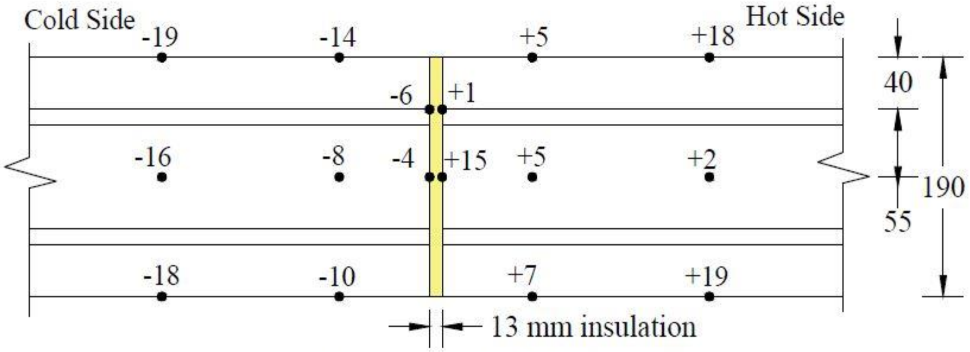

Section A-A [Thermistors] - UHMW1 - SS2

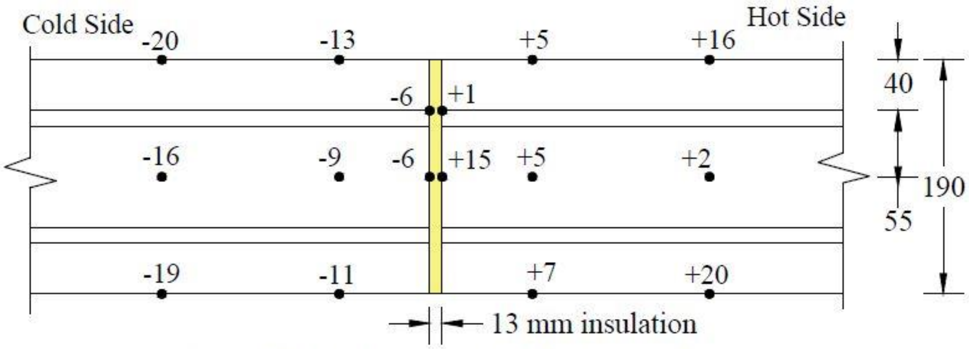

Section B-B [Thermistors] - UHMW1 - SS2

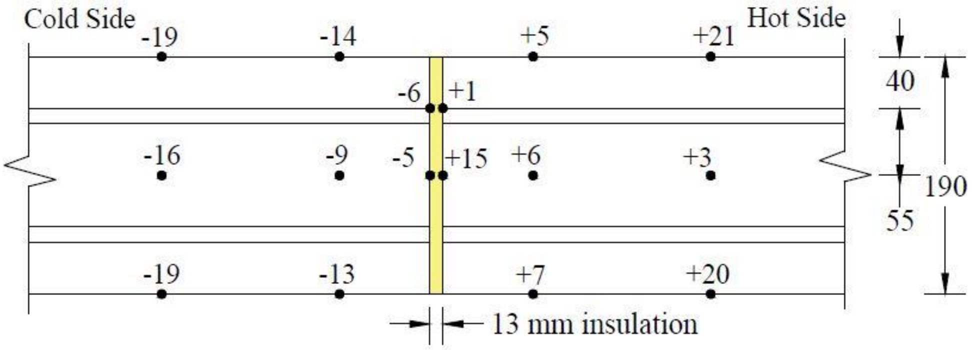

Section C-C [Thermistors] - UHMW1 - SS2

Figure B 3 Sections AA/ BB/ CC for UHMW1 – SS2

Figure B4 includes drawings of the three sections of UHMW2. The drawings show the location and recorded temperatures of each thermistor for the second steady state.

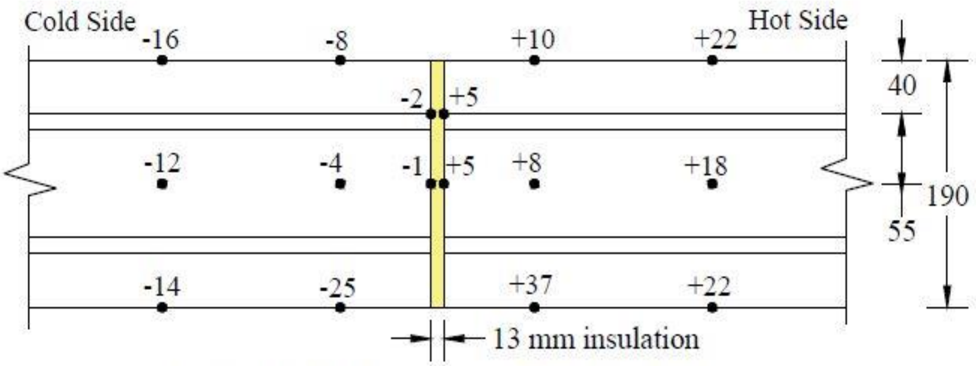

Section A-A [Thermistors] - UHMW2 - SS2

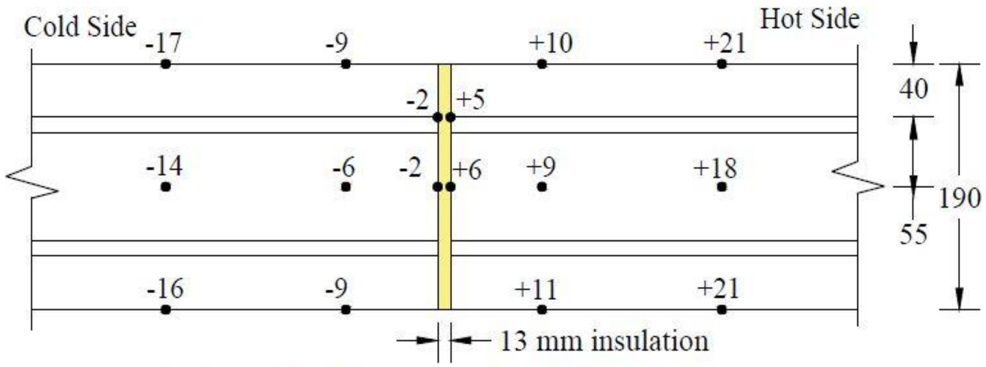

Section B-B [Thermistors] - UHMW2 - SS2

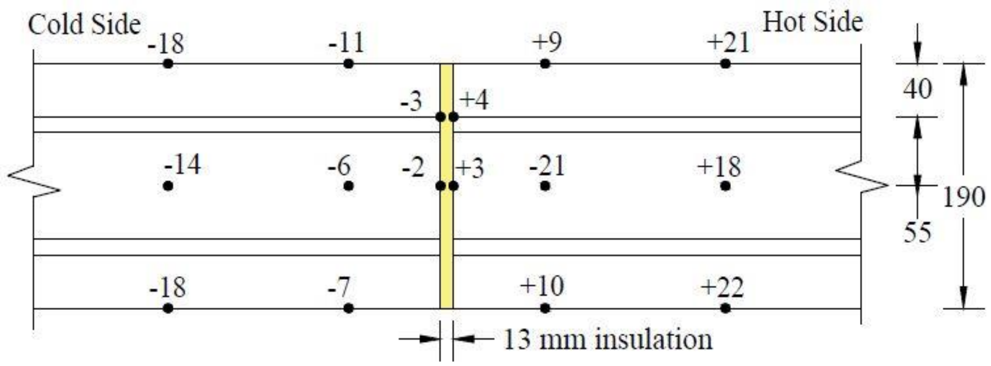

Section C-C [Thermistors] - UHMW2 - SS2

Figure B 4 Sections AA/ BB/ CC for UHMW2 – SS2